National Library
of Canada

Bibliothèque nationale
du Canada

Acquisitions and
Bibliographic Services Branch

Direction des acquisitions et
des services bibliographiques

395 Wellington Street
Ottawa, Ontario
K1A 0N4

395, rue Wellington
Ottawa (Ontario)
K1A 0N4

Your file Votre référence

Our file Notre référence

NOTICE

The quality of this microform is heavily dependent upon the quality of the original thesis submitted for microfilming. Every effort has been made to ensure the highest quality of reproduction possible.

If pages are missing, contact the university which granted the degree.

Some pages may have indistinct print especially if the original pages were typed with a poor typewriter ribbon or if the university sent us an inferior photocopy.

Reproduction in full or in part of this microform is governed by the Canadian Copyright Act, R.S.C. 1970, c. C-30, and subsequent amendments.

AVIS

La qualité de cette microforme dépend grandement de la qualité de la thèse soumise au microfilmage. Nous avons tout fait pour assurer une qualité supérieure de reproduction.

S'il manque des pages, veuillez communiquer avec l'université qui a conféré le grade.

La qualité d'impression de certaines pages peut laisser à désirer, surtout si les pages originales ont été dactylographiées à l'aide d'un ruban usé ou si l'université nous a fait parvenir une photocopie de qualité inférieure.

La reproduction, même partielle, de cette microforme est soumise à la Loi canadienne sur le droit d'auteur, SRC 1970, c. C-30, et ses amendements subséquents.

Canada

FRACTURE ANALYSIS OF CONCRETE DAMS BY BOUNDARY ELEMENT METHOD

Lingmin Feng

A Thesis
in
The Department
of
Civil Engineering

Presented in Partial Fulfillment of the Requirements
for the Degree of Doctor of Philosophy at
Concordia University
Montreal, Quebec, Canada

August, 1994

National Library
of Canada

Acquisitions and
Bibliographic Services Branch

395 Wellington Street
Ottawa, Ontario
K1A 0N4

Bibliothèque nationale
du Canada

Direction des acquisitions et
des services bibliographiques

395, rue Wellington
Ottawa (Ontario)
K1A 0N4

Your file Votre référence

Our file Notre référence

ISBN 0-315-97633-0

ABSTRACT

Fracture Analysis of Concrete Dams by Boundary Element Method

Lingmin Feng, Ph. D.
Concordia University, 1994

Static and dynamic cracking problems in concrete dams are studied by a new procedure employing linear elastic fracture mechanics theory, discrete crack modelling and the boundary element method (BEM).

This procedure is first implemented for static fracture analysis of gravity dams, followed by a detailed evaluation of the fracture process of concrete gravity dams during strong earthquakes. In the latter, the impact effect of crack closing is simulated by impulse and force rather than by change in stiffness, thus the mode superposition technique is still in effect within each stage of constant crack length. To verify the accuracy of the procedure, results are compared with rupture tests of a cantilever beam and a model of Koyna dam performed previously at Tsinghua University. The good correlation between the numerical predictions and test results indicates that the proposed procedure is relevant for evaluation of the seismic fracture process in concrete structures.

The above 2-D procedure is also applied in a case study of the Koyna prototype gravity dam under the 1967 earthquake. The results confirm the validity of the procedure for modelling crack propagation in concrete gravity dams during strong earthquakes.

This BE approach is then extended to analyze the 3-D cracking of arch dams using a simplified criterion for crack extension. The accuracy of the approach in computing 3-D stress intensity factors is verified by two examples. The first upstream cracking which occurred in the Kolnbrein arch dam is then studied in detail under various conditions concerning the foundation interface, location of initial cracking, water level and load combination. The good agreement between the numerical results and the reported field observations in terms of crack trajectory and crack trace on the upstream face demonstrates that the proposed approach can effectively be employed to predict the propagation of existing cracks in arch dams also.

ACKNOWLEDGMENTS

The author wishes to express his sincere thanks to his supervisor Dr. O. A. Pekau for the valuable guidance and thoroughness in this Thesis. The author would also like to express his sincere gratitude to his co-supervisor Professor Zhang Chuhan for his high standard of scholarship and engineering judgment in the progress of this research. Their constructive guidance, fruitful discussions and stimulating encouragement throughout the entire course of this study are greatly appreciated.

Acknowledgments are due to Concordia University for the supply of excellent computer facilities and financial support in terms of Concordia graduate fellowship and part time teaching assistantship. The financial support provided by the National Sciences and Engineering Research Council of Canada under Grant No. A8258, under which the analytical work reported in this Thesis was performed at Concordia University, is gratefully acknowledged. The author also gratefully acknowledges Tsinghua University of China for the facilities used by the author to conduct the dynamic rupture tests and to begin the 2-D crack modelling before joining Concordia. The valuable information on the Kolnbrein arch dam supplied by Tauernplan Consulting GMBH of Austria is also gratefully appreciated.

The author also wishes to express his heartful thanks to his whole family for their moral support and encouragement. Finally, the author extends his special thanks to his wife, Na Lin, for her support, encouragement and understanding.

Life Is Like A Mirror
If You Smile At It
It Will Smile At You

生活象一面镜子
你对他笑
他也对你笑

TABLE OF CONTENTS

LIST OF FIGURES

LIST OF TABLES

LIST OF SYMBOLS

a	length or radius of crack; major semi-axis of ellipse; coefficient
b	minor semi-axis of ellipse; gravitational force
c, C	coefficient
E	elastic modulus; kinetic energy
f	frequency; function describing acceleration field
F	nodal force
$J(\xi)$	Jacobian of transformation ξ to x
k	stiffness
K	combined stress intensity factor
K_I, K_{II}, K_{III}	mode I, II, III stress intensity factors
K_C, K_{IC}	fracture toughness of mode I
K_{IIC}	fracture toughness of mode II
K_d, K_{Id}	dynamic fracture toughness of mode I
L, L_c	length of crack tip element
m	mass
n	unit outward normal; number of nodes
$N_i(\xi)$	interpolation function
p	traction
p^*_{ij}	2-D traction Kelvin fundamental solution
P	source point
P_n	n^{th} load pulse
Q	integration point; nodal force
Q_s	nodal force caused by static loads
r	polar coordinate; direction normal to crack surface
R	distance from P to Q

S	strain energy density factor
S_{min}	minimum value of strain energy density factor
S_n	impulse
t	time; traction
T	change in temperature
T_{ij}	3-D traction Kelvin fundamental solution
u, U	displacement
$\dot{u}$	velocity
$\ddot{u}$	acceleration
$\ddot{u}^o$	base acceleration
u^*_{ij}	2-D displacement Kelvin fundamental solution
U_{ij}	3-D displacement Kelvin fundamental solution
V	displacement
W_i	integration term corresponds to self-weight
x	Cartesian coordinate
Y	generalized coordinate
$\dot{Y}$	generalized velocity
$\ddot{Y}$	generalized acceleration
β	parametric angle
δ	Dirac delta function
δ_{ij}	Kronecker delta
$\tilde{\varepsilon}_\theta$	circumferential strain factor
ϕ	spherical angle; mode shape
$\phi_d(\xi)$	interpolation function for displacement
$\phi_t(\xi)$	interpolation function for traction
γ	specific weight
Γ	boundary

Γ_ε	circular arc with radius ε
η	modal participation factor
λ	coefficient
μ	shear modulus
ν	Poisson's ratio
θ	polar coordinate; spherical angle
θ_0	crack propagation angle
ρ	mass density
σ	stress
ω	circular frequency
Ω	domain
ξ	local coordinate; damping ratio

CHAPTER 1

INTRODUCTION

1.1 LITERATURE REVIEW OF PAST CRACKING PROBLEMS IN CONCRETE DAMS

Most concrete dams including gravity, buttress and arch types experience varying degrees of cracking during the construction stage. Usually, this cracking is attributed to internal and external temperature variations, shrinkage of the concrete and, in some cases, differential foundation settlement. For example, the Revelstoke gravity dam in Canada[1], the Dragon arch dam in Romania[2], the Buffalo Bill arch dam in U.S.A.[3], the Salas buttress dam in Spain[4], the Zhaxi buttress dam[5], the Dong Jiang[6] and the Jinshui Tan[7] arch dams in China have reportedly experienced cracking during the construction stage due primarily to differential temperature and concrete shrinkage. On the other hand, the cracking discovered in the Daniel Johnson multiple arch dam in Canada[8], the Zervreila[9] and the Zeuzier[10] arch dams in Switzerland and, the Glen Canyon and the Hoover arch dams[3] in U.S.A. was reportedly due to nonlinear, permanent deformation of the foundation. Although the scales and depths of these cracks are relatively small and shallow, whether the cracks remain stable or not under varying loading conditions during the operation phase becomes a source of concern for the safety of these structures. Furthermore, if the cracks are unstable, what kinds of trajectories will they develop? These problems are crucial for the normal operation of such structures.

For example, under hydrostatic pressure and temperature variation, one of the small vertical surface cracks on the upstream face of the 104 m high Zhaxi diamond-head buttress dam propagated 43 m into the dam in 1969 after eight years of normal operation, and in 1977 another vertical crack experienced similar extension with 16 m depth into the dam[5].

Detailed studies by 2-D and 3-D finite element models and photoelastic experiment were performed to determine the causes of the crack propagations, and various measures including anchoring the cracked buttress by prestressed cables, sealing the cracks with epoxy mortar, drilling holes to release high uplift pressure in the crack and placing concrete plugs to support the buttress were taken to strengthen the dam.

Cracking damage as, in the above Zhaxi dam, severely hampers normal operation and may also endanger the safety of the dam; thus it is imperative to study the stability and extension of existing cracks in concrete dams to improve the method for designing new dams and identifying remedial measures to reinforce existing dams.

The behaviour of concrete dams exposed to strong earthquake has also been studied for decades. Since the Hsinfengkiang buttress dam in China[11] and the Koyna gravity dam in India[12] experienced very similar severe cracking damage during strong earthquakes in 1962 and 1967, considerable attention has focused on evaluating the safety of existing dams and predicting the dynamic performance of newly designed concrete dams subjected to strong earthquakes. Finite element analysis related to dynamic behaviour of the Koyna and Hsinfengkiang dams has demonstrated that very large tensile stresses occurred on the downstream face of the upper part of the dams, at the point of slope change consistent with the general location of observed cracking. From a number of publications related to numerical and experimental studies of the aforementioned dams, it is recognized that strong amplification of the motion in the upper part of the dam and an intensive stress concentration at the point of slope change were largely responsible for initiating the cracking damage.

A number of 2-D linear analyses have been made to determine the dynamic response of Koyna dam when subjected to the recorded accelerations, while others attempted to include the nonlinear features of cracking. A seismic study[13] by the finite element method considered cracking with stress release once the tensile stress reached a critical value which included a factor to account for strain rate effects. Ayari and Saouma[14] used fracture mechanics and a contact/impact model for crack closure within a finite element formulation to analyze the seismic performance of the Koyna dam. Recently, Bhattacharjee and Leger[15] performed the cracking analysis of Koyna dam by a non-linear smeared fracture energy conservation model using finite element method. All these studies revealed that formation of cracks on both faces was to be expected during the 1967 earthquake.

Another study[16] of the Koyna dam has attempted to model the formation and propagation of cracks based on the maximum tensile strength criterion and a discrete crack approach. The cracks were simulated by separation of originally adjacent finite elements; however, the cracking pattern obtained was totally different depending on the mesh refinement.

Experiments have also been conducted to study the dynamic response and cracking pattern. In an investigation of damage causes and strengthening measures for the Hsinfengkiang dam in 1964, a 4.5 m high model was built near the dam site and explosives were used to generate ground motions as the input. In these tests the acceleration amplification ratio reached 6.5 at the crest of the model and finally caused cracking rupture at a location very similar to that observed in the prototype[17].

A similar experiment for Koyna dam was conducted at the University of California at Berkeley[18]. A 1:150 scale model was constructed of a plaster material containing lead powder. During the test run at 1.21 g of the shaking table a crack was initiated on the downstream face at the point of slope change, which then propagated through the dam to the upstream face. Even though the excitation applied to the model was not actual Koyna ground motion and improper gravity scaling for rupture similarity was employed, the results still gave valuable insight into the cracking pattern and location under the test conditions.

A recent study of concrete gravity dam under dynamic load by shaking table tests was carried out by Donlon and Hall[19]. A series of tests on three small-scale models of the Pine Flat dam monolith under simulation of earthquake shaking were conducted to examine the characteristics of crack formation and the overall stability after the crack penetrated the dam. It was found that the neck region of a gravity dam is most vulnerable to cracking and no failures occurred in the three models due to the favorable orientations of the developed crack profiles for resisting sliding failure.

As indicated in Reference [20], for a sharp slope change at the dam face a point of singularity occurs and the maximum tensile stress becomes infinite if the linear elastic idealization for concrete is maintained. Thus, the crack formation and propagation process should be analyzed by fracture mechanics theory in which stress intensity factors need to be evaluated.

Due to the complexity of evaluating crack propagation in concrete gravity dams under strong earthquakes, sophisticated mathematical models for dealing with the cracking process of concrete structures are needed and model tests for either verification of the mathematical models or simulation of the prototype performance remain imperative.

In comparison to the 2-D case of gravity dams, the 3-D cracking problem in arch dams is even more complicated. Since an arch dam is a highly indeterminate 3-D structure, the distribution of stresses under sustained loadings is sensitive to the shape of the canyon as well as to the dam itself, and also to nonuniform deformation of the foundation. Thus, small initial cracks caused by excessive thermal strains or foundation settlement may become severe following filling of the reservoir, as was the case for the Kolnbrein arch dam in Austria[21].

At present, the traditional trial load method for cracking analysis of arch dams uses the maximum tensile stress[3], i.e. if at any point the computed tension exceeds the tensile strength, cracking will occur and develop to the point of zero stress. The resulting changes in stiffness of the dam accompanying crack propagation must be recomputed until convergence is achieved. Evidently, this criterion has the drawback of not considering the stress singularity at the crack tip. When the finite element method is employed for taking the effect of this stress concentration into account with the tensile strength still in use, the propagation of the crack will depend on the mesh size of the elements near the crack tip, and objective results cannot be obtained unless the energy criterion of fracture mechanics is incorporated.

Because of the analytical challenge posed by the complexity of the 3-D crack propagation problem related to arch dams, few publications have appeared to-date in the literature. To the author's knowledge, Linsbauer and Ingraffea et al.[22], [23] were the first to apply LEFM in the cracking analysis of arch dams, employing a 2-D finite element model of the Kolnbrein arch dam. Although the results identified several possible explanations for the cracking of this dam, it is obvious that their 2-D simulation of a doubly curvated arch dam cannot consider the redistribution of the external loads between arch and cantilever actions of the dam during the crack propagation process.

More recently, Martha et al.[24] developed a new system for interactive analysis of crack initiation and propagation in arch dams by 3-D modelling. An example arch dam was employed to demonstrate the capability of the system to simulate 3-D crack extension. It was assumed that each point along the crack propagates within a plane perpendicular to the crack front and in the direction of the local maximum circumferential tensile stress. Additionally, the length of the crack extension was assumed proportional to the value of K_I^2 at the point. However, no data were reported to verify the validity of these assumptions for crack propagation in arch dams.

1.2 OUTLINE OF PRESENT STUDY

For crack analysis of structures, both linear elastic fracture mechanics (LEFM) and nonlinear fracture mechanics (NLFM) may be considered. The latter includes the fictitious crack model presented by Hillerborg[25] and the blunt crack band model by Bazant[26], both taking the effects of strain softening into account by different assumptions. Since the characteristic dimension of a dam is much greater than the micro-cracking or process zone, and considering that mass concrete is basically a brittle material with no significant softening characteristics, LEFM is deemed applicable to the analysis of cracking in concrete dams.

There are two approaches of modelling cracks in numerical analysis of concrete structures[27]: (i) the discrete crack model in which a crack is modelled by an inter-element discontinuity between adjacent elements; and (ii) the smeared crack model in which the crack is distributed over entire elements. The smeared crack approach can easily include the non-linear effects associated with cracking, the closing and reopening of the cracks by internal material behaviour of the elements under consideration. However, this model only considers the overall effect of cracking – the exact location of an individual crack is not determined, and the procedure is sensitive to mesh size and alignment unless the energy criterion of fracture mechanics is employed. For structures with normal amounts of reinforcing steel and reasonable level of stress, the smeared crack approach is well suited to model the behaviour during and after cracking, as the reinforcement tends to give the structure a smeared crack pattern, i.e. with many small cracks distributed in a banded region. However, for unreinforced concrete structures such as concrete dams, the cracking will lead to a release of tensile stresses in the zone of the crack resulting in single, discrete crack pattern. Therefore, for unreinforced structures, the discrete crack approach represents suitable method of modelling cracking. Furthermore, this model can easily apply uplift pressure on the crack surfaces which has significant effect on the stability of the crack in concrete dams. Thus, the discrete crack approach is a physically more realistic model for concrete dams.

As noted before, the finite element method (FEM) has been employed extensively in previous analyses on fracture of concrete dams because it can easily include the nonlinear behaviour of concrete cracking. Due to its apparent versatility, the FEM can deal with such problems as nonlinear or anisotropic material behaviours and irregular body forces. Recent examples of such applications are the analysis of the progressive cracking in gravity dams due to the combined effects of water intrusion and concrete expansion by Cervera et al.[28] and the poroplastic analysis of concrete dam cracking including the pore pressure effect inside the dam body[29]. However, the boundary element method (BEM)[30] has increasingly gained popularity among numerical methods recently as an alternative technique to treat cracking problems in concrete. In this application, it has the following advantages over the FEM: (i) reducing the dimension of the problem by one; (ii) much less data preparation and easier remeshing of the crack tip discretization; and (iii) valuable representation for stress concentration resulting in better accuracy for computation of stress intensity factors (SIFs). Due to these inherent benefits, the BEM is particularly suitable for solving crack problems using discrete crack model.

Based on the above considerations, the boundary element method, linear elastic fracture mechanics theory and discrete crack model are employed herein to study the cracking problems in concrete dams.

In Chapter 2, in order to obtain the appropriate length for the crack tip elements when using the BEM to calculate the stress intensity factors, a rectangular plate having an edge crack was analyzed with different L_c/a (where L_c is the length of the crack tip element and "a" is the crack length) in a parametric study. It is found that highest accuracy is achieved when L_c is about 10% of the crack length. To compare the efficiency and accuracy between BEM and FEM, the stress intensity factors for the same plate were computed by both methods. It is revealed that BEM has the benefits of less data preparation and CPU time but better accuracy than FEM. Employing the maximum tensile strain criterion of crack extension, the stability and propagation process of cracks near the heel of a gravity dam under static loadings of hydrostatic pressure and self-weight of the dam is examined as an application example. For this example, it is concluded that the horizontal cracks near the heel of the dam will develop rapidly downwards to the interface between the dam and the foundation. The distribution pattern of uplift pressure on the crack surfaces has a significant effect on the stability of the cracks and the effective drainage system near the heel of the dam plays an important role in resisting crack extension.

Chapter 3 presents the extension of the preceding 2-D static formulation to the cracking process of concrete gravity dams during strong earthquakes[31] and the corresponding specialized software FAPGD (Fracture Analysis Program for Gravity Dams) is developed. In this procedure the boundary element technique, dynamic modal analysis and linear elastic fracture mechanics theory are combined. Two alternative methods, namely the impulse and the force methods, are presented to simulate the behaviour of crack closing during earthquake response. The force method is developed to prevent the hypothetical overlap phenomenon which is originally assumed in the modelling of crack closure by the impulse method. During the nonlinear process of crack extension, the computation is divided into discrete stages having different natural frequencies and mode shapes. However, it remains linear within each stage of constant crack length provided that the dynamic stress intensity factor is lower than the fracture toughness of the concrete. Since the impact effect of crack closing is simulated by impulse and force rather than by change in stiffness, the mode superposition technique, which is efficient for linear seismic analysis, is still in effect within each stage. The maximum strain criterion is employed for predicting the orientation of crack extension, whereas the propagation process itself is simulated in a stage by stage procedure. Generally, the proposed method is efficient for the analysis of seismic crack propagation under earthquake loadings, due primarily to simplification of the nonlinear dynamic problem resulting from the linearized nature of the present formulation combined with the computational advantages of BE modal analysis.

The accuracy of the above 2-D formulation for seismic fracture is confirmed by comparing with previously obtained results for tests of a cantilever beam and a model of Koyna dam both made of gypsum under excitation of a shaking table. The very good agreement obtained between the numerical predictions and the experimental data in aspects of natural frequencies, time histories of stress intensity factors and final crack profiles indicates that the proposed procedure is relevant for evaluation of the 2-D seismic fracture process in concrete gravity dams.

Chapter 4 applies the above 2-D procedure to the case study of Koyna prototype dam in India under the 1967 earthquake[32]. Crack propagation analyses of the dam are first performed under only seismic loading in a parametric study to obtain the magnitude of time step and the number of modes required for the convergence of the computation of crack propagation. The extension process of the crack is then, analyzed, by both impulse and force methods for simulation of crack closure under the actual load conditions including the hydrostatic pressure, the self-weight of the dam, the 1967 Koyna earthquake comprising both the stream and vertical components, and the hydrodynamic pressure of the reservoir. The results show that the final rupture profiles obtained from the two methods are in excellent agreement for both the prototype and a model of the Koyna dam, thus indicating that the crack closure mechanism has no significant effect on the crack propagation trajectories. Since the numerical results and the model test for the Koyna dam show very similar patterns of rupture, also consistent with the prototype measurements after the 1967 earthquake, it is concluded that the present boundary element procedure based on LEFM is suitable for modelling crack propagation in concrete gravity dams during strong earthquakes.

The foregoing 2-D BE and fracture mechanics based formulation is extended in Chapter 5 to the analysis of the stability and propagation of 3-D static cracking for the much more complex case of arch dams and the associated software FAPAD (Fracture Analysis Program for Arch Dams) is developed. In order to improve the accuracy in computing 3-D stress intensity factors by BEM, special crack front elements are employed and the appropriate coordinate transformation technique is performed to evaluate accurately the singular integral associated with the special crack front element by standard Gaussian quadrature formulae. The accuracy of the procedure to compute 3-D stress intensity factors is verified for a horizontal and an inclined circular crack within a cylinder. Because of the great difficulties in dealing with 3-D crack propagation in arch dams using LEFM, certain simplifying assumptions are introduced in the computational modelling of the crack propagation process.

Finally, in Chapter 6 the preceding 3-D procedure is applied to the case study of the Kolnbrein arch dam in Austria[33]. The first upstream crack which occurred in this dam is studied in detail under various conditions concerning the foundation interface, location of crack initiation, reservoir water level and load combination. Crack trajectories close to the observed one are obtained with water level at 1850-1860 m, which agrees with the prototype experience. It is found that the hydrostatic load and associated uplift pressure on the crack surfaces are the key factors for causing an initial crack at the dam base to propagate to the upstream face. It is also noted that the bonded condition at the interface between the dam and the upstream elevated foundation is responsible for producing the distinctive profile of the observed crack which daylights on the upstream face at an acute angle. The good agreement between the numerical results and the observations in respect to crack trajectory and crack trace on upstream face confirms that the current fracture mechanics based boundary element procedure can also be employed to predict crack extension in arch dams wherein using a simplified model for 3-D crack propagation.

CHAPTER 2

FORMULATION OF 2-D STATIC CRACK PROBLEMS

Before undertaking detailed studies of static and dynamic fracture of dams, the boundary element (BE) formulation for two-dimensional elastostatic crack problems is presented and the accuracy of the procedure in computing stress intensity factors is examined. Also presented is an example application consisting of the crack propagation analysis of a gravity dam under static loading.

2.1 BOUNDARY ELEMENT FORMULATION OF 2-D ELASTOSTATICS

By making use of the residual approximation and utilizing the 2-D Kelvin fundamental solution as the weighting function, the governing static equilibrium equation for a homogeneous isotropic elastic domain Ω can be transformed to the following boundary integral equation[30]

$$c_{ij}(P)u_j(P)+\int_\Gamma p^*_{ij}(P,Q)u_j(Q)d\Gamma=\int_\Gamma u^*_{ij}(P,Q)t_j(Q)d\Gamma$$

$$+\int_\Gamma W_i(P,Q)d\Gamma \qquad (2.1)$$

where u_j ($j=1, 2$) are the displacements, t_j the tractions at the boundary Γ of the domain Ω; P is the source point, Q the integration point, both on the boundary;

$$c_{ij}=\lim_{\varepsilon\to 0}\int_{\Gamma_\varepsilon} p^*_{ij}d\Gamma_\varepsilon$$

in which Γ_ε is the circular arc within the domain with radius ε and centre P.

$u^*_{ij}(P,Q)$ and $p^*_{ij}(P,Q)$ are the 2-D Kelvin fundamental solution given by[30]

$$u^*_{ij}(P,Q)=\frac{(1+\nu)}{4\pi E(1-\nu)}[(3-4\nu)\ln(\frac{1}{R})\delta_{ij}+\frac{\partial R}{\partial x_i}\frac{\partial R}{\partial x_j}]$$

$$p^*_{ij}(P,Q)=-\frac{1}{4\pi(1-\nu)R}\{\frac{\partial R}{\partial n}[(1-2\nu)\delta_{ij}+2\frac{\partial R}{\partial x_i}\frac{\partial R}{\partial x_j}]+(1-2\nu)(\frac{\partial R}{\partial x_j}n_i-\frac{\partial R}{\partial x_i}n_j)\} \tag{2.2}$$

where R is the distance from P to Q, δ_{ij} the Kronecker delta, n_i the unit outward normal at Q, E the elastic modulus, ν the Poisson's ratio, and x_i is the Cartesian coordinate; $W_i(P,Q)$ in equation (2.1) corresponds to the body force of self-weight and is given by

$$W_i(P,Q)=\frac{(1+\nu)R}{4\pi E}[2\ln(\frac{1}{R})-1][b_i n_j\frac{\partial R}{\partial x_j}-\frac{1}{2(1-\nu)}b_j\frac{\partial R}{\partial x_j}n_i] \tag{2.3}$$

in which b_i is the constant gravitational force.

It should be noted that equations (2.2) and (2.3) are only valid for plane strain problems. They are valid for plane stress if E and ν are replaced by $E' = (1+2\nu)E/(1+\nu)^2$ and $\nu' = \nu/(1+\nu)$, respectively.

Discretizing the boundary Γ into m elements and on each r-node element, the displacements and tractions are expressed in terms of nodal values through the r interpolation functions $\phi_{dr}(\xi)$ and $\phi_{tr}(\xi)$, respectively, leading equation (2.1) to become

$$c_{ij}(p)u_j(p)+\sum_{l=1}^{m}\sum_{s=1}^{r}H_{ij}^{pls}u_j^{ls}=\sum_{l=1}^{m}\sum_{s=1}^{r}G_{ij}^{pls}t_j^{ls}+\sum_{l=1}^{m}\sum_{s=1}^{r}B_i^{pls} \tag{2.4}$$

where the source point P has been taken to coincide with the discretization node p. The coefficients H_{ij}^{pls}, G_{ij}^{pls} and B_i^{pls} are given by

$$H_{ij}^{pls}=\int_{\Gamma_l}p^*_{ij}(P,Q^l(\xi))\phi_{ds}(\xi)J^l(\xi)d\xi \tag{2.5}$$

$$G_{ij}^{pls} = \int_{\Gamma_{\ell}} u*_{ij}(P, Q^{l}(\xi))\phi_{ls}(\xi)J^{l}(\xi)d\xi \tag{2.6}$$

$$B_{i}^{pls} = \int_{\Gamma_{\ell}} W_{i}(P, Q^{l}(\xi))J^{l}(\xi)d\xi \tag{2.7}$$

where $J(\xi) = d\Gamma/d\xi$ is the Jacobian of transformation ξ to x.

Applying equation (2.4) to nodal point p and adding the terms relating to the same node q, we obtain

$$\sum_{q=1}^{n} H*_{ij}^{pq}u_{j}^{q} = \sum_{q=1}^{n} G_{ij}^{pq}t_{j}^{q} + \sum_{q=1}^{n} B_{i}^{pq} \tag{2.8}$$

in which n is the total number of nodes in the mesh.

When all the n nodes are considered, with the proper boundary conditions applied and the terms reordered, equation (2.8) leads to a non-symmetric fully-populated system of 2n equations with 2n unknowns which can be solved by Gauss elimination scheme. When the domain is divided into subdomains, from the conditions of compatibility and equilibrium on the interface between the subdomains α and β, we have

$$u_{i}^{(\alpha)} = u_{i}^{(\beta)} \quad , \quad t_{i}^{(\alpha)} = -t_{i}^{(\beta)}$$

To avoid directly evaluating c_{ij} and the strongly singular integral in equation (2.5) when the node s of the element l coincides with point p, the coefficients $H*_{ij}{}^{pp}$ can be obtained by applying the rigid body motion condition to equation (2.8):

$$H*_{ij}^{pp} = -\sum_{q=1}^{n} H*_{ij}^{pq} \quad (q \neq p)$$

All the other integrals in equations (2.5) - (2.7) are numerically computed by Gaussian quadrature formula. In order to obtain a roughly uniform precision of integration, the order of the Gaussian formula is determined according to the rapidity of variation of the integrand within the element.

2.2 COMPUTATION OF STRESS INTENSITY FACTORS

It is recognized that the BEM has the advantages of better accuracy in solving stress concentration problems and greater efficiency in remeshing an extended crack surface in comparison with the FEM. If BEM is applied directly to cracking problems, the coefficient matrix of the equation becomes singular[34] because it cannot distinguish between the two coincident surfaces of a crack within one domain. Cruise modelled the crack with a small width between the two surfaces[35] which requires very fine discretization on the crack surfaces and yields poor accuracy. The so-called "Multi-domain Method"[36] has been shown to be effective for cracked structures and is therefore adopted in the present study. It treats the cracked structure as two separate subregions artificially divided by the crack surface and its prolonged line, but requires that continuity and equilibrium conditions be satisfied along the latter.

For the coordinate system at the crack tip shown in Figure 2.1(b), the displacement and stress fields near the tip for a combined opening (type I) and sliding (type II) crack mechanism (with r << a, where 'a' represents the length of the crack) are given by[37]

$$
\begin{aligned}
u_r &= \frac{1}{8\mu}\sqrt{\frac{2r}{\pi}}\left\{K_I\left[(2k-1)\cos\frac{\theta}{2}-\cos\frac{3\theta}{2}\right]+K_{II}\left[(2k-1)\sin\frac{\theta}{2}-3\sin\frac{3\theta}{2}\right]\right\} \\
u_\theta &= \frac{1}{8\mu}\sqrt{\frac{2r}{\pi}}\left\{K_I\left[-(2k+1)\sin\frac{\theta}{2}+\sin\frac{3\theta}{2}\right]+K_{II}\left[(2k+1)\cos\frac{\theta}{2}-3\cos\frac{3\theta}{2}\right]\right\}
\end{aligned}
\qquad (2.9)
$$

and

$$\sigma_r = \frac{1}{2\sqrt{2\pi r}}\left[K_I(3-\cos\theta)\cos\frac{\theta}{2} + K_{II}(3\cos\theta-1)\sin\frac{\theta}{2}\right]$$

$$\sigma_\theta = \frac{1}{2\sqrt{2\pi r}}\left[K_I(1+\cos\theta)\cos\frac{\theta}{2} - K_{II}(3\sin\theta)\cos\frac{\theta}{2}\right] \qquad (2.10)$$

$$\tau_{r\theta} = \frac{1}{2\sqrt{2\pi r}}\left[K_I\sin\theta\cos\frac{\theta}{2} + K_{II}(3\cos\theta-1)\cos\frac{\theta}{2}\right]$$

in which

$$\mu = \frac{E}{2(1+\nu)} \quad ; \qquad k = \begin{cases} (3-4\nu) \quad , & \text{plane strain} \\ (3-\nu)/(1+\nu), & \text{plane stress} \end{cases}$$

where E is the modulus of elasticity; ν is Poisson's ratio; K_I and K_{II} are the stress intensity factors for types I and II crack mechanisms, respectively.

Crack tip element

Based on the $r^{1/2}$ displacement variation and $r^{-1/2}$ stress variation near the crack tip as shown in equations (2.9) and (2.10), one can define the displacement and boundary traction of the crack tip element as follows:

$$u = a_0 + a_1\sqrt{\xi} + a_2\xi = \sum_{i=1}^{3} N_i(\xi)\,u_i$$

$$t = (a_0 + a_1\sqrt{\xi} + a_2\xi)/\sqrt{\xi} = \sum_{i=1}^{3} \frac{1}{\sqrt{\xi}} N_i(\xi)\,t_i \qquad (2.11)$$

in which u_i, t_i are the nodal displacement and traction at point i, respectively; a_0, a_1, a_2 are coefficients; and $N_i(\xi)$ are interpolation functions taken as

$$N_1(\xi) = 1 - 3\sqrt{\xi} + 2\xi$$

$$N_2(\xi)=4(\sqrt{\xi}-\xi) \tag{2.12}$$

$$N_3(\xi)=-\sqrt{\xi}+2\xi$$

where ξ is the local coordinate of the quarter point crack tip element shown in Figure 2.1(a).

Stress intensity factors(SIFs)

(i) Crack in one material

According to Reference [38], better accuracy can be achieved by employing the 'one-point' rather than the 'two-point' formula to compute the stress intensity factors. Thus, for the combined opening and sliding cracking mechanism (i.e. types I and II, respectively), the stress intensity factors are determined from the relative displacements at element quarter points B and D [shown in Figure 2.1(b)] by substituting $\theta=\pi$ and $-\pi$ into equation (2.9), resulting in the following 'one-point' expressions:

$$\begin{aligned} K_I &= \frac{2\mu}{(k+1)}\sqrt{\frac{\pi}{2r}}\,(V_D - V_B) \\ K_{II} &= \frac{2\mu}{(k+1)}\sqrt{\frac{\pi}{2r}}\,(U_D - U_B) \end{aligned} \tag{2.13}$$

where U_B, U_D, V_B, V_D represent nodal displacements in the U and V directions; r corresponds to the radial coordinate of nodal points D and B.

(ii) Crack on the interface of two different materials

When the crack is located on the interface of two different materials, the stress intensity factors can be computed using the displacements of the crack surfaces near the crack tip as proposed by Smelser[39].

Employing the coordinate system shown in Figure 2.2, the complex relative displacement of the crack surfaces is defined as:

$$\Delta U = U_2 \big|_{\theta=\pi} - U_1 \big|_{\theta=-\pi}$$

the norm of ΔU can be expressed as

$$|\Delta U| = \frac{1}{4\sqrt{2\pi}}(\Lambda_1+\Lambda_2)\frac{K_0}{\lambda_0}\sqrt{r} \tag{2.14}$$

where

$$\Lambda_\alpha = \begin{cases} 4(1-\nu_\alpha)/\mu_\alpha \quad , \text{ plane strain} \\ 4/[\mu_\alpha(1+\nu_\alpha)] \; , \text{ plane stress} \end{cases} \qquad \alpha = 1\,,2$$

in which μ_α, ν_α are the shear modulus and Poisson's ratio of material α, respectively; K_0 is the norm of the complex stress intensity factor **K** which is defined by

$$K = K_0 e^{i\beta} = K_I + i\, K_{II}$$

$$\lambda_0 = \sqrt{\frac{1}{4} + \varepsilon^2} \quad , \quad \varepsilon = \frac{1}{2\pi}\ln\left(\frac{\mu_1+\mu_2\kappa_1}{\mu_2+\mu_1\kappa_2}\right)$$

in which

$$\kappa_\alpha = \begin{cases} (3-4\nu_\alpha) \quad , \qquad \text{plane strain} \\ (3-\nu_\alpha)/(1+\nu_\alpha)\; , \text{ plane stress} \end{cases} \qquad \alpha = 1\,,2$$

The argument of ΔU can be expressed as

$$\phi = \varepsilon \ln r - \beta - \delta + \pi/2 \tag{2.15}$$

in which

$$\delta = \tan^{-1}(2\varepsilon)$$

From equations (2.14) and (2.15) we have:

$$K_0 = \frac{4\sqrt{2\pi}\,\lambda_0 |\Delta U|}{(\Lambda_1 + \Lambda_2)\sqrt{r}} \tag{2.16}$$

$$\beta = \varepsilon \ln r - \delta - \phi + \pi/2 \tag{2.17}$$

Thus, the stress intensity factors are obtained by

$$\begin{aligned} K_I &= K_0 \cos\beta \\ K_{II} &= K_0 \sin\beta \end{aligned} \tag{2.18}$$

in which K_0 and β are determined by equations (2.16) and (2.17), respectively.

2.3 CRITERION FOR CRACK PROPAGATION

To predict the orientation of the crack development, there are alternative criteria to be considered. The criterion of maximum tensile stress, or alternatively the maximum rate of energy release theory, is commonly used for metal and resin type materials. For brittle material such as concrete, experiments[40] have shown that the maximum tensile strain criterion[41] is more appropriate and is therefore adopted herein. The circumferential strain factor $\tilde{\varepsilon}_\theta(\theta)$ for plane stress is employed; namely

$$\begin{aligned} \tilde{\varepsilon}_\theta(\theta) = {} & \frac{K_I}{E}\left[(3-5\nu)\cos\frac{\theta}{2} + (1+\nu)\cos\frac{3\theta}{2}\right] \\ & - \frac{K_{II}}{E}\left[(3-5\nu)\sin\frac{\theta}{2} + 3(1+\nu)\sin\frac{3\theta}{2}\right] \end{aligned} \tag{2.19}$$

The hypotheses of the maximum tensile strain criterion are: (a) crack extension is initiated at the tip in the radial direction θ_0 for which the circumferential strain factor is maximum, i.e.

$$\tilde{\varepsilon}_\theta(\theta_0)>0 \quad ; \quad \tilde{\varepsilon}_\theta'(\theta_0)=0 \quad ; \quad \tilde{\varepsilon}_\theta''(\theta_0)<0$$

and (b) the crack extends when K_I and K_{II} increase to cause the combined stress intensity factor K [defined by equation (2.23)] to reach the critical value representing the material fracture toughness. From equation (2.19), the extremum condition $\tilde{\varepsilon}_\theta'(\theta)=0$ is equivalent to

$$2\nu K_I p^3+2(3+4\nu)K_{II}p^2-(3+\nu)K_I p-(3+\nu)K_{II}=0 \tag{2.20}$$

where

$$p=\tan\frac{\theta_0}{2}$$

With $K_{II}=0$ and $\theta=0$ for the opening type crack mechanism, equation (2.19) leads to

$$\tilde{\varepsilon}_{\theta,cr}=\frac{4(1-\nu)}{E}K_{IC} \tag{2.21}$$

where K_{IC} represents the fracture toughness of the concrete. Thus, the existing crack will propagate if

$$\tilde{\varepsilon}_\theta(\theta_0)\geq\tilde{\varepsilon}_{\theta,cr}=\frac{4(1-\nu)}{E}K_{IC} \tag{2.22}$$

or, employing equation (2.19), the propagation criterion may also be written as

$$K=\frac{1}{4(1-\nu)}\{K_I[(3-5\nu)\cos\frac{\theta_0}{2}+(1+\nu)\cos\frac{3\theta_0}{2}]$$

$$-K_{II}[(3-5\nu)\sin\frac{\theta_0}{2}+3(1+\nu)\sin\frac{3\theta_0}{2}]\}\geq K_{IC} \tag{2.23}$$

in which θ_0 is given by equation (2.20) and K represents the stress intensity factor for the combined crack mechanism.

2.4 COMPARISON OF BEM WITH FEM FOR ACCURACY IN COMPUTING SIFS

In order to verify the accuracy of the BEM and study the appropriate length adopted for the crack tip elements, the stress intensity factors of a rectangular plate with a 3.5 m long edge crack shown in Figure 2.3 are computed for different L_c/a (where L_c is the length of the crack tip element and "a" is the crack length) by BEM and the results are plotted in Figure 2.4 (compared with collocation method whose error is within 1% [42]). It is seen from Figure 2.4 that K_I has better accuracy than K_{II}, and good accuracy (within 2% and 6% of error for K_I and K_{II}, respectively) is obtained when the length of the crack tip element is about 10% of the crack length.

To compare the efficiency and accuracy between BEM and FEM, the stress intensity factors of the plate are calculated by both methods. The BE and FE discretizations of the plate are shown in Figure 2.5 and the results obtained from DPS-8 computer are listed in Table 2.1. In the FEM, 8 node quadrilateral isoparametric elements are employed and the mid-node of those elements adjacent to the crack tip is moved to quarter point in order to improve accuracy[43].

It is seen from Table 2.1 that the input data and CPU time of FEM are 4.4 and 2.3 times those of BEM, respectively, whereas the accuracy is poorer than that of BEM, indicating that BEM is an efficient method having the advantages of higher accuracy, less CPU time and input data in computing stress intensity factors.

2.5 EXAMPLE ANALYSIS OF CRACK PROPAGATION FOR GRAVITY DAM

The stability and propagation of the crack near the heel of a 165 m high gravity dam under the loads of reservoir water pressure and the self-weight of the dam were analyzed by the proposed boundary element method. The cross-section of the dam and the coordinate system are shown in Figure 2.6 . The material properties of the dam and its base rock are listed in Table 2.2, and the dam is treated as a plane strain problem. Since accurate distribution pattern of the uplift pressure on the crack surfaces is not available at present, the rectangular distribution with full water head on the crack surfaces is assumed in the analysis. After the crack extends to the drainage of the dam located at x=15.0 m as shown in Figure 2.7(a), two cases are considered for the uplift pressure on the crack surfaces shown in Figure 2.7(b): (i) the drainage works well, thus the uplift pressure at the point of the drainage is zero, resulting in the triangular distribution of the uplift pressure on the crack surfaces; (ii) the drainage is blocked, and the distribution pattern remains rectangular. The former is a usual case in practical engineering, whereas the latter is an extreme case used herein to study the effect of the uplift pressure on the stability of the crack. The fracture toughness of the concrete K_{IC} is taken as 0.64 MPa·m$^{1/2}$ based on the experiments of Reference [44].

Horizontal initial cracks of 2 m length are assumed on the upstream face of the dam at two elevations 15.0 m and 20.0 m, respectively, as shown in Figure 2.7(a) for parameter study. The BE discretization of the dam and its foundation for crack 2 is shown in Figure 2.8 where the infinite boundary elements were employed to model the remote region of the foundation[45]. The propagation process is analyzed stage by stage for the two cracks, respectively. During these crack extensions, the dam is remeshed automatically by the program. The crack profiles are shown in Figure 2.9 and the stress intensity factors during the crack propagation are illustrated in Figure 2.10. It is evident from Figure 2.9 that the horizontal crack near the heel of the dam propagates rapidly downwards to the interface between the dam and the base. From Figure 2.10, it is seen that: (i) K_{II} is much smaller than K_I, resulting in the almost identical K_I with the combined stress intensity factor K; (ii) K_I and K increase monotonically as the crack develops forward, indicating that the crack will extend all the way down to the dam-foundation interface once it becomes unstable.

Usually the interface is relatively weak, and if the base rock is intact, one can assume that the crack will propagate along the weak interface after it reaches there. From the computation results shown in Table 2.3, it is seen that the crack becomes a compression-shear type (negative K_I) quickly after it develops along the interface. No further investigation is performed since the criterion for compression-shear type crack propagation is not well established and the example here is employed only to demonstrate the feasibility of the present approach in simulating tension-shear type crack propagation. Comparing the two cases in Table 2.3, it is seen that the K_I at x=15.0 m in case 1 is less than the K_I at x=40.0 m in case 2, indicating that the distribution pattern of the uplift pressure on the crack surfaces has a significant effect on the stress intensity factor K_I and that the effective drainage system near the heel of the dam plays an important role in resisting crack propagation.

2.6 CONCLUDING REMARKS

Based on the foregoing good accuracy and high efficiency of the BE approach in solving 2-D static cracking problems, the above procedure is extended to treat 2-D dynamic crack problems in concrete gravity dams in the following Chapter.

Table 2.1 Comparison of BEM with FEM

Method	BEM	FEM
K_I (kPa $m^{1/2}$)	340	318
Error (%)	2.0	4.7
K_{II} (kPa $m^{1/2}$)	41.5	39.0
Error (%)	7.0	12.5
CPU time (second)	12.2	27.7
No. of Input data	381	1671
Discretization	NE=20, NP=43	NE=48, NP=177

Note: NE and NP represent the number of elements and the number of nodes respectively.

Table 2.2 Material properties of gravity dam

Property Material	Elastic modulus (MPa)	Poisson ratio	Specific weight (kN/m^3)
Dam concrete	26, 000	0.17	23.5
Foundation rock	39, 000	0.20	25.9

Table 2.3 Crack propagation along the interface for crack 1

Case	Crack-tip coordinates		K_I (MPa $m^{1/2}$)	K_{II} (MPa $m^{1/2}$)
	x (m)	y (m)		
1	15.0	10.0	-8.00	4.37
2	20.0	10.0	1.68	5.56
	40.0	10.0	-6.39	11.09

Note: Case 1 and 2 correspond to triangular and rectangular distribution of uplift pressure in crack, respectively.

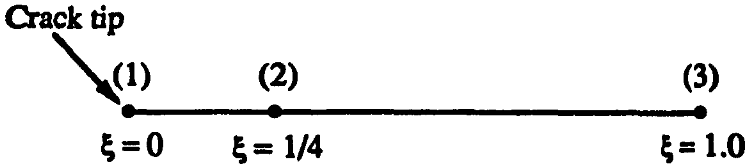

(a) Quarter point element

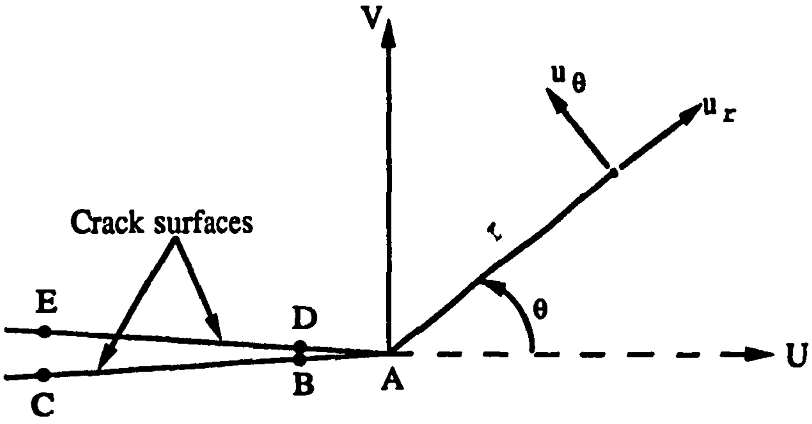

(b) Crack tip coordinate system

Figure 2.1 BE crack tip discretization

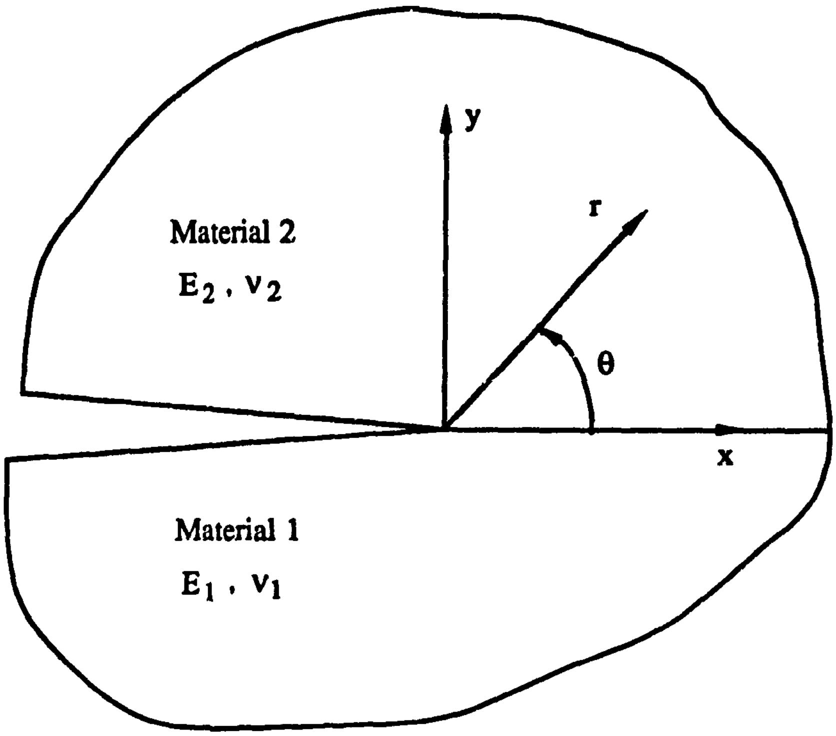

Figure 2.2 Crack on the interface of two different materials

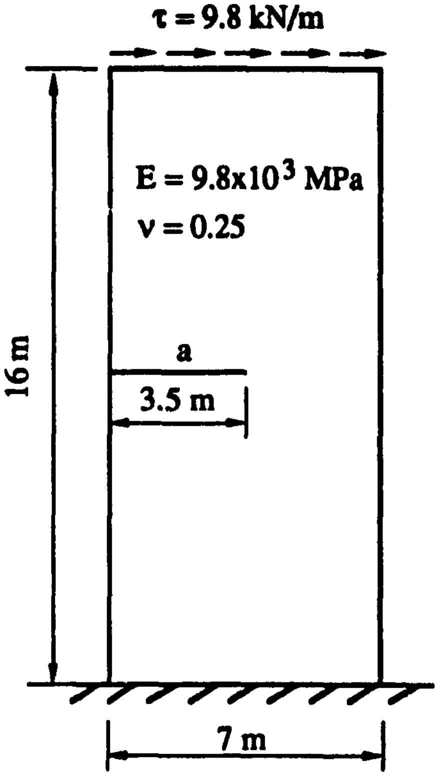

Figure 2.3 Rectangular plate with edge crack

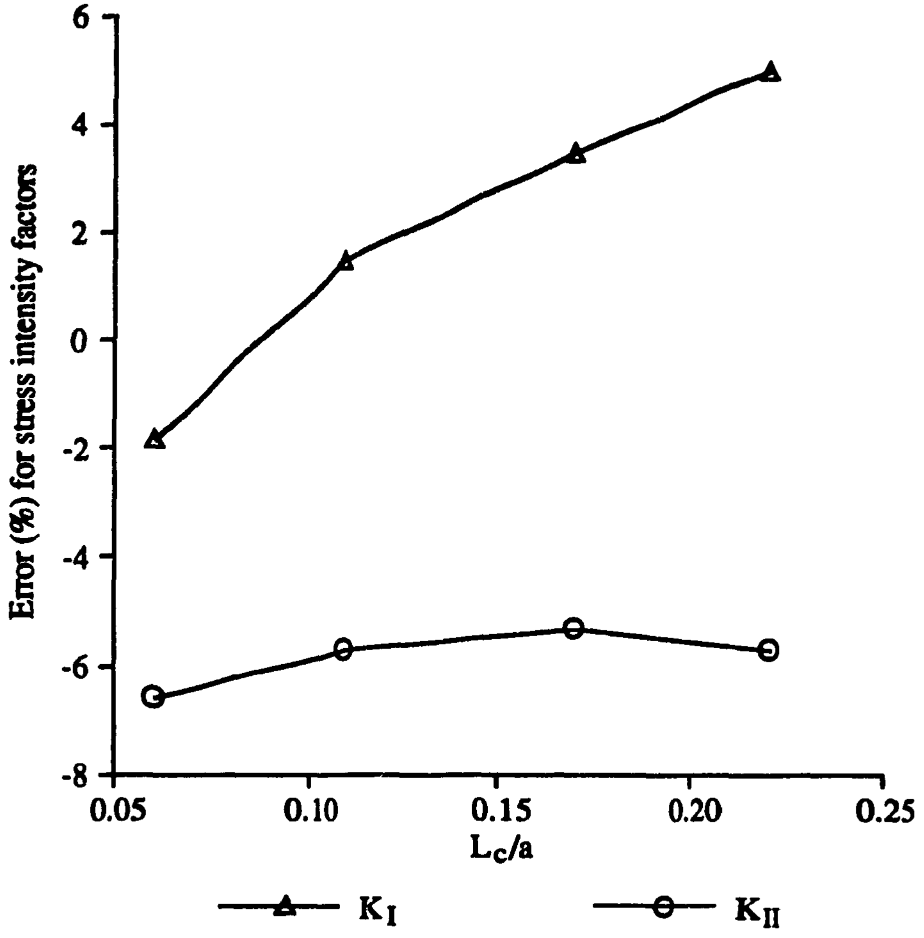

Figure 2.4 Accuracy of BEM in computing SIFs

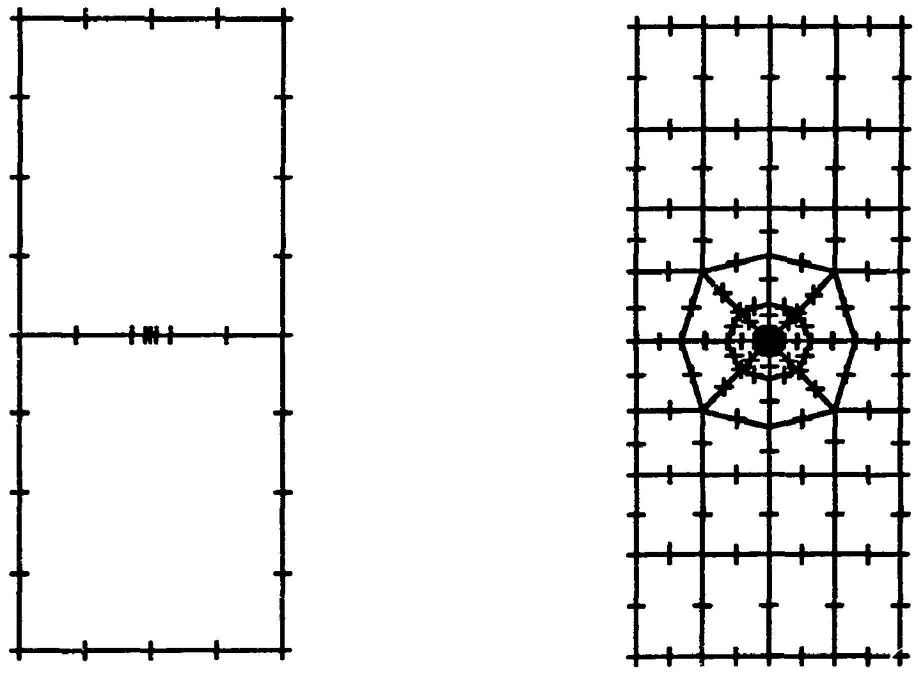

(a) BE discretization

(b) FE discretization

Figure 2.5 Discretizations of plate

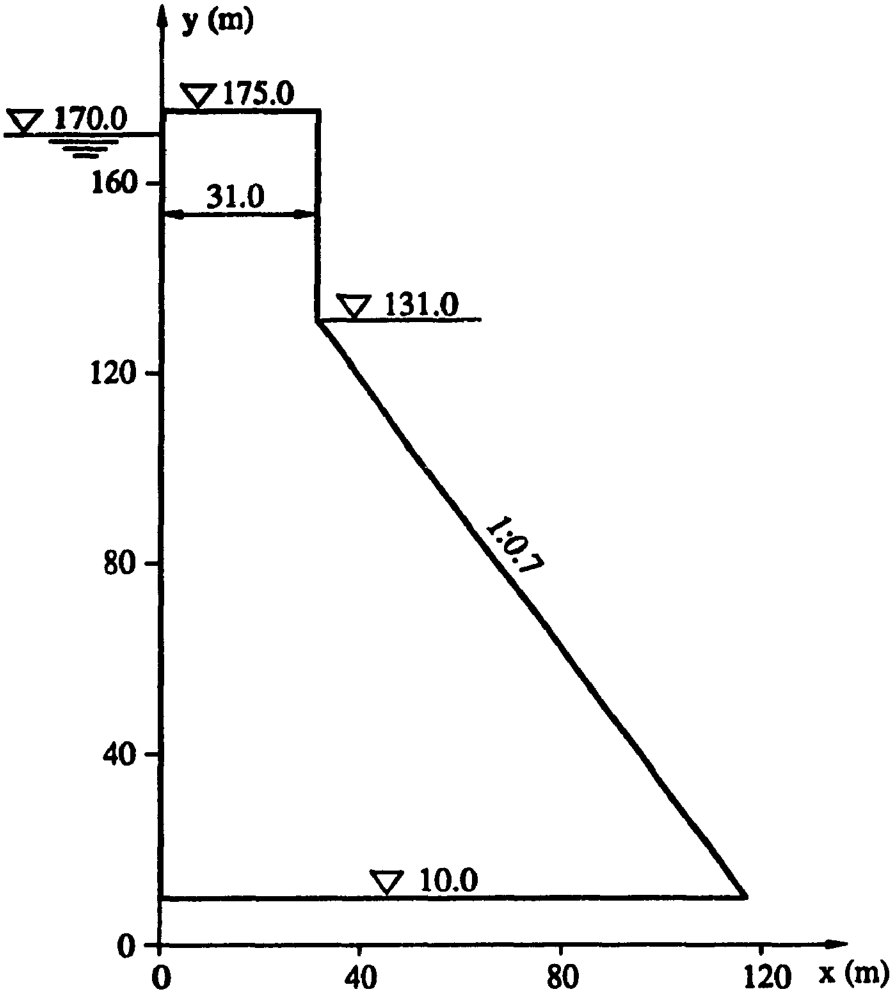

Figure 2.6 Cross-section of the dam and coordinate system

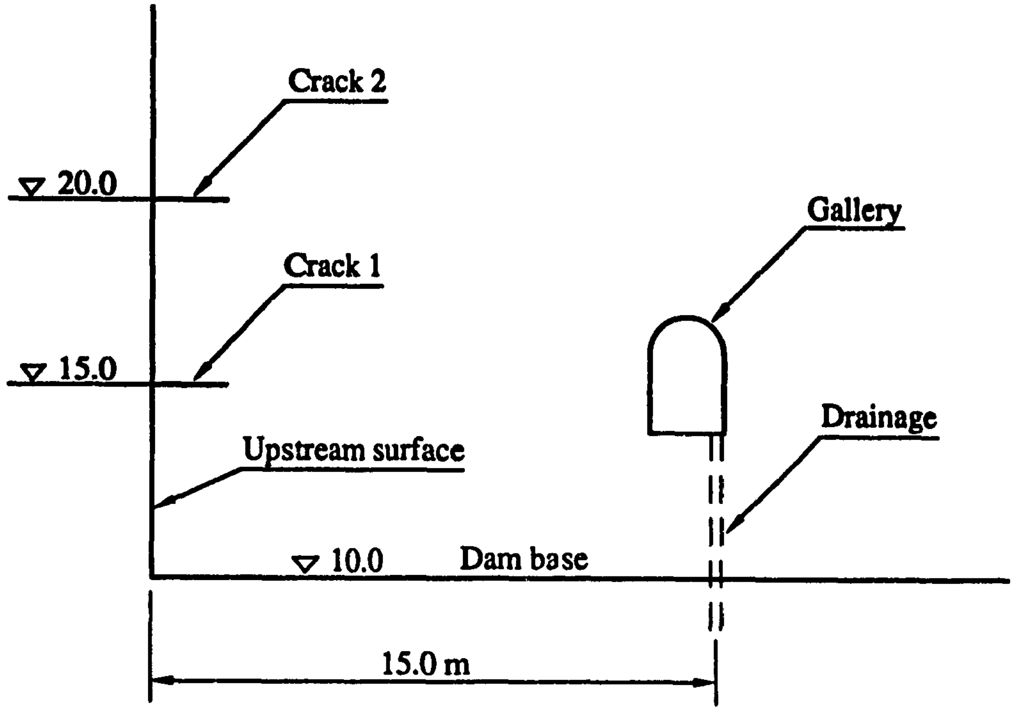

(a) Locations of the gallery, the drainage and the initial cracks

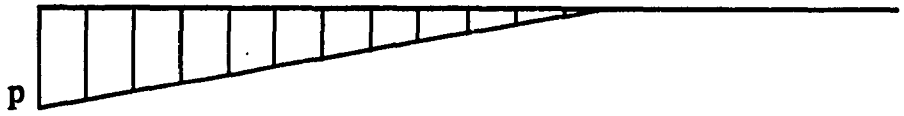

Case 1: Triangular distribution

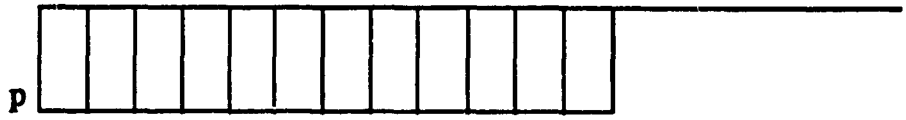

Case 2: Rectangular distribution

(b) Distribution pattern of the uplift pressure in crack

Figure 2.7 Details near the heel of the dam

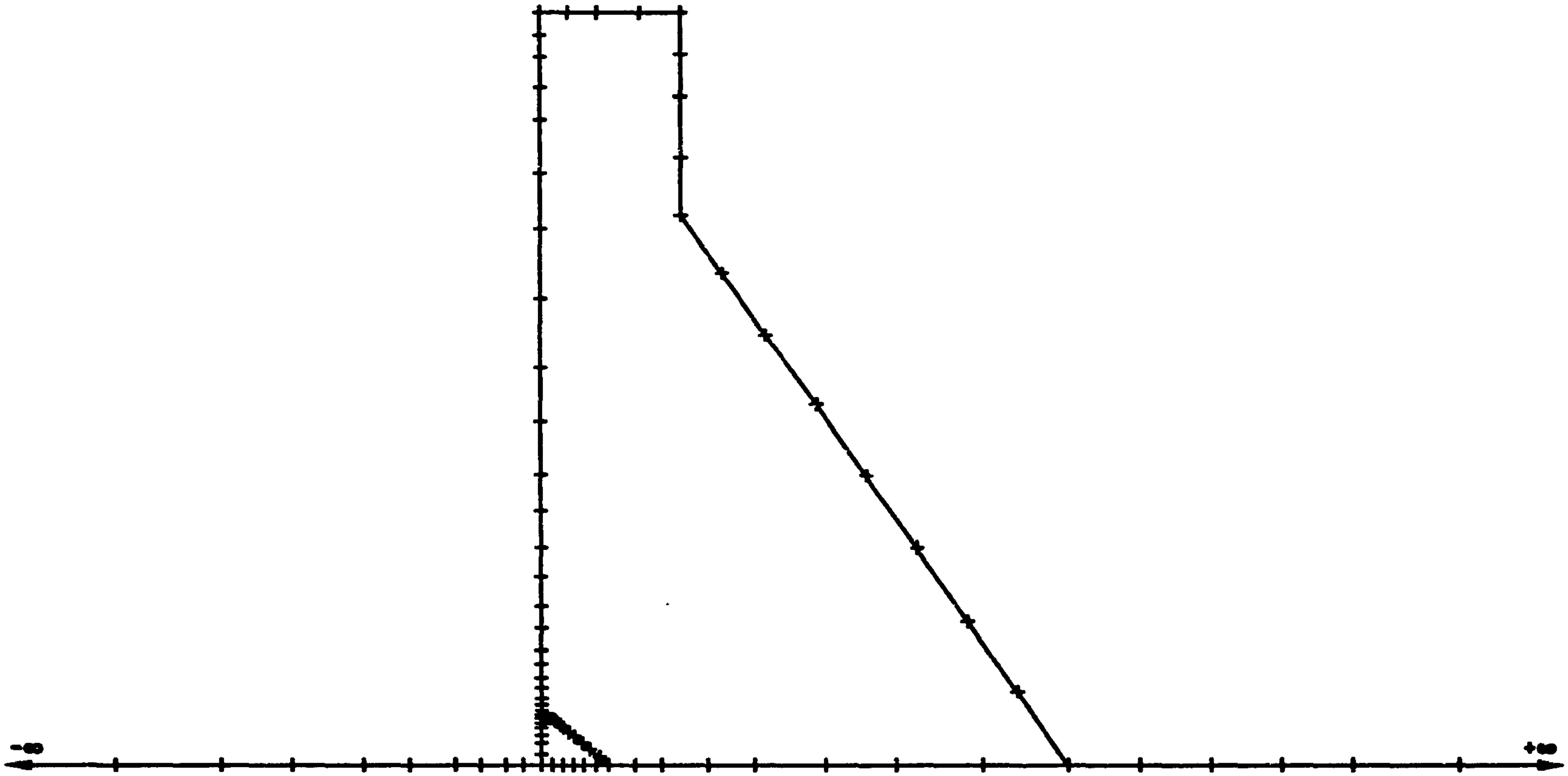

Figure 2.8 BE discretization of the dam

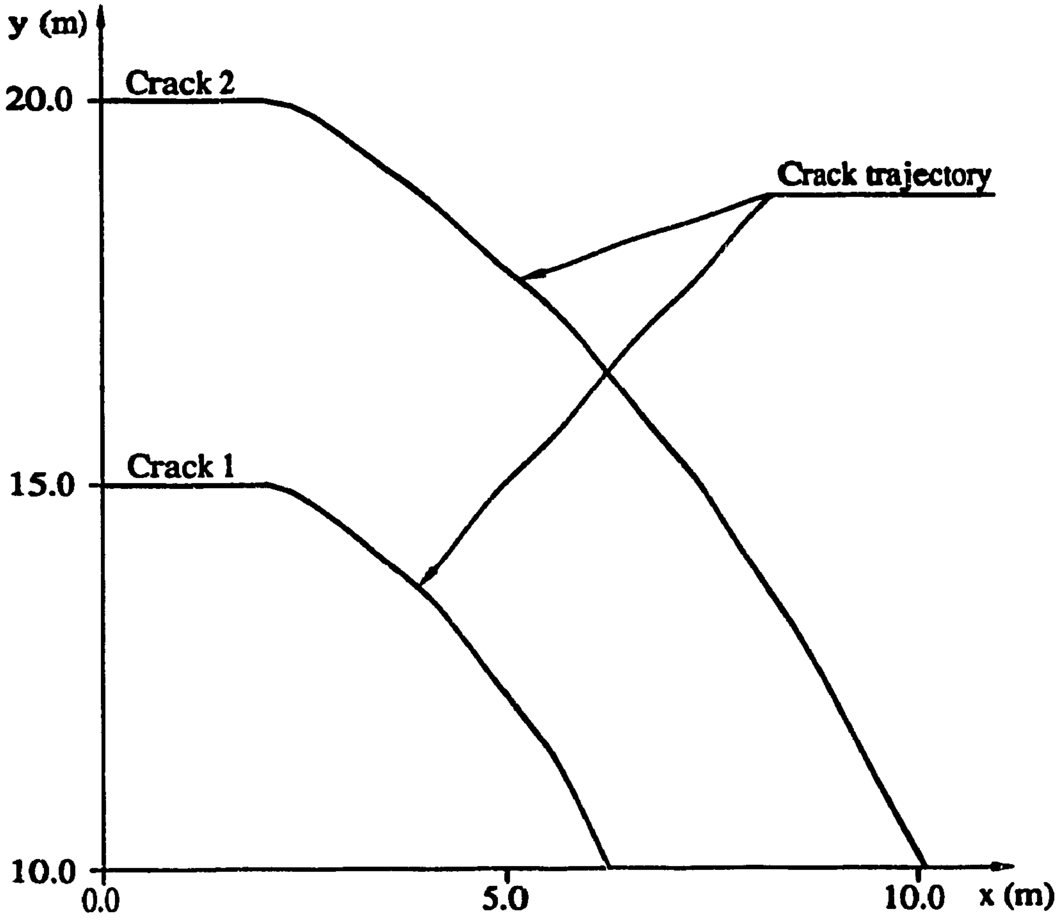

Figure 2.9 Crack profiles of the dam

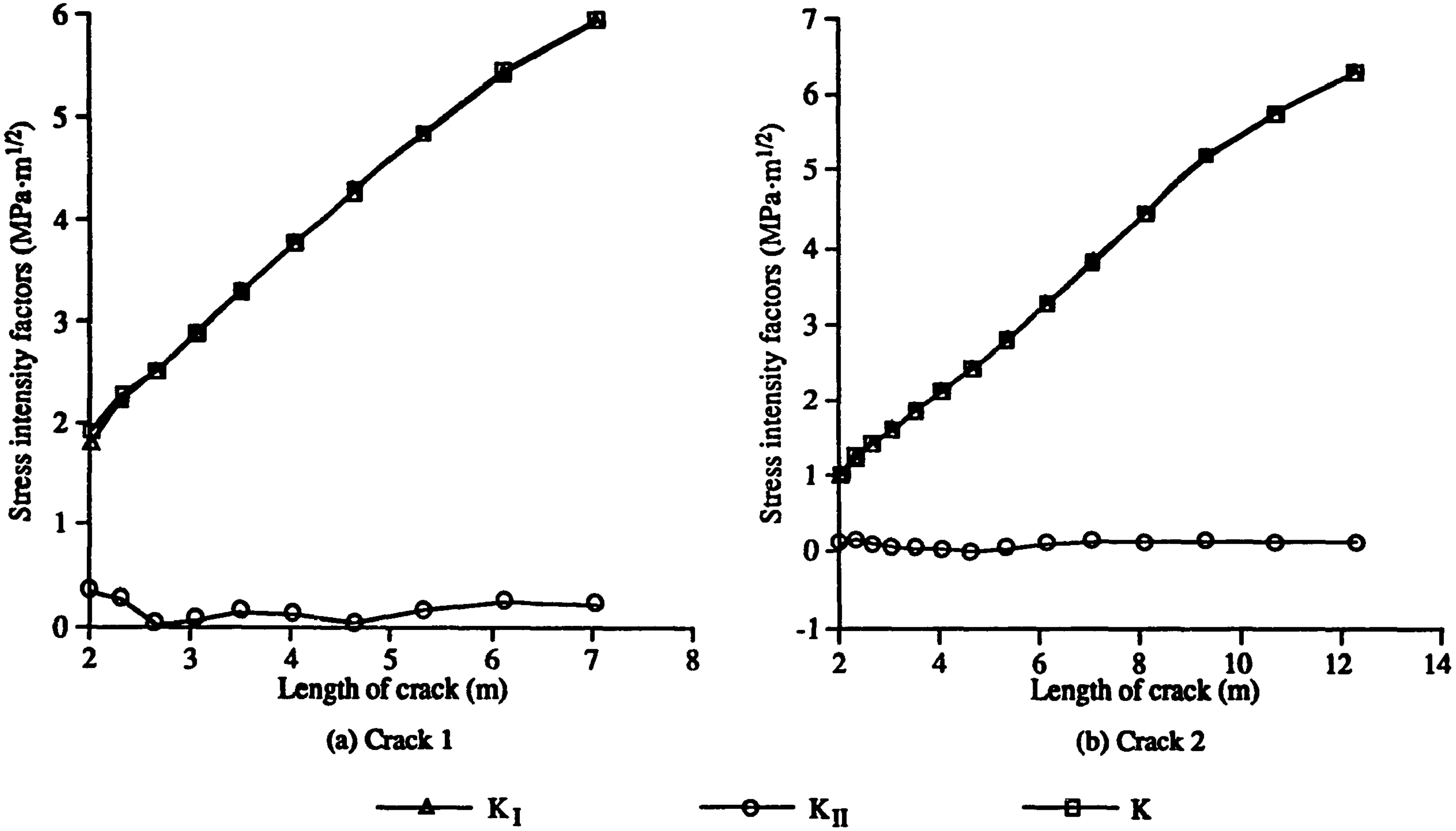

(a) Crack 1

(b) Crack 2

Figure 2.10 Stress intensity factors of the dam

CHAPTER 3

2-D FRACTURE ANALYSIS OF GRAVITY DAMS UNDER STRONG EARTHQUAKES

This Chapter extends the 2-D static fracture analysis presented in Chapter 2 to the detailed evaluation of the fracture process of concrete gravity dams during strong earthquakes. The boundary element technique for seismic cracking is formulated, based also on the principles of linear elastic fracture mechanics. The technique takes advantage of both the high accuracy of the BEM in the computation of stress intensity factors and the ease in remeshing the crack tip discretization. The nonlinear process of crack extension is modelled in a stage by stage procedure. Since the impact effect of crack closing is simulated by impulse and force rather than by change in stiffness, the mode superposition technique is still in effect within each stage of constant crack length. Generally, the proposed method is efficient for the analysis of seismic crack propagation under earthquake loadings, due primarily to simplification of the nonlinear dynamic problem resulting from the linearized nature of the present formulation combined with the computational advantages of BE modal analysis.

To study the feasibility and accuracy of the procedure, comparisons are made with previously obtained experimental data from rupture tests at Tsinghua University of a cantilever beam and a model of Koyna dam both made of gypsum and under excitation of a shaking table. The very good agreement obtained between the numerical predictions and test results indicates that the proposed procedure is suitable for evaluation of the 2-D seismic fracture process in concrete gravity dams.

3.1 BOUNDARY ELEMENT FORMULATION OF 2-D ELASTODYNAMICS

Without taking the constant body forces into account, the dynamic equilibrium equation for a 2-D linear elastic system is given by

$$\sigma_{lj,j} - \rho\, \ddot{u}_l = 0 \qquad (j, l = 1, 2) \tag{3.1}$$

where ρ is the mass density and $\ddot{u}_l$ is the acceleration component in the l-direction.

For solving equation (3.1) by the BEM, one of the simplified methods was developed by Nardini and Brebbia[46] and subsequently extended to treat seismic input problems in Reference [47]. By using the Kelvin fundamental solution for static problems as the weighting function and making use of the residual approximation the integral form of equation (3.1) becomes

$$\int_\Omega \sigma_{lj,j}(Q)\, u^*_{kl}(P,Q)\, d\Omega(Q) - \rho \int_\Omega \ddot{u}_l(Q)\, u^*_{kl}(P,Q)\, d\Omega(Q) = 0 \tag{3.2}$$

in which P and Q represent the source and field points, respectively. The first integral of equation (3.2) is related to the static part of the problem as follows:

$$\int_\Omega \sigma_{lj,j}(Q)\, u^*_{kl}(P,Q)\, d\Omega(Q) = -C_{kl}(P)\, u_l(P)$$

$$- \int_\Gamma p^*_{kl}(P,Q)\, u_l(Q)\, d\Gamma(Q) + \int_\Gamma u^*_{kl}(P,Q)\, p_l(Q)\, d\Gamma(Q) \tag{3.3}$$

where C_{kl} are coefficients related to the geometry of the boundary; u^*_{kl} and p^*_{kl} constitute the Kelvin solution pair given by equation (2.2); and u_l and p_l are displacements and tractions on the boundary. For the second integral of equation (3.2), a linear combination of a class of functions $f^j(Q)$ can be used to describe the acceleration field in the domain[46], i.e.

$$\ddot{u}_l(t,Q)=\ddot{\alpha}_{lj}(t)f^j(Q) \tag{3.4}$$

in which $\ddot{\alpha}_{lj}(t)$ is a group of coefficients depending on time t. Applying equation (3.4) to all nodal points yields the vector expression

$$\{\ddot{u}\}=[F]\{\ddot{\alpha}\}$$

or, if the functions $f^j(Q)$ are linearly independent and their number is chosen to be equal to the number of nodes

$$\{\ddot{\alpha}\}=[F]^{-1}\{\ddot{u}\}=[E]\{\ddot{u}\} \tag{3.5}$$

The selection of functions $f^j(Q)$ involves several alternatives. One of the simplest set is given by: $f^j(Q) = C - R(P_j, Q)$, where $R(P_j, Q)$ is the distance between source point P_j and field point Q and C is a constant. From the experience of References [46] and [47], this approximation for $f^j(Q)$ to depict the inertial field provides reasonable accuracy in the structural response. For practical ranges of distance R, the role of C is not particularly important; thus C = 1.0 is assumed (indeed C = 0 would also have been a suitable choice).

To reduce the second domain integral of equation (3.2) to a boundary integral, one can define a displacement field ζ^j_{il} and related stress field τ^j_{ilm} such that

$$\tau^j_{ilm,m}=\delta_{il}f^j(Q) \tag{3.6}$$

in which δ_{il} is the Kronecker delta.

From equations (3.4) and (3.6), the second integral of equation (3.2) can be derived as the boundary integral

$$\int_\Omega \ddot{u}_l(Q)u^*_{kl}(P,Q)\,d\Omega(Q)=\ddot{\alpha}_{ij}\int_\Omega \delta_{il}f^j(Q)\,u^*_{kl}(P,Q)\,d\Omega(Q)$$

$$
\begin{aligned}
&=\ddot{\alpha}_{ij}\int_{\Omega}\tau^{j}_{ilm,m}(Q)u^{*}_{kl}(P,Q)\,d\Omega(Q) \\
&=\ddot{\alpha}_{ij}\Big[-C_{kl}\,\zeta^{j}_{il}(P)+\int_{\Gamma}u^{*}_{kl}(P,Q)\eta^{j}_{il}(Q)\,d\Gamma(Q) \\
&\qquad\qquad\qquad-\int_{\Gamma}p^{*}_{kl}(P,Q)\zeta^{j}_{il}(Q)\,d\Gamma(Q)\Big] \qquad (3.7)
\end{aligned}
$$

where $\eta^{j}_{il}=\tau^{j}_{ilm}n_{m}$ represents the boundary traction related to the displacement field ζ^{j}_{il} and n_m is the direction cosine of the boundary normal. Substituting equations (3.3) and (3.7) into equation (3.2) leads to the following integral expression for dynamic problems:

$$
\begin{aligned}
&C_{kl}(P)u_{l}(P)+\int_{\Gamma}p^{*}_{kl}(P,Q)u_{l}(Q)\,d\Gamma(Q) \\
&-\int_{\Gamma}u^{*}_{kl}(P,Q)p_{l}(Q)\,d\Gamma(Q)+\rho\,\ddot{\alpha}_{ij}(t)\Big[-C_{kl}(P)\zeta^{j}_{il}(P) \\
&+\int_{\Gamma}u^{*}_{kl}(P,Q)\eta^{j}_{il}(Q)\,d\Gamma(Q)-\int_{\Gamma}p^{*}_{kl}(P,Q)\zeta^{j}_{il}(Q)\,d\Gamma(Q)\Big]=0 \qquad (3.8)
\end{aligned}
$$

By discretizing boundary Γ and using interpolation functions, equation (3.8) can be transformed to the matrix form

$$[H]\{u\}+[M]\{\ddot{u}\}=[G]\{p\} \qquad (3.9)$$

where [H], [G] are coefficient matrices related to elasto-static problems; $\{u\}$, $\{\ddot{u}\}$ are vectors of displacement and acceleration, respectively; $\{p\}$ represents tractions on the boundary expressed as two global quantities per node; and [M] denotes an inertial matrix which has the form

$$[M]=\rho([G][\eta]-[H][\zeta])[E] \qquad (3.10)$$

With $\{Q\}$ defined as the vector of nodal forces, the relation between $\{Q\}$ and $\{p\}$ becomes

$$\{ Q \} = [N] \{ p \} \tag{3.11}$$

where $[N]$ is the transformation matrix derived from element interpolation functions. After pre-multiplying equation (3.9) by $[N]\,[G]^{-1}$, one obtains

$$[k] \{ u \} + [m] \{ \ddot{u} \} = \{ Q \} \tag{3.12}$$

where

$$\begin{aligned} [k] &= [N] [G]^{-1} [H] \\ [m] &= [N] [G]^{-1} [M] \end{aligned} \tag{3.13}$$

Partitioning equation (3.12) and letting $\{u_1\}$, $\{\ddot{u}_1\}$ denote the unknown and $\{u_2\}$, $\{\ddot{u}_2\}$ the known displacements and accelerations lead to

$$\begin{bmatrix} k_{11} & k_{12} \\ k_{21} & k_{22} \end{bmatrix} \begin{Bmatrix} u_1 \\ u_2 \end{Bmatrix} + \begin{bmatrix} m_{11} & m_{12} \\ m_{21} & m_{22} \end{bmatrix} \begin{Bmatrix} \ddot{u}_1 \\ \ddot{u}_2 \end{Bmatrix} = \begin{Bmatrix} Q_1 \\ Q_2 \end{Bmatrix} \tag{3.14}$$

The first of equations (3.14) is for the displacement response

$$[k_{11}] \{ u_1 \} + [k_{12}] \{ u_2 \} + [m_{11}] \{ \ddot{u}_1 \} + [m_{12}] \{ \ddot{u}_2 \} = \{ Q_1 \} \tag{3.15}$$

while the second equation is for unknown nodal forces $\{Q_2\}$ on the input boundary. The reservoir dynamic pressure can be modelled[48]-[50] by adding mass to matrix $[m_{11}]$. Since it is a normal procedure, it will not be described here.

From equation (3.15), the free vibration equation has the form

$$[k_{11}] \{ X \} - \omega^2 [m_{11}] \{ X \} = 0 \tag{3.16}$$

or

$$[A]\{X\}=\lambda\{X\} \tag{3.17}$$

where

$$[A]=[k_{11}]^{-1}[m_{11}] \;;\qquad \lambda=1/\omega^2 \tag{3.18}$$

The subspace iteration method can be employed to obtain the eigenvalues and eigenvectors of equation (3.17), which represent the natural frequencies and mode shapes of the structure.

For the earthquake input mechanism, either rigid foundation input or base rock input (Figure 3.1) can be considered. The latter assumes uniform earthquake motion along base rock boundary ABC as the input with the foundation rock itself treated as massless.

Assuming that $\ddot{u}^o_{x1}$ and $\ddot{u}^o_{x2}$ represent base rock accelerations in the x_1 and x_2 directions, and letting $\{u^o\}=\{u^o_{x1}\;\;u^o_{x2}\}^T$ lead to

$$\begin{aligned}\{u_1\}&=\{u_r\}+[B']\{u^o\}\\ \{u_2\}&=[B]\{u^o\}\end{aligned} \tag{3.19}$$

where $\{u_r\}$ is the relative displacement vector with reference to ground motion and

$$[B]=\begin{bmatrix}1&0&1&0&\dots&1&0\\0&1&0&1&\dots&0&1\end{bmatrix}^T$$

Matrix $[B']$ of the first of equations (3.19) has the same form as $[B]$ but its size is different due to the partitioning of the degrees of freedom separating the base rock boundary from the remainder of the system. Substituting equation (3.19) into equation (3.15) and noting that the rigid displacement does not produce internal forces yields

$$[m_{11}]\{\ddot{u}_r\}+[k_{11}]\{u_r\}=[F']\{\ddot{u}^o\}+\{Q_1\} \tag{3.20}$$

in which

$$[F'] = -([m_{11}][B'] + [m_{12}][B]) \tag{3.21}$$

Pre-multiplying equation (3.20) by $[k_{11}]^{-1}$ gives

$$[A]\{\ddot{u}_r\} + \{u_r\} = [k_{11}]^{-1}[F']\{\ddot{u}^o\} + [k_{11}]^{-1}\{Q_1\} \tag{3.22}$$

Displacement $\{u_r\}$ can be expressed as the sum of the modal components

$$\{u_r\} = \{\phi_1\}Y_1 + \{\phi_2\}Y_2 + \ldots + \{\phi_m\}Y_m = [\phi]\{Y\} \tag{3.23}$$

in which $[\phi]$ is the mode shape matrix and $\{Y\}$ represents the generalized coordinates.

Substituting equation (3.23) into equation (3.22) and applying the relation

$$[A][\phi] = [\phi][\lambda]$$

yields

$$\{\ddot{Y}\} + [\lambda]^{-1}\{Y\} = [\lambda]^{-1}[\psi]^T[F']\{\ddot{u}^o\} + [\lambda]^{-1}[\psi]^T\{Q_1\} \tag{3.24}$$

where

$$[\psi]^T = ([\phi]^T[\phi])^{-1}[\phi]^T[k_{11}]^{-1} \tag{3.25}$$

The new symbol η_k is now defined as the modal participation factor, i.e. $\{\eta_k\}^T = \omega_k^2 \{\psi_k\}^T[F']$. Setting $\lambda_k = 1/\omega_k^2$ and introducing damping ratio ξ_k provide the following generalized equation of motion for mode k:

$$\ddot{Y}_k + 2\xi_k\omega_k\dot{Y}_k + \omega_k^2 Y_k = \{\eta_k\}^T\{\ddot{u}^o\} + \omega_k^2\{\psi_k\}^T\{Q_1\} \tag{3.26}$$

When static loads consisting of the self-weight of the structure and the hydrostatic pressure are included, equation (3.26) becomes

$$\ddot{Y}_k + 2\xi_k\omega_k\dot{Y}_k + \omega_k^2 Y_k = \{\eta_k\}^T\{\ddot{u}^o\} + \omega_k^2\{\psi_k\}^T\{Q_1\} + \omega_k^2\{\psi_k\}^T\{Q_s\} \tag{3.27}$$

where $\{Q_s\}$ represents the nodal forces caused by the static loads. It is a vector of constant elements for each stage of the crack length obtained from BE static analysis. Substituting the initial conditions

$$\ddot{Y}_k=\dot{Y}_k=\{\ddot{u}^0\}=\{Q_1\}=0 \tag{3.28}$$

into equation (3.27) leads to the following generalized coordinate for the initial displacements:

$$Y_k = \{\psi_k\}^T \{Q_s\} \tag{3.29}$$

Since only the lowermost modes suffice to obtain accurate estimates of stresses in gravity dams subjected to earthquake excitation, this transformation to generalized coordinates is computationally more efficient than the alternative of direct integration of the coupled equations of motion. Even though a new eigenvalue problem must be solved each time the crack extends, subspace iteration minimizes this effort.

3.2 SIMULATION OF CRACK CLOSURE DURING EARTHQUAKES

The crack opening and closing process of a dam structure during earthquake excitation poses a problem of a complicated nonlinear nature. The nonlinearity is due not only to the stiffness variation accompanying progressive crack extension but also to the alternate opening and closing of the crack. In modeling a discrete crack by a numerical technique such as the BE method used in this study, the two crack surfaces are represented as traction free boundaries. Thus, correct representation of the opening phase of the crack is inherent in the numerical model. For simulation of the behaviour during crack closing two alternative methods, namely the impulse and the force methods, are developed.

Modelling of crack closure by impulse method

For simplification of the problem, Reference [51] used a load pulse to simulate the effect of impact at the instant of closing of the crack for finite element discretization. Described below is the extension of this concept to the present BE formulation.

Consider the cracked dam structure shown in Figure 3.2. A partial crack exists at a certain elevation on the downstream face. Points i and j belong to the upper and lower banks of the crack, respectively, and represent a pair of adjacent nodes along the crack. When the structure deforms in the upstream direction, the crack opens; on the other hand, when the structure deforms in the downstream direction an idealized structure is assumed to replace the real system. This idealized structure has exactly the same parameters as the cracked dam but allows the crack surfaces to overlap, with a load pulse acting at all those points i and j which touch each other during closing of the crack. Thus, the cracked system and its stiffness characteristics remain unchanged. By using this approximation, the system remains linear and the mode superposition technique is still in effect within each stage of constant crack length. By dividing the process of crack extension into suitably small stages and re-evaluating the system frequencies and mode shapes at each stage, the complicated nonlinear problem can be solved by linear techniques.

When impact occurs between nodal points i and j, the load at these nodes due to the impact can be expressed as

$$\{Q_1\} = \sum_{n=1}^{N} \{P_n\} \delta(t-t_n) \qquad (3.30)$$

where $\{P_n\}$ is the n^{th} amplitude vector of the load pulse and only has values at points i and j; t_n is the arrival instant of the n^{th} pulse; N represents the number of pulses; and $\delta(t-t_n)$ is the Dirac delta function. Here it should be noted that, although a general boundary element formulation would require the use of tractions along the crack surfaces, the present formulation permits the direct application of the nodal forces of equation (3.30). This is possible without causing analytical singularities because governing (discretized) equation (3.9) has been transformed to the nodal force form given by equation (3.20).

Substituting equation (3.30) into equation (3.27) yields

$$\ddot{Y}_k+2\,\xi_k\omega_k\dot{Y}_k+\omega_k^2Y_k=\{\eta_k\}^T\{\ddot{u}^o\}+\omega_k^2\{\psi_k\}^T\{Q_s\}$$

$$+\sum_{n=1}^{N}\omega_k^2[\psi_{kr}(i)-\psi_{kr}(j)]P_n(t)\delta(t-t_n) \qquad (3.31)$$

where $\psi_{kr}(i)$, $\psi_{kr}(j)$ are component values of ψ_k at points i and j in the r-direction and ω_k, ξ_k, η_k are the frequency, damping ratio and participation factor of the kth mode related to the hypothetical linear system.

Equation (3.31) can be solved by employing the Duhamel integral to give

$$Y_k=\{\psi_k\}^T\{Q_s\}+\frac{1}{\omega_{kd}}\int_0^t[\{\eta_k\}^T\{\ddot{u}^o(\tau)\}+\omega_k^2\{\psi_k\}^T\{Q_s\}]\exp[-\xi_k\omega_k(t-\tau)]\sin[\omega_{kd}(t-\tau)]\,d\tau$$

$$+\sum_{n=1}^{N}\frac{S_n(t_n)\,\omega_k^2[\psi_{kr}(i)-\psi_{kr}(j)]}{\omega_{kd}}\sin[\omega_{kd}(t-t_n)]\exp[-\xi_k\omega_k(t-t_n)]\,H(t-t_n) \qquad (3.32)$$

where

$$\omega_{kd}=\omega_k\sqrt{1-\xi_k^2}$$

$$S_n(t_n)=\int_{t_n^-}^{t_n^+}P_n\delta(t-t_n)\,dt \qquad (3.33)$$

$$H(t-t_n)=\begin{cases}1\,, & t-t_n>0\\ 0\,, & t-t_n\leq 0\end{cases} \qquad (3.34)$$

in which t_n^- and t_n^+ are the time instants before and after impact. The criterion for specifying the time instant of impact t_n is represented by

$$\begin{aligned} &u_r[i](t_n)=u_r[j](t_n) \\ &\dot{u}_r[i](t_n)<\dot{u}_r[j](t_n) \end{aligned} \tag{3.35}$$

where $u_r[i]$ and $u_r[j]$ are displacements and $\dot{u}_r[i]$ and $\dot{u}_r[j]$ are velocities of points i and j in the r-direction. The first of equations (3.35) represents the condition of incipient contact between two nodes, whereas the second indicates that impact will take place only if the two crack surfaces are moving toward each other, rather than apart. During the closing process, all pairs of nodes along the crack need to be examined t each time step. If both criteria of equation (3.35) are satisfied for a nodal pair, a load pulse is applied at that location. Thus the criteria for crack closure are applied continuously along the length of the crack. It is also to be noted that these criteria pertain only to the direction normal to the crack; shear displacements along the crack occur but do not govern crack closure.

To determine the expression for the impulse magnitude $S_n(t_n)$, the principles of both impulse-momentum and conservation of energy are employed.

First, integrating equation (3.31) over time t_n^- to t_n^+ and noting that the generalized coordinate Y_k is assumed not to change within this infinitesimal period allows the corresponding increment of generalized velocity $\Delta\dot{Y}_k$ to be represented in terms of impulse $S_n(t_n)$, thus implying the application of the impulse-momentum principle. This yields

$$\Delta\dot{Y}_k=S_n(t_n)\,\omega_k^2[\psi_{kr}(i)-\psi_{kr}(j)] \tag{3.36}$$

To next establish the relationship between $\Delta\dot{Y}_k$ and the velocity field $\dot{Y}_k^-$ just prior to impact, energy conservation is assumed as follows.

For a linear elastic system where neither material damage nor friction is assumed to occur along the crack surfaces, the energy loss during the instant of impact of nodal pair i and j may be ignored. Total energy thus remains constant during impact of individual nodal pairs. This approximation applies only at the times of impact of node pairs and not during the total time the crack remains closed; during the latter energy loss is not negligible and is accounted for through the viscous damping mechanism.

The total energy comprising strain and kinetic energies is thus assumed to be unchanged before and after the occurrence of each impact. Assuming the structure be an idealized elastic system, the deformation due to impact will be completely restored during a finite time interval $\Delta t_n = t_n^+ - t_n^-$. As Δt_n approaches zero, the impulse acting at the contact nodes approaches a δ function, thus implying that deformation around the crack region due to impact will occur only after the time of the idealized impulse. From this, it is clear that the strain energy may be assumed constant during these intervals. The latter leads to the total kinetic energy of the system unchanged also during the time of impact when a node pair along the crack comes into contact; thus

$$E(t_n^+) - E(t_n^-) = 0 \tag{3.37}$$

where

$$\begin{aligned} E(t_n^-) &= \frac{1}{2}\{\dot{Y}^-\}^T([\phi]^T[m_{11}][\phi])\{\dot{Y}^-\} \\ E(t_n^+) &= \frac{1}{2}(\{\dot{Y}^-\}^T + \{\Delta\dot{Y}\}^T)([\phi]^T[m_{11}][\phi])(\{\dot{Y}^-\} + \{\Delta\dot{Y}\}) \end{aligned} \tag{3.38}$$

in which $E(t_n^-)$ and $E(t_n^+)$ are the kinetic energies of the structure before and after impact.

Combining equations (3.36) - (3.38) yields

$$S_n(t_n) = -\frac{\{\gamma\}^T([\phi]^T[m_{11}][\phi] + [\phi]^T[m_{11}]^T[\phi])\{\dot{Y}^-\}}{\{\gamma\}^T([\phi]^T[m_{11}][\phi])\{\gamma\}} \tag{3.39}$$

where

$$\{\gamma\} = \{\gamma_1, \gamma_2, \ldots, \gamma_m\}^T$$

$$\gamma_k = \omega_k^2 [\psi_{kr}(i) - \psi_{kr}(j)]$$

$$\{\Delta\dot{Y}\} = \{\Delta\dot{Y}_1, \Delta\dot{Y}_2, \ldots, \Delta\dot{Y}_m\}^T = S_n(t_n)\{\gamma\}$$

Hence, by using equations (3.32) and (3.39) the response of the cracked structure can be evaluated by the mode superposition technique within one stage of crack extension.

Modelling of crack closure by force method

Whereas the impulse method relies on load pulses to simulate the effect of crack closure while permitting hypothetical overlap, in the force method nodal forces are applied on the two crack surfaces in order to bring these back into contact. The magnitudes of the required forces are obtained by an iteration process.

Let i and j represent the two banks of the crack which have opposite nodes on the upper and lower surfaces, respectively, as shown in Figure 3.2. With r denoting the direction normal to the crack surface, the relative normal displacement Δu_{ij} between any pair of nodes at time t can be written as

$$\Delta u_{ij}(t) = u_{ri}(t) - u_{rj}(t) \tag{3.40}$$

where $u_{ri}(t)$ and $u_{rj}(t)$ are the components of displacement of these nodes in the normal direction r. For the convention used, the nodes overlap if

$$\Delta u_{ij}(t) \quad < \quad 0 \tag{3.41}$$

At every time step, this relative normal displacement is determined for all the node pairs situated along the length of the crack. When overlap occurs at any of these nodal pairs, the response calculations are repeated over this time step with corrective forces applied to bring the nodes together. Letting i_n and j_n represent the n^{th} pair of the nodes where overlap occurs, say at time $t = t_1 = t_0 + \Delta t$, a first estimation of the corrective force F_n can be assumed as

$$F_n = -\Delta u_{ij}^n(t_1)[k_{ri}^n + k_{rj}^n]/2 \tag{3.42}$$

where $k^n{}_{ri}$ and $k^n{}_{rj}$ are the components of the stiffness at node pair n in the normal direction. This force is assumed to act linearly over time step Δt as shown in Figure 3.3.

In this re-calculation, the dynamic load at nodes i_n and j_n within time step Δt is given by

$$\{Q_1\} = \{F\}\left(\frac{t - t_0}{\Delta t}\right) \qquad \left(t_0 \le t \le t_1\right) \tag{3.43}$$

where $\{F\}$ is the amplitude vector of the nodal force at time t_1. Substituting load $\{Q_1\}$ into generalized equation (3.27) yields

$$\begin{aligned}\ddot{Y}_k + 2\,\xi_k\omega_k\dot{Y}_k + \omega_k^2 Y_k = \{\eta_k\}^T\{\ddot{u}^o\} + \omega_k^2\{\psi_k\}^T\{Q_s\} \\ + \sum_{n=1}^{m}\omega_k^2\,\frac{F_n(t-t_0)}{\Delta t}[\psi_{kr}(i_n) - \psi_{kr}(j_n)]\end{aligned} \tag{3.44}$$

where $\psi_{kr}(i_n)$, $\psi_{kr}(j_n)$ are components of ψ_k at nodes i_n and j_n, respectively, and m denotes the number of node pairs that are overlapped.

Integrating equation (3.44) by the Runge-Kutta method from time t_0 to t_1 provides the generalized coordinates and the corresponding displacements at time t_1. At this stage, the relative displacements of all node pairs are re-evaluated. If overlap is still detected, the nodal forces F_n are increased by an arbitrary amount and the process is repeated until the overlap is corrected or the crack is forced to become open. In the present calculations, this increase was assumed equal to one-half of the force in the preceding cycle and the convergence criterion is based on a prescribed overlap tolerance of 0.02, i.e. the ratio of the current overlap to the initial overlap before imposing corrective forces. If, however, the crack is found to be open at some node pairs under the above cyclic application of corrective forces F_n, the bisection algorithm is employed to determine the forces required to satisfy the overlap tolerance. In this algorithm, the subsequent corrective nodal forces are given by $F_n = (F_{n,o} + F_{n,c})/2$, where $F_{n,o}$ and $F_{n,c}$ are the force magnitudes corresponding to the most recent cycles at the end of which the crack was open and closed, respectively, at the nodes in question.

Although 10 to 30 corrective load cycles were usually found necessary to model crack closure for the above overlap tolerance of 0.02, the procedure proved to be very efficient nonetheless. This is due to the overall computational efficiency of the present mode superposition analysis which requires only a small number of modes to achieve good accuracy as shown later in Chapter 4.

3.3 MODELLING THE PHYSICAL PROCESS OF CRACK EXTENSION

To prevent the singularity problems associated with cracked structures due to identical coordinates of node pairs on the two surfaces of the crack, the multi-domain boundary element method is employed in this study. The latter requires the two surfaces of the crack to belong to two different subdomains. To achieve this, the domains on either side of the crack are separated by the so-called "prolonged line" which is an arbitrary boundary drawn from the crack tip to a node on the opposite side of the full boundary element model. For convenience, it is initially assumed to be horizontal.

For seismic response analysis, the expressions for the dynamic modal stress intensity factors may, by analogy to equation (2.13), be written as

$$K_{Ij} = \frac{2\mu}{(k+1)}\sqrt{\frac{\pi}{2r}}\,[\phi_{jV}(D)-\phi_{jV}(B)]$$

$$K_{IIj} = \frac{2\mu}{(k+1)}\sqrt{\frac{\pi}{2r}}\,[\phi_{jU}(D)-\phi_{jU}(B)] \tag{3.45}$$

where K_{Ij}, K_{IIj} are stress intensity factors of the j th mode related to the crack opening mechanism (type I) and the crack sliding mechanism (type II), respectively; and ϕ_{jV} (D), ϕ_{jV} (B), ϕ_{jU} (D), ϕ_{jU} (B) are amplitudes of the j th mode shape at points D and B in the V and U-directions respectively as shown in Figure 2.1(b).

The time histories of the stress intensity factors during seismic loading can be obtained by mode superposition, which yields

$$K_I(t) = \sum_{j=1}^{m} K_{Ij} Y_j(t)$$

$$K_{II}(t) = \sum_{j=1}^{m} K_{IIj} Y_j(t) \tag{3.46}$$

where m represents the number of modes considered.

The maximum tensile strain theory adopted in Chapter 2 is also employed to determine the orientation of crack development under dynamic loads. The criterion for crack extension may, by analogy to equation (2.23), be expressed as

$$K = \frac{1}{4(1-\nu)}\{K_I[(3-5\nu)\cos\frac{\theta_0}{2}+(1+\nu)\cos\frac{3\theta_0}{2}] - K_{II}[(3-5\nu)\sin\frac{\theta_0}{2}+3(1+\nu)\sin\frac{3\theta_0}{2}]\} \geq K_{Id} \tag{3.47}$$

where K_{Id} is the dynamic fracture toughness, θ_0 is determined by equation (2.20) and K is defined as the combined stress intensity factor for the mixed type crack mechanism.

At the time when the dynamic fracture toughness is found to be exceeded, the angle at which the crack propagates is determined from equation (2.20). The crack length is now extended in this direction arbitrarily by a certain fraction of the existing crack length. In this regard, the determination of the amount of crack extension is always a limitation of the discrete crack approach. Indeed, the available finite element studies of dynamic crack propagation extend the crack by moving the tip to the nearest node in the appropriate direction.

Since equation (2.20) gives only the direction of crack propagation, it is important that the crack be extended in this direction by a suitably small amount at a time in order to avoid forcing the development of the crack profile. Because extremely small increments in length are computationally inefficient, extensions of approximately 10 to 20 per cent of the existing crack length are assumed in the present study.

Once the crack has been extended in the appropriate direction, the two subdomains on either side of the crack are again separated by arbitrarily relocating the nodes of the previous prolonged line but in such a way that the revised line emanates from the new crack tip. Thus, the nodes on the revised prolonged line are neither related to the crack increment nor does the new line affect the propagation of the crack in any manner.

Following the above crack extension and remeshing, the natural frequencies and mode shapes of the cracked structure are re-calculated. Since it is assumed that no time elapses during each stage of crack extension, the generalized coordinates are assumed to remain unchanged. Thus, the response of the structure after each stage of crack extension is based on the new mode shapes and the generalized coordinates before the extension. Noting that the mode shapes do not change significantly for each stage of extension, this initial discrepancy in the displacements following crack propagation will vanish after a few integration time steps because of the damping mechanism.

3.4 VERIFICATION OF NUMERICAL MODEL BY COMPARING WITH TEST OF CANTILEVER BEAM

To enhance confidence in the foregoing procedure for examining the cracking process of concrete dam structures, the basic hypotheses underlying the formulation need to be verified by experimental data. This involves primarily the impact simulation of crack closing and the maximum tensile strain criterion for crack extension. For this purpose, numerical predictions are compared with experimental data of a cantilever beam model made of gypsum tested at Tsinghua University on a shaking table subjected to dynamic excitation. Test data and numerical results obtained by impulse method were generated for three conditions of the model structure: (1) uncracked; (2) initially cracked without extension; and (3) initially cracked leading to rupture. To simulate the initially cracked condition, a 50 mm long cut was made in the beam model using a steel blade.

Details of tests

Figure 3.4 shows the experimental set-up which had a force capacity of 4.90 kN and a frequency range of 5-2000 Hz. The size of the gypsum beam was 800 x 200 x 100 mm with the following material properties: specific gravity = 7.65 kN/m^3; dynamic modulus of elasticity $E_d = 1.77 \times 10^3$ MPa (converted from frequency tests); damping ratio = 0.02; and Poisson's ratio = 0.2.

Two accelerometers were employed, one located on the table and the other at the top of the model. Strain gauges were located at 5 and 12 mm in front of the crack tip on both sides of the beam to measure the stress intensity factor and to monitor extension of the crack. With strain measured in the y-direction, the stress intensity factor K_I (opening type mechanism) was evaluated employing the expression

$$K_I = E \varepsilon_y \sqrt{2\pi r} \qquad (3.48)$$

where r represents the distance between the crack tip and the strain gauge.

Accuracy

The above locations of the strain gauges were based on the following considerations of accuracy. Equation (3.48) is the first-term expansion of a complete series in which the truncation error depends on the finite distance between the crack tip and the measuring point. According to the accuracy study of intensity factor around the crack tip reported in Reference [52], the error is of the order of 6.5 per cent if the distance r is chosen to be 1/10 of the crack length. Thus the first gauge, located at this distance, should theoretically give realistic results although other factors, such as the average strain over the gauge length rather than that at a point, lead to experimental measurements of K_I which should be viewed as approximations only.

Comparison of numerical results and test data

The BE discretization of the beam used to obtain the numerical results is shown in Figure 3.5. Table 3.1 compares the measured and computed frequencies for the first six modes of vibration for both the initially cracked and uncracked states of the beam. Very good agreement (within 10 per cent) is observed for the first four modes, while the discrepancy between the test and numerical results is approximately 30 per cent for the fifth and sixth modes. It is worth noting that the frequency decrease due to the existence of the initial 50 mm crack is not significant, except for the first mode where frequency decreases by approximately 11 per cent. The corresponding measured frequency response curves are presented in Figure 3.6.

Figure 3.7 shows the results of the initially cracked beam for harmonic excitation at frequency f = 10 Hz. Shown are the acceleration time histories of the shaking table and top of the model, as well as of the stress intensity factor K_I. The BE numerical results are also plotted in these figures. It is evident that the beam vibrated essentially as a rigid body; thus, the amplification effects were not significant since the excitation frequency was much lower than even the fundamental frequency $f_1 = 64.7$ Hz of the beam. The accelerations at the top of the beam obtained in the test are very close to the BE numerical results, while the measured values of stress intensity factor K_I are somewhat smaller than those computed. Nevertheless, there is still good correlation between the numerical and experimental values.

The capacity of the shaking table was not sufficient to conduct a harmonic crack extension test to rupture, but the latter was nevertheless attempted by gradually increasing the initially harmonic force of the table in stages. Due to this mechanical limitation of the equipment, the table acceleration curve became distorted from harmonic as seen in Figure 3.8(a). From Figure 3.8(b), it is interesting to note that this distorted acceleration input excited response of the model structure primarily at two frequencies, namely the fundamental frequency of 64.7 Hz as well as the forcing frequency ($f = 7$ Hz) itself. The associated resonant effect resulted in an amplification factor of more than 2.0 at the top of the model, causing the crack to extend to the rupture phase. In Figures 3.8(b) and 3.8(c) one can clearly see that the crack began to propagate at time $t = 0.96$ sec following a series of strong response cycles. The dynamic fracture toughness of the gypsum material K_{Id} is approximately 41 kPa·$m^{1/2}$ as evident in Figure 3.8(c).

Whereas the extension of the crack in the beam for the BE calculation took place over a number of cycles of vibration, in the experiment the propagation of the crack was too rapid to be observed. However, in both cases the crack breaks through when the beam is deflected to the left, namely when the crack is open. In this position, the left edge is in compression and it is the shear acting on the small connecting portion that accounts for final breakthrough in the experiment. In the present analysis, on the other hand, this final phase is not modelled. Rather, breakthrough is assumed if, after extending the crack, it is found that the distance between the new crack tip and the edge of the structure is smaller than needed to accommodate new boundary elements. The compression and sliding in the remaining phase could be handled by the BEM but is beyond the scope of the present analysis. Thus, the formulation is limited to behaviour of the cracked structure up to, but not including, final penetration. Behaviour following rupture also involves sliding and is similarly not modelled herein.

Figure 3.9 shows the time history of combined stress intensity factor K for the rupture test table excitation of Figure 3.8(a). It is worth noting that the initial crack was predicted to extend once the computed value of K first reached the critical magnitude of 41 kPa·m$^{1/2}$ at t = 0.27 sec (see also Table 3.3), whereas in the test the crack began to propagate only at t = 0.96 sec as previously noted. This departure from expected behaviour is probably attributable to weakening of the gypsum material due to the effect of cyclic fatigue, with the actual (initial) fracture toughness at t = 0.27 sec being higher than its value at the time of failure.

Table 3.2 lists the natural frequencies of the model for the different stages of crack development. It is seen that the first mode frequency decreases significantly as the crack extends; however, crack extension has progressively smaller relative effect on the frequencies of the higher modes. Table 3.3 documents the computed development of the crack in terms of orientation, tip coordinates and stress intensity factors.

Finally, Figure 3.10 shows the profile when the crack has finally penetrated through the model. Here also, very close agreement is observed between the numerical predictions and test results.

The numerical results in this section are obtained by impulse method for which the formulation is based on use of a hypothetical structure to model the behaviour of the actual cracked system. In this idealization, impulses act at the nodes along the closed portion of the crack to simulate the effect of change in stiffness due to crack closure, but overlap of the crack surfaces is not prevented. To confirm that this hypothetical violation of the physical situation is not an actual limitation of the proposed method, comparison has been made with force method for modelling crack closure. Figure 3.11 shows that both the impulse method and the force method predict identical crack profiles for the rupture test of the cantilever beam model structure.

More detailed comparison between the two methods for crack closure is presented in Section 3.5 and Chapter 4.

3.5 CORRELATION ANALYSIS WITH MODEL TEST OF KOYNA DAM

The objectives of this correlation analysis are: (1) to provide, in addition to the preceding comparison with the cantilever beam test data, further verification of the accuracy of the proposed numerical procedure for seismic fracture analysis; and (2) to obtain a qualitative evaluation of the cracking process of the Koyna dam under simplified loading conditions. The model scale of the Koyna dam section is 1:200; namely 515 mm in height, 351 mm wide at the base and 80 mm thick. The specific gravity γ of the gypsum material is 4.71 kN/m^3 and the dynamic modulus of elasticity $E = 600$ MPa.

Accelerometers were installed on the table and at the crest of the model and strain gauges were located on both sides of the model at 5 and 12 mm from the crack tip. Thus, with strain ε_y measured in the y-direction the stress intensity factor K_I was determined from equation (3.48).

As shown in Figure 3.12, the model was fixed to the shaking table, with no reservoir water included. Harmonic sweeping tests were first conducted to obtain the frequency components of the model. To cause the dam model to rupture, a lead block weighing 27.1 N was attached at the crest. An initial crack 10 mm in length was cut at the location of slope change on the downstream face. Because of the capacity limitation of the shaking table, the input excitation for the rupture test comprised a series of load pulses which was approximately periodic but not harmonic.

For the numerical predictions, two per cent damping ($\xi = 0.02$) was assumed for the six modes considered and the Poisson's ratio ν was assumed equal to 0.2. As shown in

Figure 3.13, the test model was divided into three BE subregions. The lead block having an elastic modulus E = 1.0×10^5 MPa and specific gravity $\gamma = 75.3$ kN/m^3 was also represented by a subregion. The initial crack and its arbitrarily prolonged line form a horizontal interface between dam subregions II and III. This interface will change shape as the crack progresses stage-wise in orientation and length. Fifty nine quadratic elements were employed in the discretization of the model assuming the condition of a rigid foundation to simulate the shaking table. An unequal distribution of elements, with a much denser mesh near the crack tip and also at the slope change location on the downstream face, was employed in order to refine the calculation of stress intensity factors and to permit ease of remeshing the crack surfaces following crack extension.

The process of crack extension was divided into 8 stages, each of which extended the crack length by a predetermined amount. In each stage of constant crack length, the first six frequencies and mode shapes were obtained and step-by-step time integration was employed to obtain the structural response and the stress intensity factors at the crack tip. Time step $\Delta t = 0.001$ sec was used in the calculation. Once the combined stress intensity factor exceeds the dynamic fracture toughness $K_{Id} = 11.0$ kPa·m$^{1/2}$, crack propagation occurs perpendicular to the maximum circumferential strain direction with infinite velocity. The foregoing value of K_{Id} is obtained directly from the test measurements shown in Figure 3.14(b), where sudden rupture of the model is seen to occur at time 0.728 sec. It should be noted that different kinds of plaster were used in the tests of the previous cantilever beam of Section 3.4 and the current model dam, resulting in very different values of K_{Id} as well as modulus E (600 MPa for the model dam and 1770 MPa for the beam). It was assumed that the crack length extends by 10-20 per cent and the structural frequencies and related stress intensity factors were re-evaluated for each new stage of crack length. This procedure was repeated until either the crack reached the opposite face of the model or the excitation stopped.

For the initially cracked model, the measured and calculated frequencies are listed in

Table 3.4. The results from the test and calculation are seen to be close. For the rupture test the table excitation frequency was 6.1 Hz, with the input acceleration exceeding the table capacity and causing a distortion of the intended harmonic motion as evident in Figure 3.14(a). The time histories of the measured and calculated (force method and assuming no crack extension) crack tip stress intensity factor K_I are compared in Figure 3.14(b). It is noted that the BE results and the test measurements are in good agreement in general. Figure 3.14(b) also shows that rupture of the model dam occurred at t = 0.728 sec, when the strain gauges suddenly broke during the test.

A comparison of the time histories of stress intensity factors for the impulse and force methods for crack closure modelling is shown in Figure 3.15, assuming no extension of the initial crack before time t = 0.728 sec. Figure 3.15(a) demonstrates that K_I shows very similar patterns for both methods , thus indicating that the crack closure modelling does not have much influence on the crack opening behaviour. However, Figure 3.15(b) shows that K_{II} exhibits a significant dependence on the modelling of the closure mechanism. Whereas a vivid oscillation is observed for the impulse model, the force approach yields similar negative values but with all the positive peaks cut out. The explanation for this is that the former allows an additional positive tangential deformation (toward downstream) to occur due to the hypothetical overlap, thus causing positive peaks in K_{II}. Since the combined stress intensity factor K is influenced mainly by K_I, it is to be expected that the time histories of K are similar for the two methods as evident in Figure 3.15(c).

Figure 3.16 shows the results from crack extension analysis in terms of the time histories of stress intensity factors up to t = 0.260 sec. At this time the first major peak in the excitation occurred, causing rupture at this instant rather than at t = 0.728 sec as observed in the test. The probable explanation for the time discrepancy is the effect of cyclic fatigue. It is postulated that the gypsum material actually possessed a higher initial fracture toughness which was subsequently reduced under the effect of load reversals until rupture finally occurred when the shaking table experienced another major acceleration peak at t = 0.728 sec. A detailed comparison of stress intensity factors for both the impulse and force methods during the extension process is shown in Table 3.5. The results indicate very good agreement between the two models for crack closure. They also confirm that K_I plays a dominant role in the process of crack extension because the magnitudes of the combined stress intensity factor are close to those of K_I. It is interesting to note that the crack of the model dam propagates much faster than that of the previous cantilever beam. This is probably due to the heavy lead block attached at the model's crest, resulting in large amplifying inertial force during the rupture process and causing the crack to break through during one peak in the excitation.

Figure 3.17 shows the crack profiles at rupture observed in the test and those obtained by both the impulse and force methods. The agreement between the three is outstanding, thereby confirming that the two models for closure simulation are applicable to practical problems.

3.6 CONCLUDING REMARKS

The BE numerical procedure for 2-D seismic cracking analysis has been formulated employing a stage by stage crack development. Since the process of crack closure is simulated by impulse and force rather than change in stiffness, the mode superposition is still in effect within each stage of crack growth, resulting in a linear solution to the otherwise complex nonlinear problem. The accuracy of the proposed procedure is verified by comparing numerical predictions with data from rupture tests of a cantilever beam and a model of Koyna gravity dam. The excellent agreement between the numerical predictions and the experimental measurements confirms that the 2-D dynamic procedure for fracture analysis is valid for application to practical problems.

In the following Chapter, this BE procedure is applied to a detailed evaluation of the seismic crack propagation for the Koyna prototype gravity dam. The cracking process of the dam under the 1967 earthquake is studied by both impulse and force methods for the crack closure mechanism. The computed results are compared with data from both the model test of Koyna dam and reported field observations to further confirm the engineering application of the proposed 2-D seismic fracture analysis procedure.

Table 3.1 Initial frequencies (Hz)

Modal frequency		f_1	f_2	f_3	f_4	f_5	f_6
Without crack	Measured	73.1	397.7	433.8	958.7	1074	1178
	Calculated	72.2	372.1	467.9	875.8	1424	1488
With crack	Measured	64.7	388.5	430.7	936.9	1058	1155
	Calculated	60.6	363.4	442.6	892.0	1373	1472

Table 3.2 Computed frequencies (Hz) at different stages of cracking

Stage	f_1	f_2	f_3	f_4	f_5	f_6
1	60.6	363.4	442.6	892.0	1373	1472
2	56.6	360.2	435.0	885.7	1339	1464
3	51.7	354.2	424.3	883.1	1309	1467
4	45.6	345.3	411.4	875.4	1270	1467
5	38.1	332.2	394.5	861.6	1235	1458
6	29.7	313.9	373.3	828.9	1189	1428
7	21.4	291.9	349.1	790.1	1176	1340

Table 3.3 Computed crack orientation, tip coordinates and stress intensity factors at different stages of cracking

Stage	t (sec)	Tip-x (mm)	Tip-y (mm)	θ (deg.)	K_I (kPa $m^{1/2}$)	K_{II} (kPa $m^{1/2}$)	K (kPa $m^{1/2}$)
1	0.271	150.0	100.0	185.34	42.1	2.0	42.3
2	0.396	140.0	99.1	185.50	44.4	0.1	44.4
3	0.396	128.1	97.9	186.23	42.8	0.3	42.8
4	0.675	113.8	96.4	186.42	44.1	0.1	44.1
5	0.807	96.6	94.4	187.20	49.9	0.3	49.9
6	0.807	76.7	91.9	187.82	57.8	0.3	57.8
7	0.807	57.0	89.2	189.00	62.6	0.6	62.6
8	0.807	37.2	86.1	Rupture			

Note: θ denotes the orientation of crack extension from the positive x-direction.

Table 3.4 Frequencies (Hz) of cracked dam model

Modal frequency	f_1	f_2	f_3	f_4	f_5	f_6
Measured	51.2	252.3	366.4	604.2	1119	1233
Calculated	51.1	273.9	375.9	670.2	1127	1187

Table 3.5 Comparison of stress intensity factors for model dam at different stages of cracking computed by force and impulse methods

Stage	t (sec)		K_I (kPa $m^{1/2}$)		K_{II} (kPa $m^{1/2}$)		K_E (kPa $m^{1/2}$)	
	Force	Impact	Force	Impact	Force	Impact	Force	Impact
1	0.256	0.256	10.69	10.66	-2.07	-2.05	11.44	11.40
2	0.256	0.256	12.10	12.09	0.04	0.02	12.10	12.09
3	0.256	0.256	12.94	12.86	0.04	0.10	12.94	12.86
4	0.256	0.256	13.66	13.64	0.08	0.02	13.66	13.64
5	0.256	0.256	14.04	14.02	0.11	0.11	14.04	14.02
6	0.256	0.256	13.65	13.65	0.25	0.18	13.66	13.65
7	0.256	0.256	12.49	12.38	0.25	0.31	12.50	12.40
8	0.260	0.260	14.76	11.00	0.00	-0.40	14.76	11.03

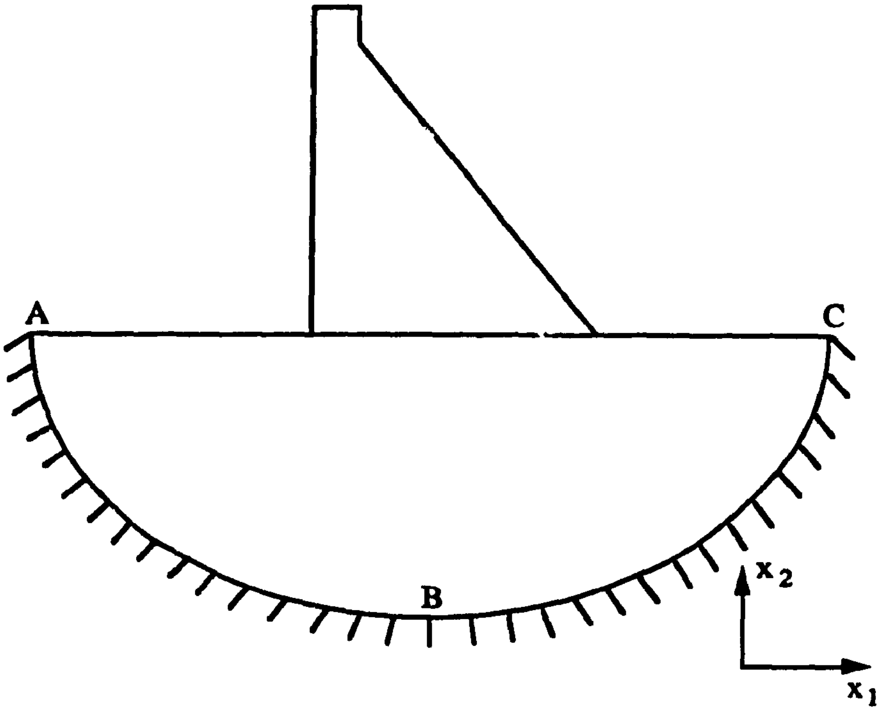

Figure 3.1 Seismic input boundary

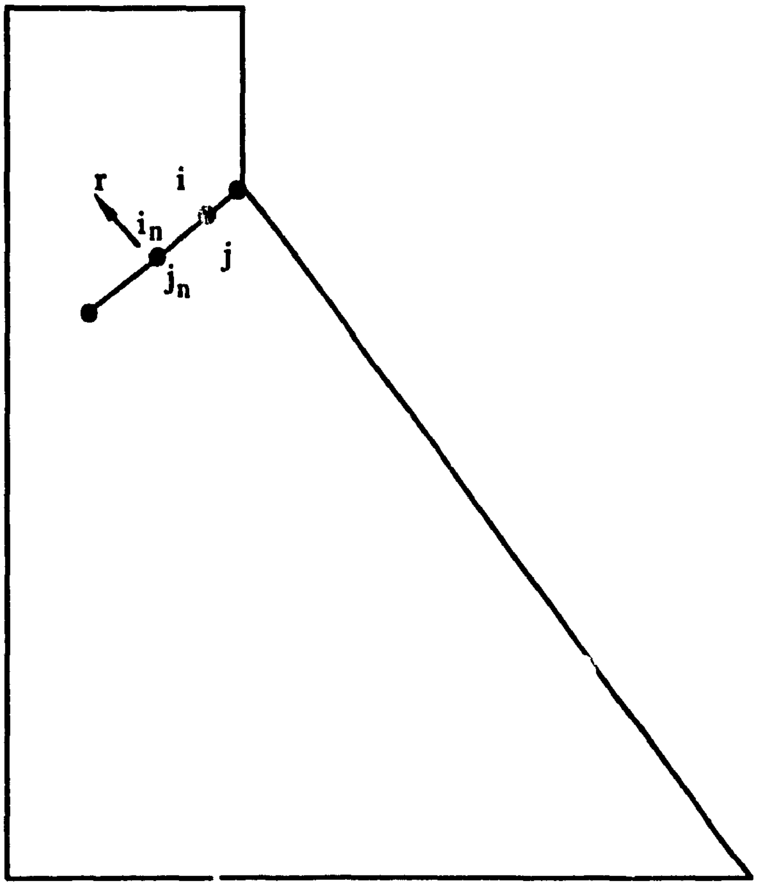

Figure 3.2 Cracked dam structure

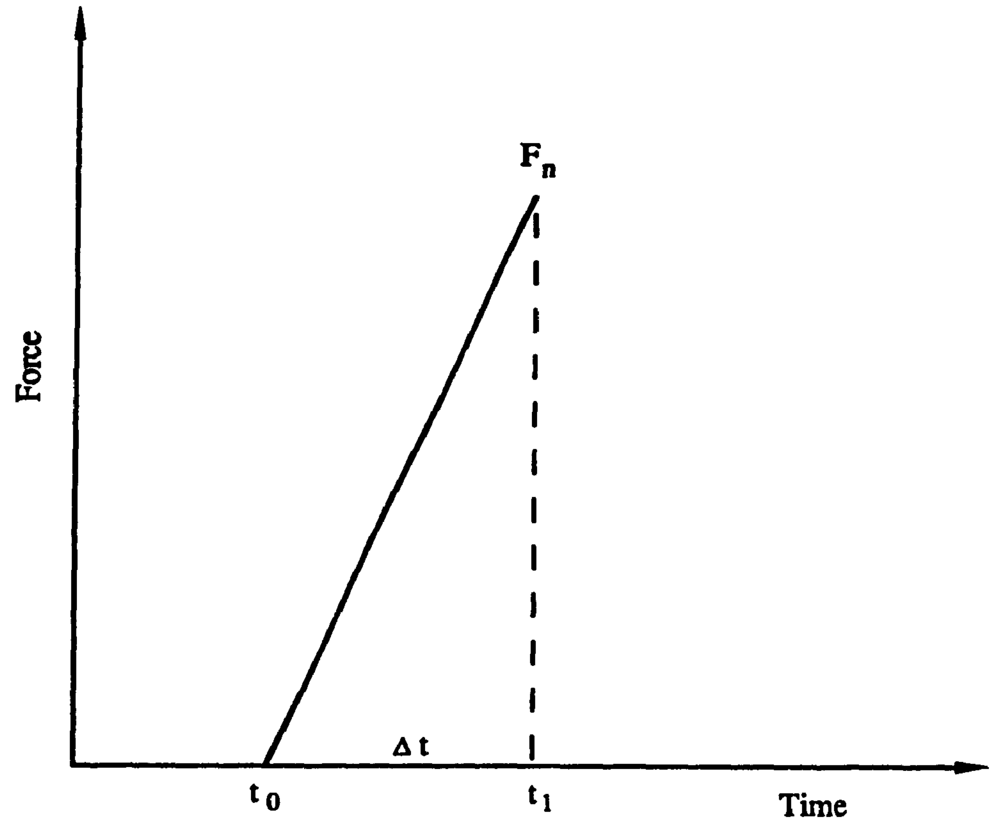

Figure 3.3 Force applied at overlapped node pair n

Figure 3.4 Shaking table and cantilever beam model structure

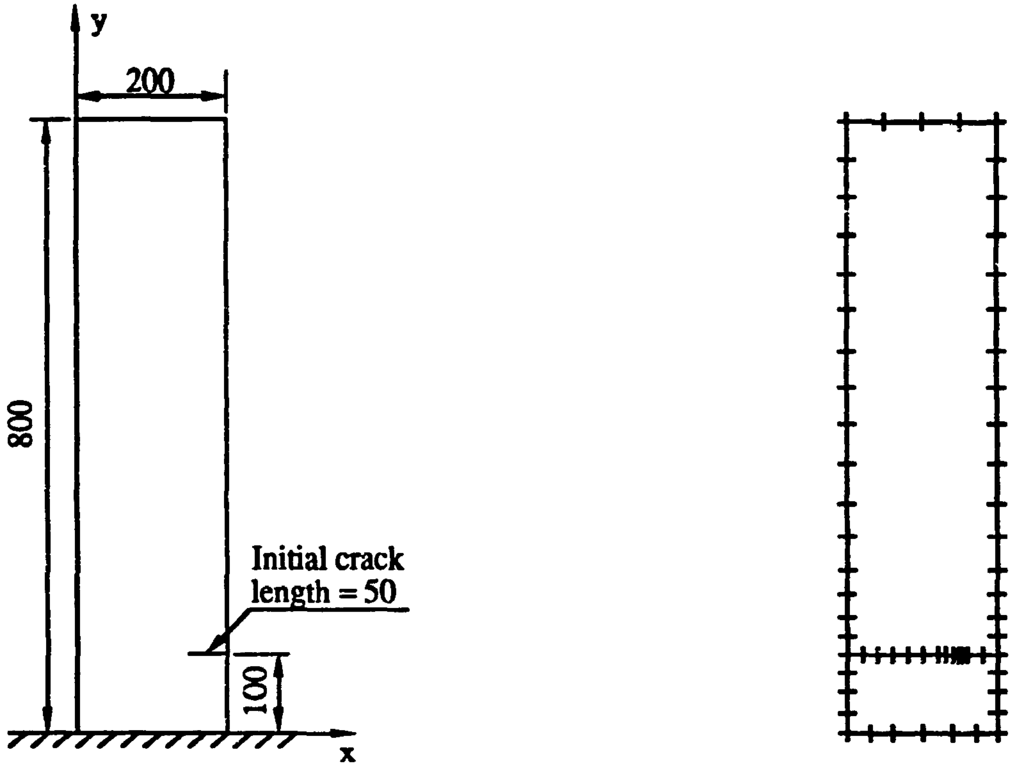

(a) Dimension in mm

(b) BE discretization

Figure 3.5 Cantilever beam model

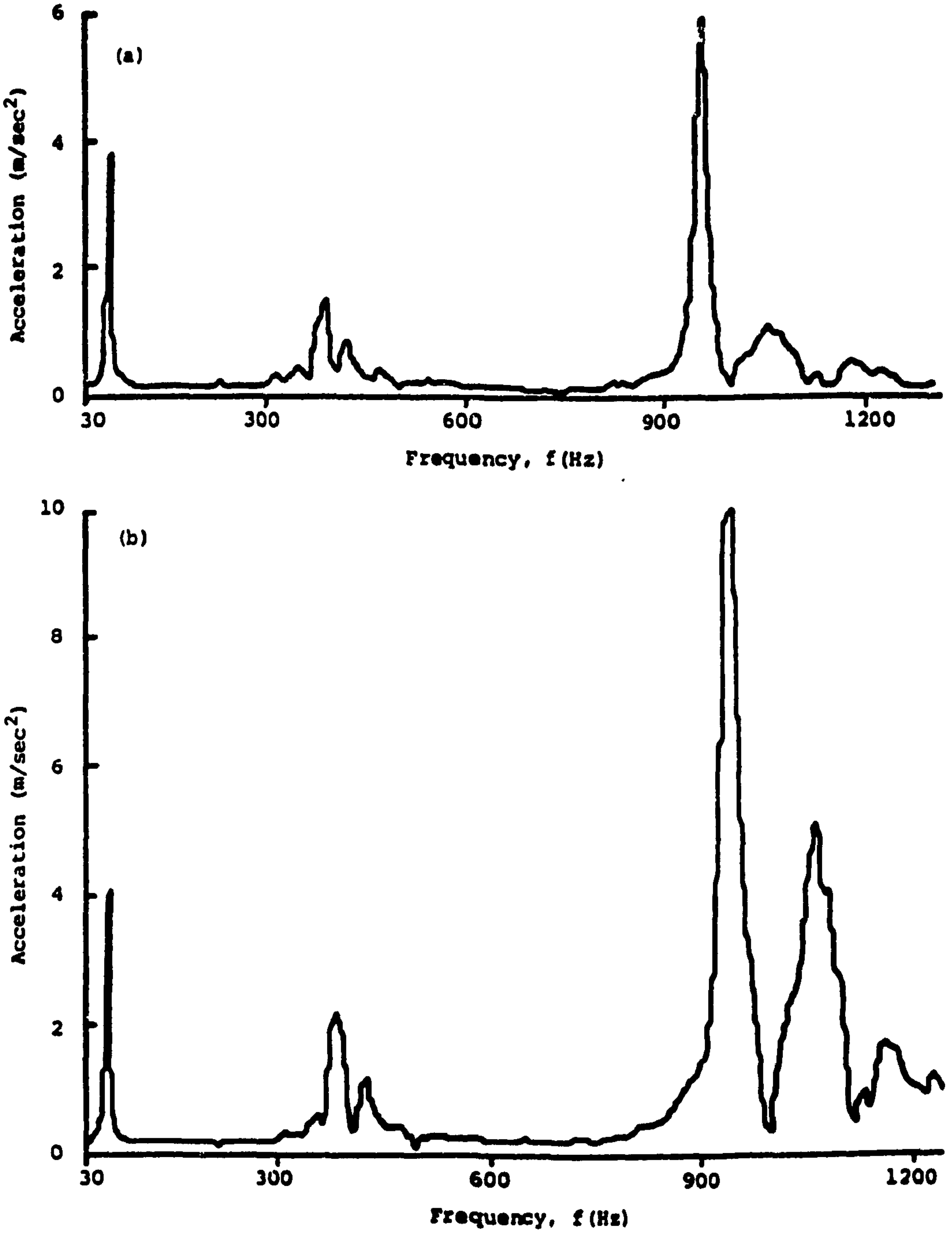

Figure 3.6 Test frequency response of model: (a) uncracked; (b) with initial crack

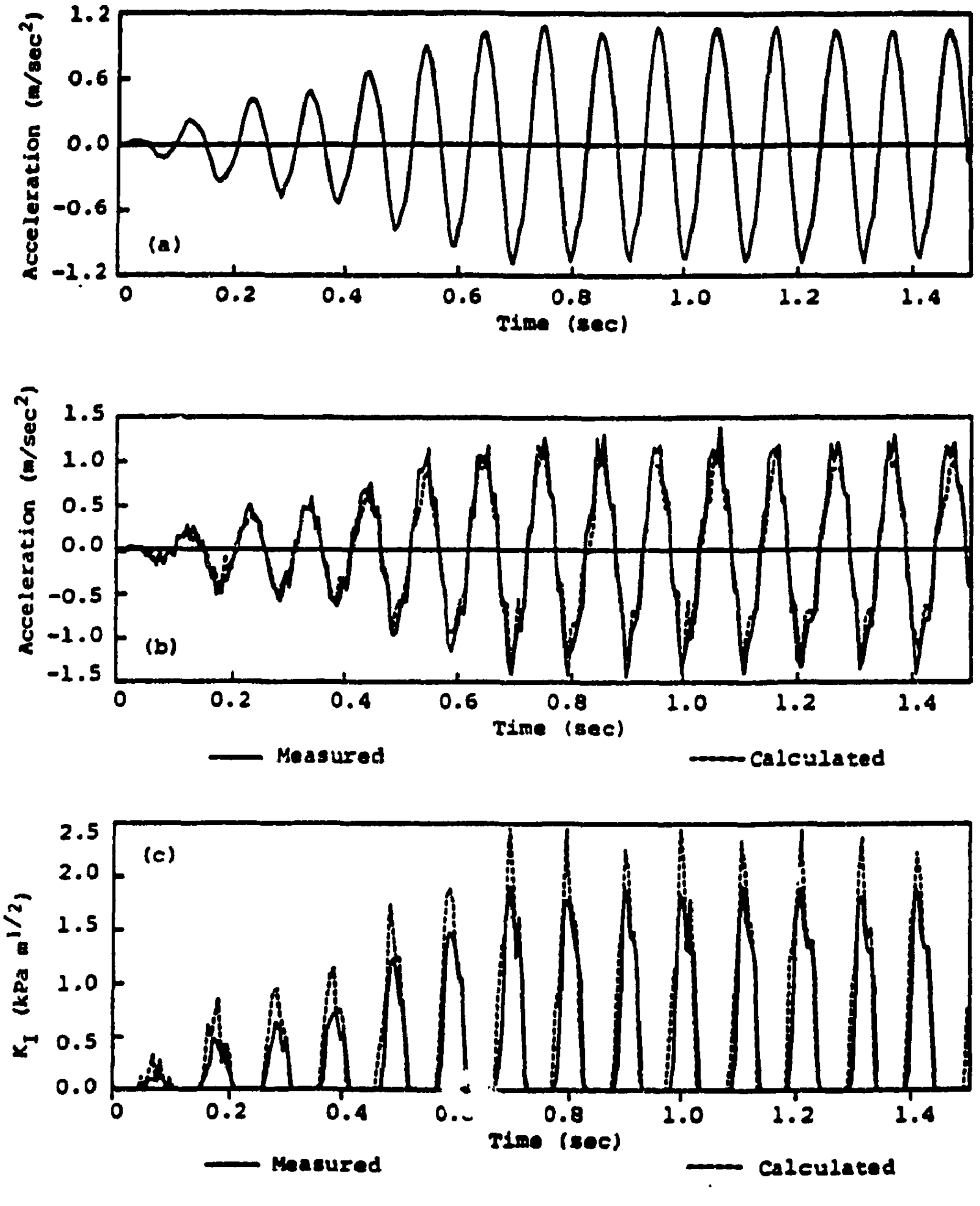

Figure 3.7 Harmonic test time histories for cracked model: (a) input motion of shaking table; (b) top acceleration; (c) stress intensity factor K_I

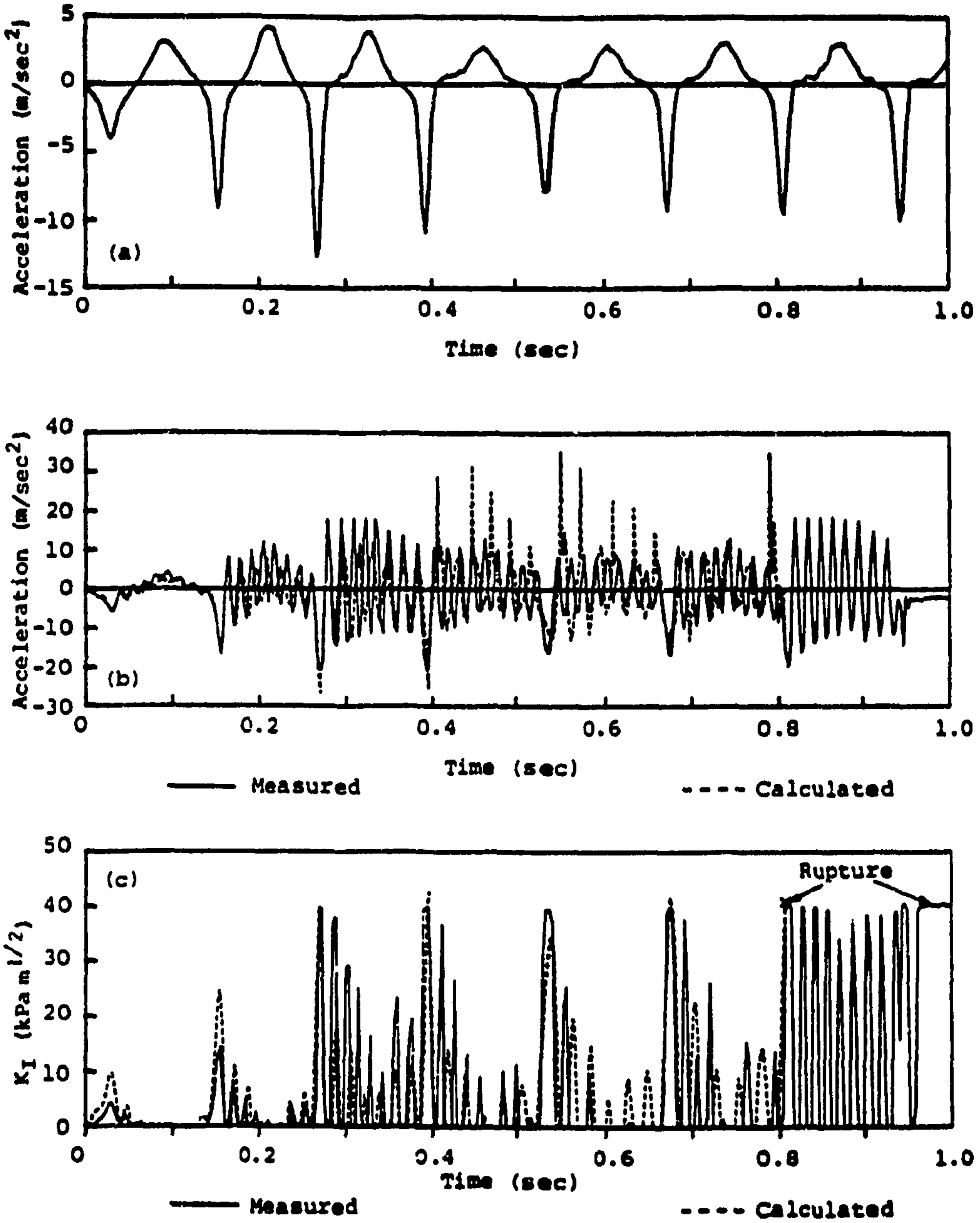

Figure 3.8 Rupture test time histories for cracked model: (a) input motion of shaking table; (b) top acceleration; (c) stress intensity factor K_I

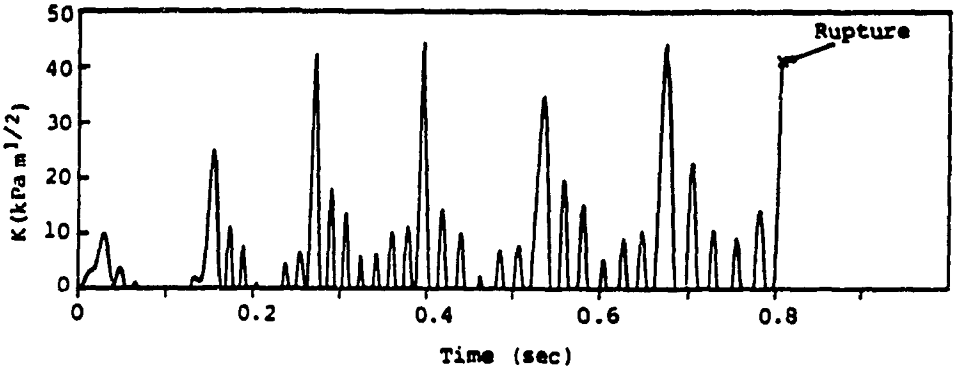

Figure 3.9 Computed combined stress intensity factor K for cracked model -- rupture test excitation

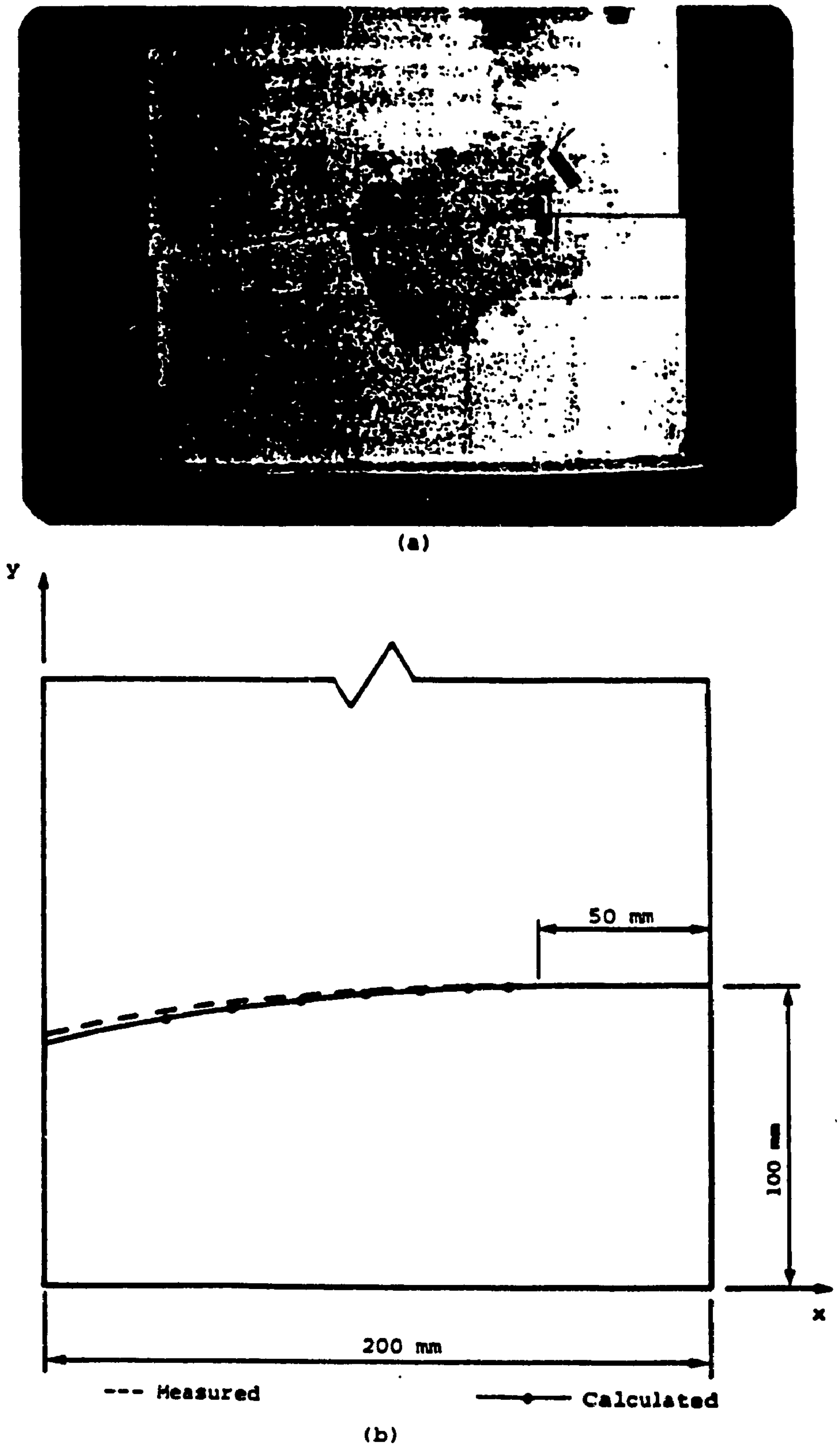

Figure 3.10 Crack profile after rupture: (a) test; (b) comparison of test and numerical results

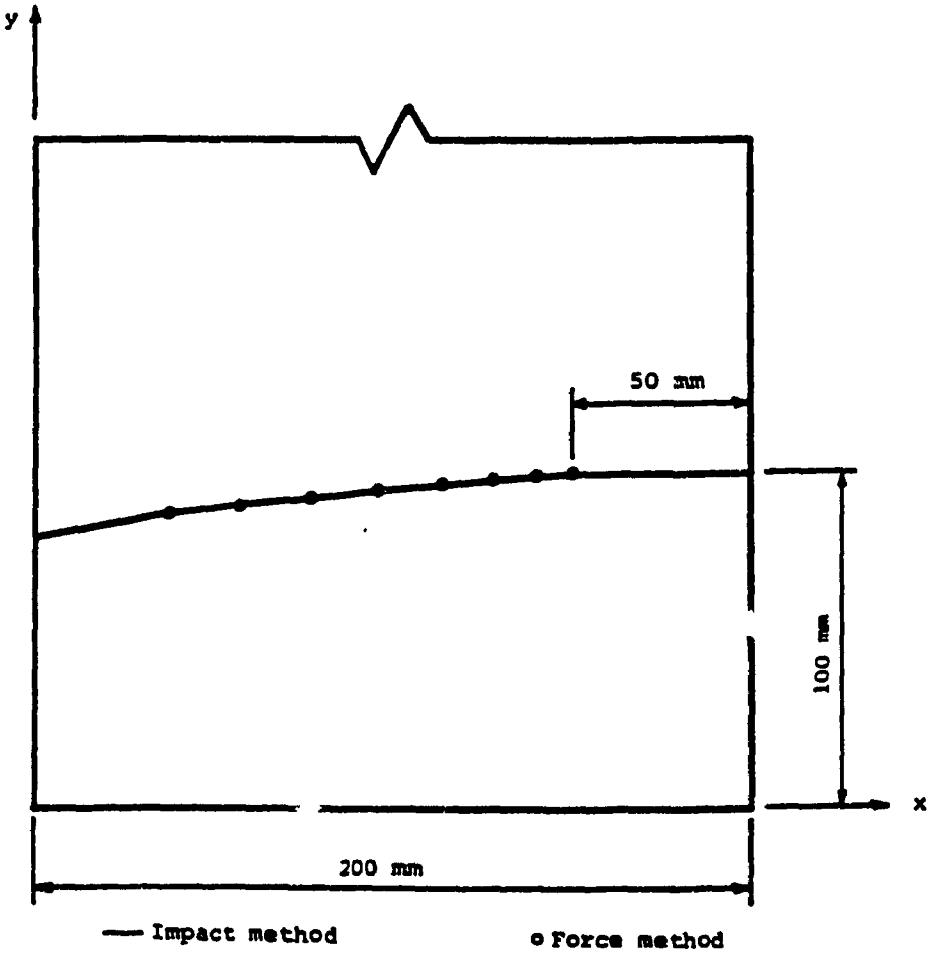

Figure 3.11 Crack profiles for impulse and force methods to simulate crack closure

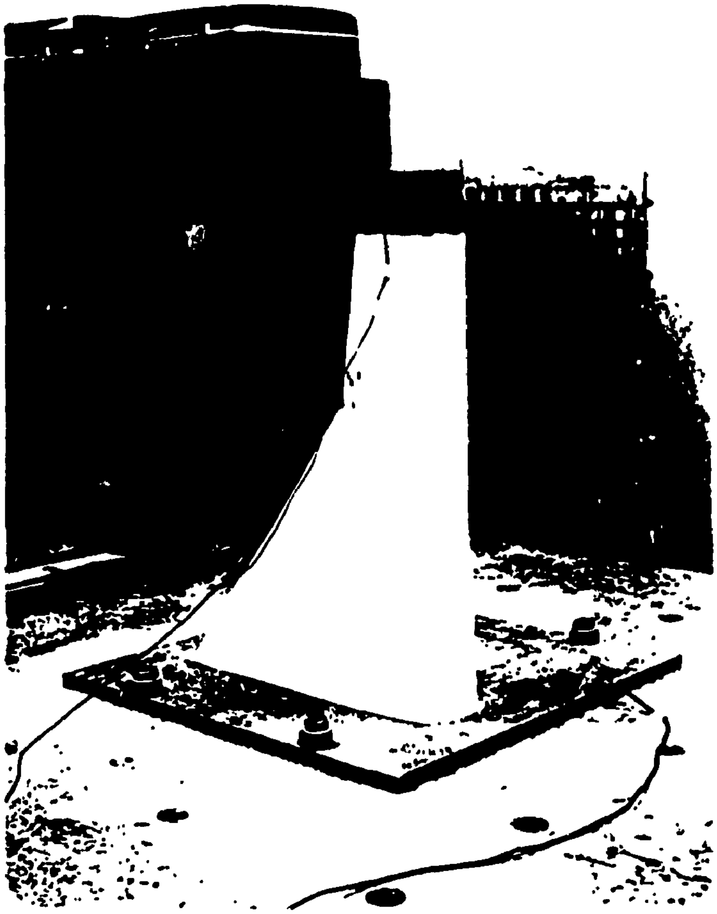

Figure 3.12 Koyna dam model with lead block on crest

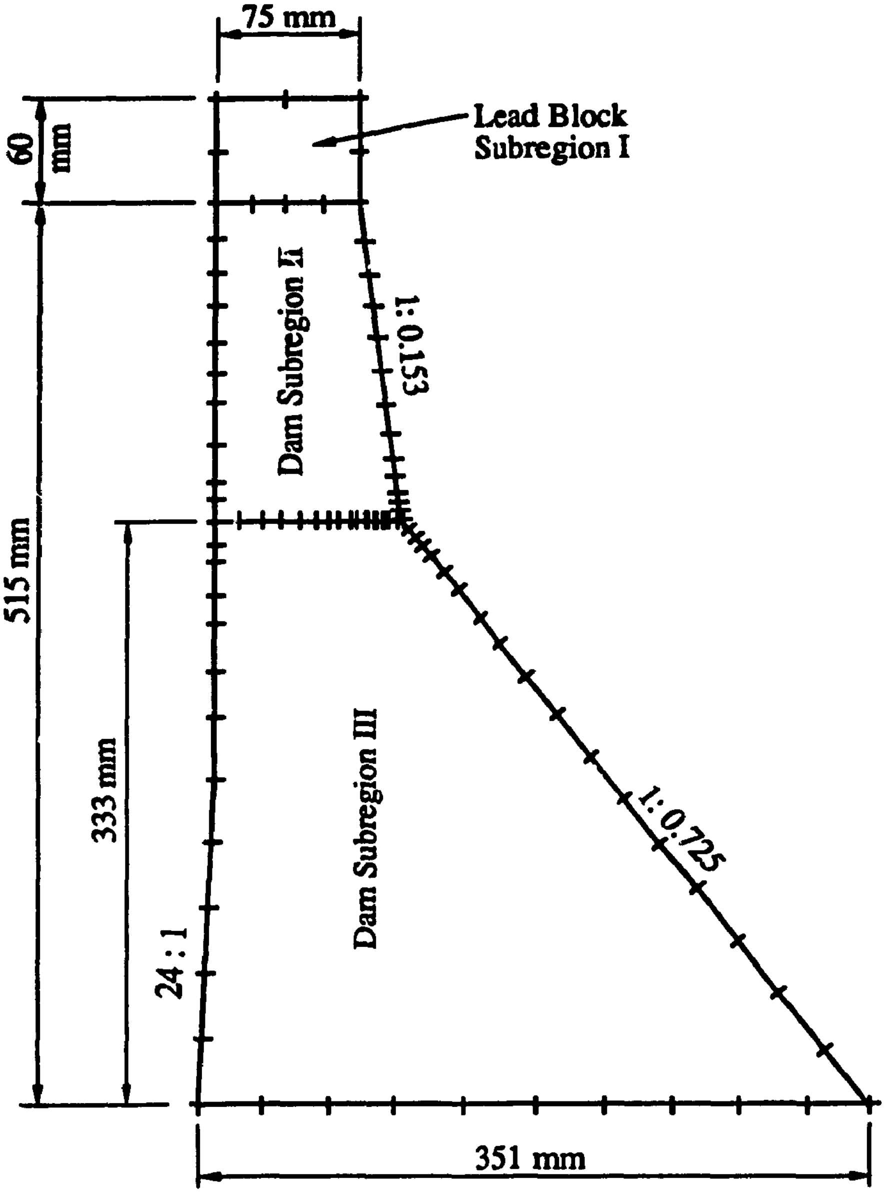

Figure 3.13 BE discretization of model dam

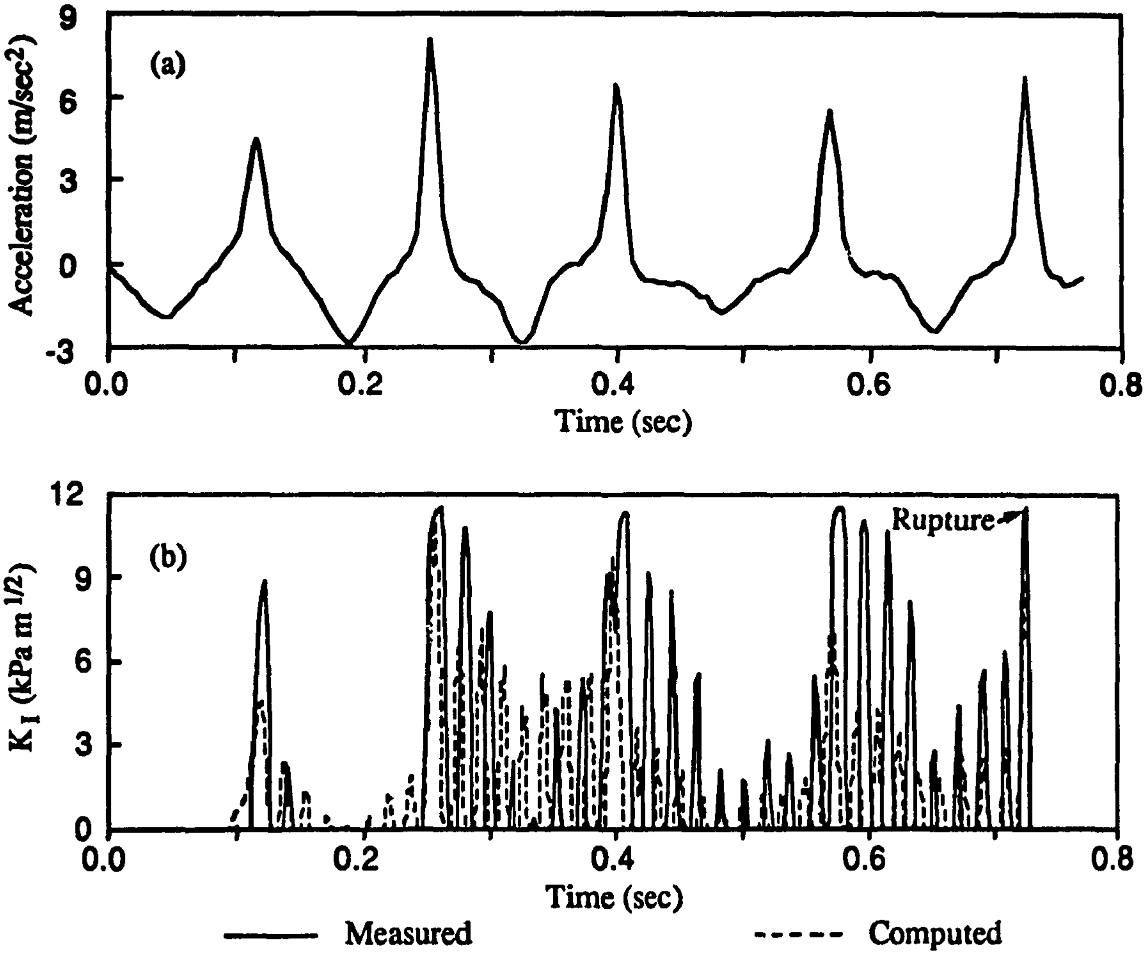

Figure 3.14 Rupture test time histories for model dam: (a) input motion of shaking table; (b) measured and computed stress intensity factor K_I

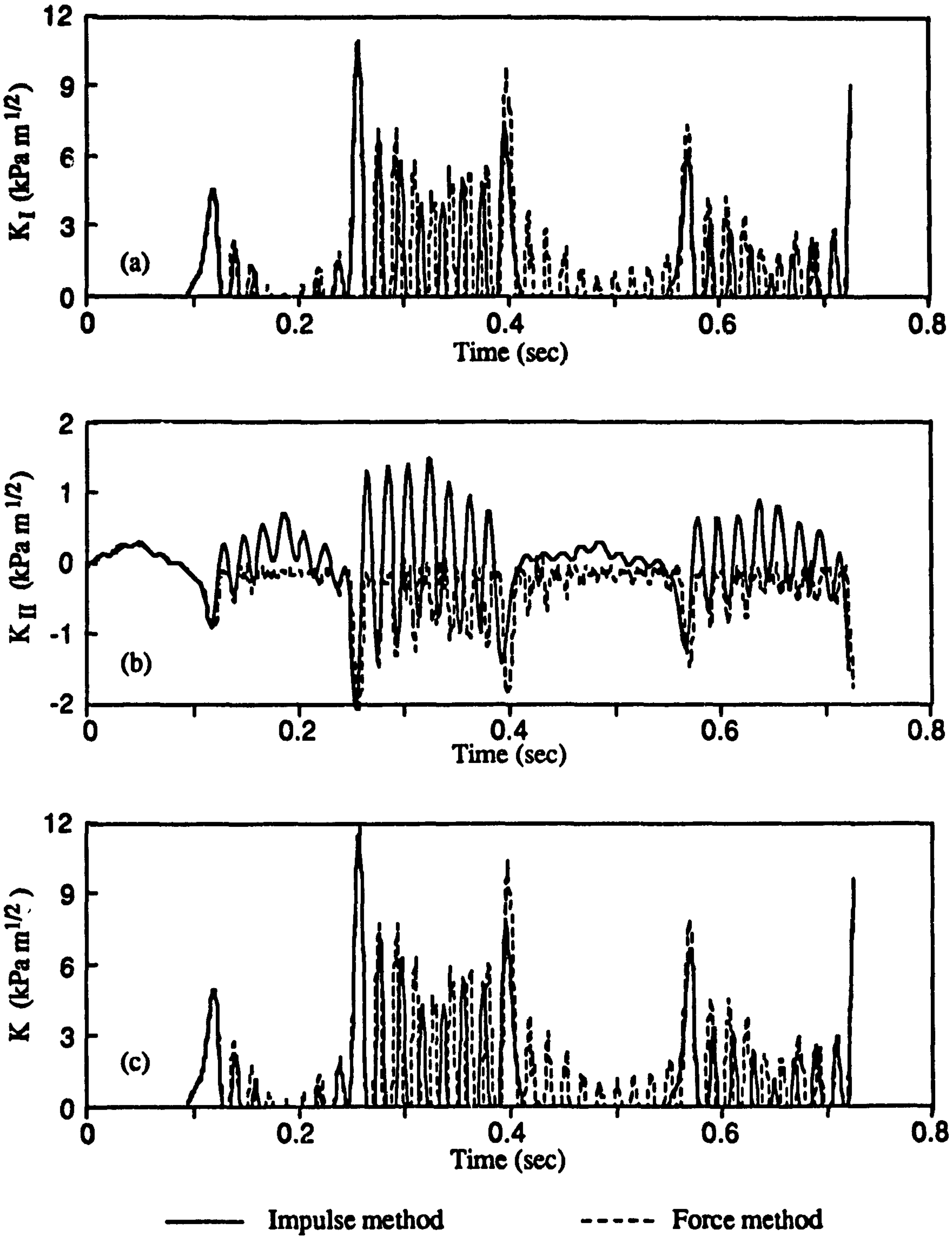

Figure 3.15 Time histories of stress intensity factors for model dam without crack extension computed by impulse and force crack closure methods

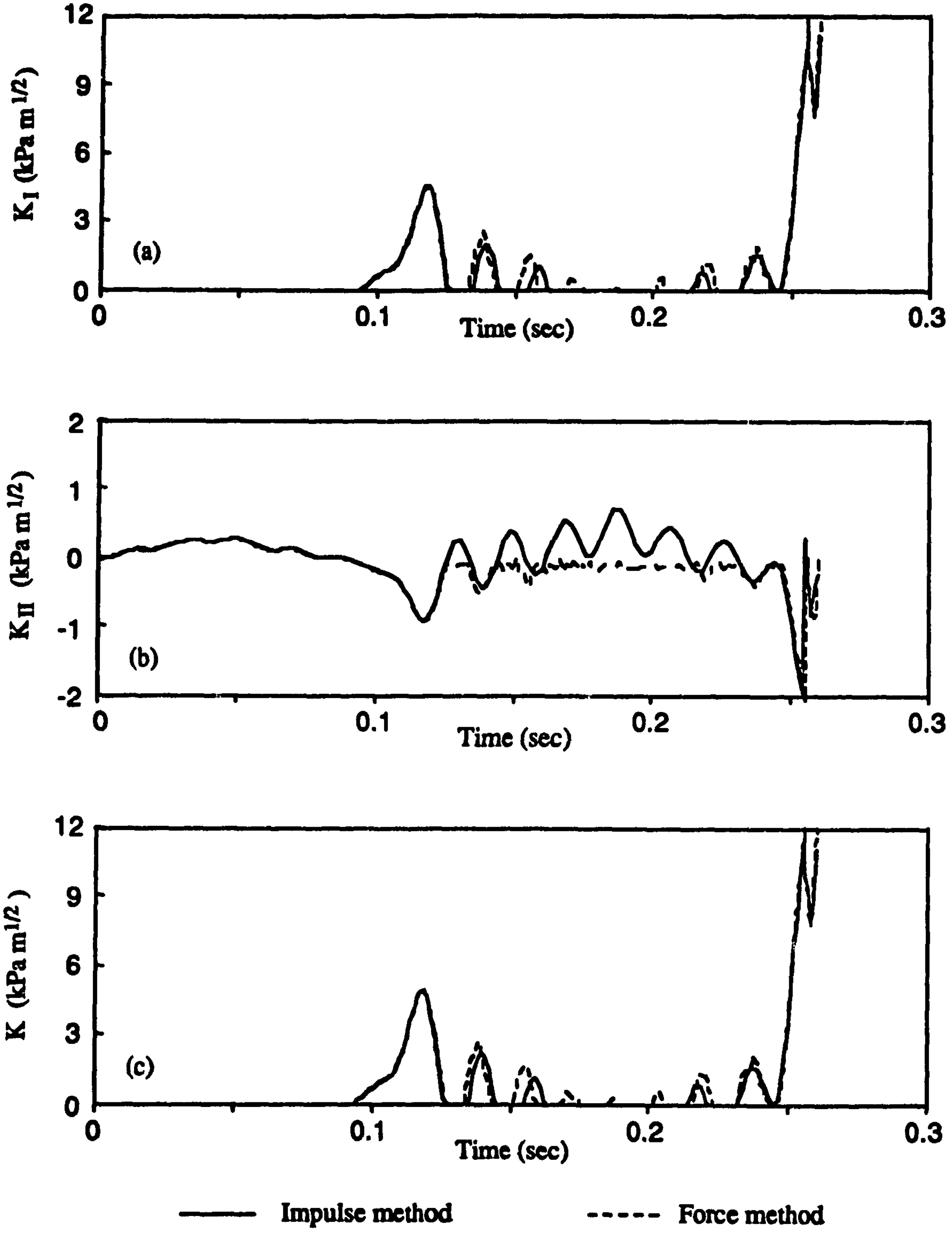

Figure 3.16 Rupture test time histories of stress intensity factors for model dam computed by impulse and force crack closure methods

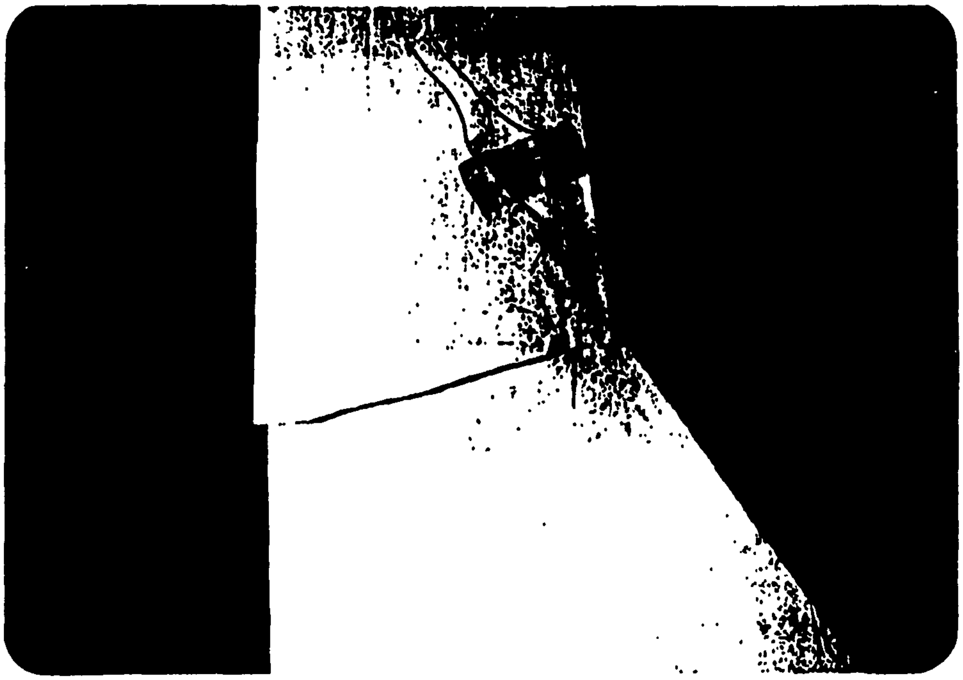

(a) Test

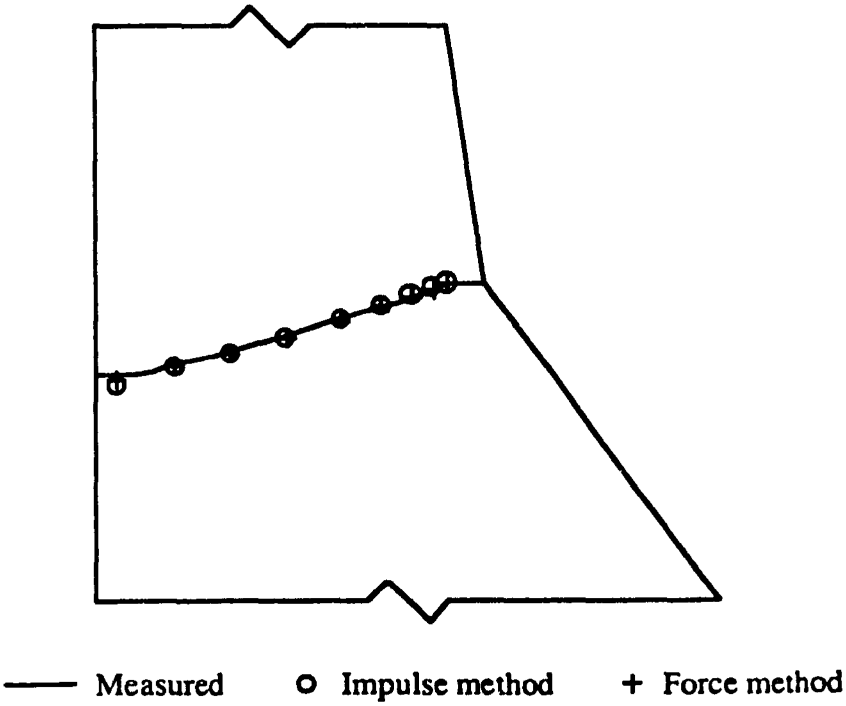

(b) Comparison of test and computed profiles

Figure 3.17 Rupture profile for model dam

CHAPTER 4

CASE STUDY - 2-D FRACTURE ANALYSIS OF KOYNA GRAVITY DAM UNDER 1967 EARTHQUAKE

4.1 KOYNA EARTHQUAKE AND DAMAGE TO KOYNA DAM

The Koyna dam is a 103 m high gravity structure located on the Koyna River in the western part of the Indian peninsula. The dam started impounding water in 1962 and experienced a magnitude 6.5 earthquake, probably reservoir induced, on December 11, 1967[53] when the reservoir elevation was only 11 m below the dam crest. The accelerations of the ground at the site were: 0.49 g in the stream direction, 0.63 g in the cross-stream direction and 0.34 g in the vertical direction. The most important structural damage consisted of horizontal cracking on both the upstream and downstream faces of a number of the non-overflow monoliths as shown in Figure 4.1. Substantial water leakage was observed on the downstream face of monolith 26 near elevation 66.5 m and traces of water seepage were detected on monoliths 18, 19, 28, 29, and 31. Soon after the earthquake, the major cracks were sealed by epoxy resin and the taller non-overflow monoliths were reinforced along the height from the top of the dam down to elevation 45.0 m which is 21.5 m below the major cracks[12].

In spite of the limited field measurements of the pattern of cracking, the Koyna dam experience has provided the most complete information to-date on seismic cracking damage of concrete gravity dams. Since the cracking of the Koyna dam occurred in the upper part of the dam, near the point of slope change where high stress concentration is to be found, initial cracking would be expected to occur at this location even during the early stages of the ground shaking during the 1967 earthquake. Once the initial crack has formed, it is evident that fracture mechanics theory should be employed to evaluate the crack propagation process and the resulting pattern of cracking.

Based on the above considerations, the cracking process of the Koyna prototype dam during the 1967 earthquake is analyzed using the numerical procedure proposed in Chapter 3.

4.2 ANALYSIS OF CRACK PROPAGATION FOR KOYNA DAM UNDER THE 1967 EARTHQUAKE

The Koyna dam cross-section and its BE discretization are shown in Figure 4.2. To improve accuracy by limiting the difference in element size encountered over a domain, a transition subregion is introduced in the BE discretization of Figure 4.2(b). The characteristics of the Koyna concrete are listed in Table 4.1[12]. The elastic modulus of the foundation rock (7×10^4 MPa) is approximately twice that of the concrete. Considering the high stiffness of the foundation rock and the fact that the ground acceleration was obtained directly at the dam base, a rigid foundation and earthquake input applied directly at the base were assumed. The corresponding accelerograms of the ground motion are shown in Figure 4.3. The component in the cross-stream direction was assumed not to affect crack development and was therefore neglected. In the results to follow, seismic loading refers only to the effects of the components of the 1967 Koyna earthquake in both the horizontal stream-wise and the vertical directions, whereas static and dynamic loading includes the former as well as the hydrostatic force, the dam's self-weight and also the added mass hydrodynamic effect.

According to the field measurements taken after the 1967 earthquake as shown in Figure 4.1[12], most of the downstream cracks occurred at, or near, the location of slope change where the effect of stress concentration is expected to be significant. Accordingly, an initial crack was assumed to exist at elevation 66.5 m on the downstream face.

Results from many experiments[54] on the fracture toughness K_c of concrete with various specimen sizes show that K_c increases with increasing specimen size, and it is concluded that only those obtained by tests of large specimens are valid for concrete dams. The magnitude of K_c obtained from large test specimens ranges from 1.1 to 3.6 $\mathrm{MPa{\cdot}m^{1/2}}$. It is also found that the fracture toughness increases with increasing rate of loading, indicating that the dynamic fracture toughness K_d should exceed K_c. Based on these considerations, $K_d = 2.0\ \mathrm{MPa{\cdot}m^{1/2}}$ was employed in the present computations for the Koyna dam.

Time histories of the dam's response were computed considering contributions from up to six modes. As the crack extends, the frequencies and mode shapes of the dam structure change accordingly. Damping ratio $\xi = 0.05$ for all six modes was assumed. Based on the foregoing assumptions, the following behaviour was predicted for the Koyna dam prototype.

Pre-cracking analysis

The first four modal frequencies of the initially uncracked Koyna dam-reservoir system are compared with FE analysis[12] in Table 4.2. It is seen from Table 4.2 that BEM results are very close to those from FEM and thus serve to verify the accuracy of the present BE discretization. For load combination consisting of static and dynamic components, time step integration was performed with $\Delta t = 0.005$ sec and an earthquake duration of 6.0 sec.

The response of the dam in terms of the crest displacement and acceleration, and also the stresses on both upstream and downstream faces, was examined. The results may be summarized as follows: The horizontal displacement of the dam crest reached 43.6 mm in the downstream direction. The maximum accelerations at the crest were 22.8 $\mathrm{m/sec^2}$ and 22.6 $\mathrm{m/sec^2}$ in the horizontal and vertical directions, respectively, with corresponding amplification factors of 4.8 and 6.6. The computed maximum tensile stress of 6.69 MPa shown in Figure 4.4 occurred near the point of slope change on the downstream face and already itself far exceeds the tensile strength of the concrete, thus confirming that first cracking is indeed to be expected at the point of slope change.

Fracture analysis with crack extension

The process of crack propagation from the downstream toward the upstream face was analyzed next. As for the model dam, in these analyses it was assumed that the crack extends in increments 10-20 per cent of the existing length, but not greater than 1.0 m (0.5 m increment was also examined with very similar results). During these crack extensions remeshing of the dam is performed automatically by the program and no user intervention is needed. The CPU time to complete a typical fracture analysis requires approximately 85 minutes on a PC 486/50 computer.

To study the magnitude of the time step required for convergence in the computation of crack propagation, the cracking process under seismic load only was calculated for time steps $\Delta t = 0.001$ and 0.002 sec using both the force and impulse methods for simulation of crack closure. Since the convergence trends of the crack profile for the two methods are very similar, only the results from the force method are shown in Figure 4.5(a). It is seen that the cracking patterns obtained with $\Delta t = 0.001$ and 0.002 sec are extremely close. Nevertheless, in the following calculations $\Delta t = 0.001$ sec was adopted.

It is known that, for mode superposition analysis, use of the first four to five modes is sufficiently accurate to determine stresses in gravity dams under earthquake loading when crack propagation is not involved. To study convergence when fracture is of interest, the crack profiles were also computed using different numbers of modes N. The results for N = 5 and 6 are shown in Figure 4.5(b), from which it is noted that both profiles are in good agreement. To ensure accurate results, the first 6 modes were used in the remainder of the calculations.

To examine the performance of both the impulse and the force methods for modelling crack closure for the Koyna dam, Figure 4.6(a) compares the crack profiles considering only the seismic loading, whereas Figure 4.6(b) represents the practical case of static and dynamic loads combined. The time histories of the displacement at the crest and the stress intensity factors at the crack tip corresponding to Figure 4.6(b) are also compared in Figures 4.7 - 4.9. From these results, the following observations are noteworthy:

(1) The crack profiles of Figure 4.6 obtained by the two methods of modelling crack closure are in excellent agreement. The trajectories show an inclined downward orientation from the downstream to upstream faces. It appears that the crack closure models with or without the overlap assumption produce very similar crack configurations, thus implying that the crack closure mechanism does not have significant effect on the cracking process. From comparing Figures 4.6(a) and 4.6(b), it is also evident that the static loads do not affect the final crack pattern although they may delay the initiation of the extension.

(2) Comparing the crack profiles of Figure 4.6 with that of the model test shown in Figure 3.17, it is surprising that the profiles are nearly identical. Although the input of the shaking table in the model test is totally different from the earthquake excitation of the Koyna dam prototype and also since the effects of the self-weight and hydrostatic pressure were not properly included in the test, the crack profiles are still very similar. Since concrete and gypsum are brittle materials it appears that the crack extension, once it occurs, is so rapid that complete rupture accompanies the peak in the response, thus resulting in very similar profiles under different conditions.

(3) As shown in Figure 4.7, the overall trend of the time histories of the crest displacement is also similar for the two methods, although a significant discrepancy in the magnitude appears after the initial crack first opens at t = 0.78 sec. This is clearly due to the spurious overlap displacement permitted in the impulse method, since a shift of the solid curve toward the negative side (upstream direction) to remove the overlap would produce good agreement with the dashed curve representing the force model.

(4) Comparing Figures 4.8(a) and 4.9(a), it is evident that the stress intensity factor K_I for the opening mode behaves quite similarly in terms of peak response for both closure

simulations, particularly at the final stage. However, there are two main differences which need to be mentioned. First, small peaks are seen during the entire history for the force model while nothing appears between 1.1 - 1.7 sec for the impulse model. This difference is also due to the hypothetical overlap permitted in the impulse model for crack closure, in which no opening will occur during the small peaks in the excitation because of the initial overlap due to static loads. Secondly, many small irregular peaks occur for the force model due to displacement pulses imposed at the crack surfaces to adjust the overlap, whereas only velocity changes are imposed in the impulse model. Regarding stress intensity factors K_{II} for the sliding mode, similar differences as observed in the test of the model dam (Figure 3.15) are seen in Figures 4.8(b) and 4.9(b). As noted previously, the overlap assumption is again the cause of these differences. It is also seen that the time instants of rupture are 2.10 and 2.16 sec for the force and impulse methods, respectively. This slight time discrepancy between the two models arises because the latter needs more time steps to restore the overlap displacement. The patterns of the peak values of the combined stress intensity factor K which functions as the critical factor for crack propagation are also similar, especially at the instants of extension; thus very close crack profiles can still be obtained for the two methods as shown in Figure 4.6. As already noted for the model dam (Table 3.5), it is clear that the dominant trait in seismic crack propagation of gravity dams is fracture due to the opening mode, while the closing mechanism does not have a significant influence on the problem.

For the accelerograms shown in Figure 4.3, it is worth noting that the dam ruptures at the time which corresponds to ground accelerations 0.2 g and -0.25 g in the horizontal and vertical directions, respectively. Although these accelerations are smaller than the subsequent maximum values, the corresponding stress intensity factors already exceed the assumed fracture toughness causing the initial crack to propagate. From the prototype performance of the Koyna dam during the 1967 earthquake, the actual cracks were observed to be concentrated at elevation 60 - 65 m both on the upstream and downstream faces. On the other hand, all the current results for the crack profiles in both the model and prototype dams predict that the upstream Koyna cracks would have appeared at elevation 62 - 63 m. This is consistent with the aforementioned field observations.

4.3 CONCLUDING REMARKS

Employing the 2-D seismic fracture procedure presented in Chapter 3, the cracking process of the Koyna prototype dam under 1967 earthquake has been studied in detail. Results obtained by both impulse and force methods for simulation of crack closure mechanism are compared with previously obtained data from the rupture test of a model of the Koyna dam. Since the numerical results and the model test data show very similar patterns of rupture, also consistent with the prototype measurements after the 1967 earthquake, it is concluded that the proposed boundary element procedure based on fracture mechanics is suitable for modelling crack propagation in concrete gravity dams during strong earthquakes.

The foregoing 2-D BE procedure is extended in the following Chapter to treat 3-D static cracking in arch dams.

Table 4.1 Concrete properties of Koyna dam

Elastic modulus (MPa)	Poisson ratio	Specific weight (kN/m^3)	Damping ratio
31,000	0.2	25.9	0.05

Table 4.2 Frequencies (Hz) of Koyna dam

Method	f_1	f_2	f_3	f_4
BEM	3.07	7.98	11.2	16.5
FEM	3.07	8.20	10.8	15.9

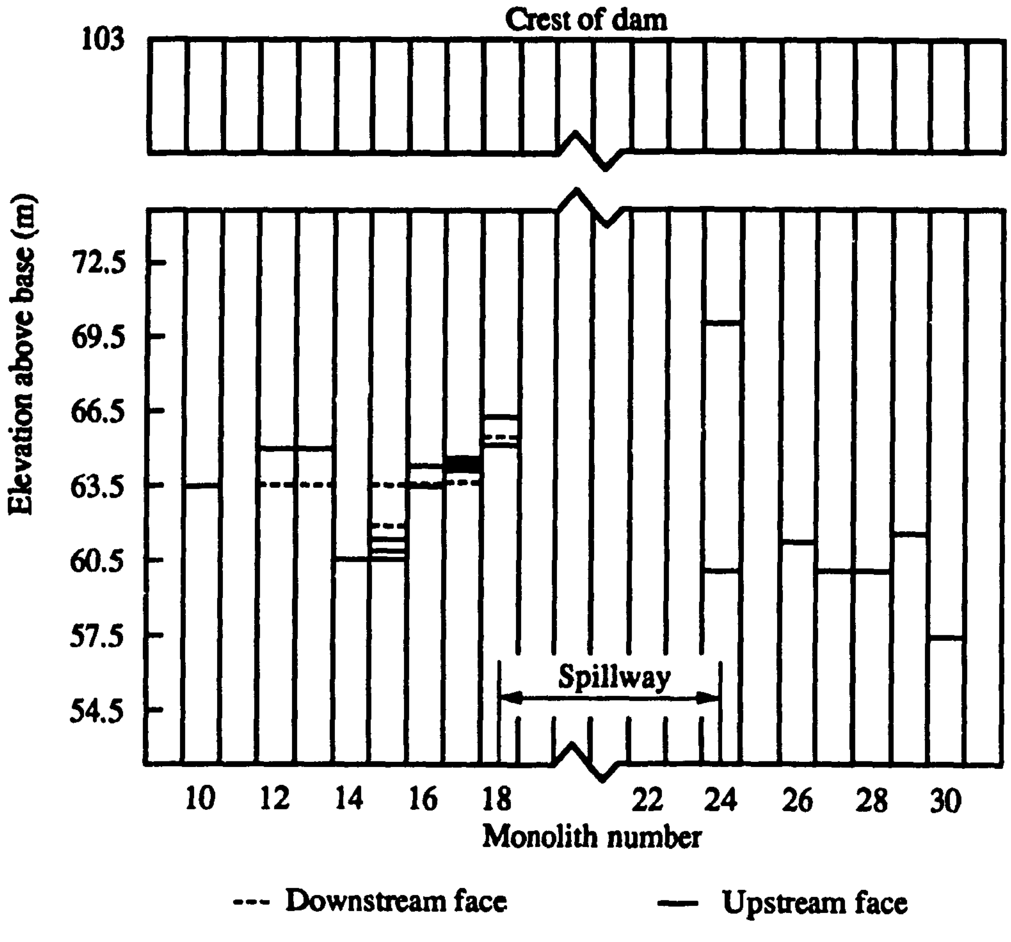

Figure 4.1 Observed pattern of cracking on faces of Koyna dam after 1967 earthquake, after Ref. 12

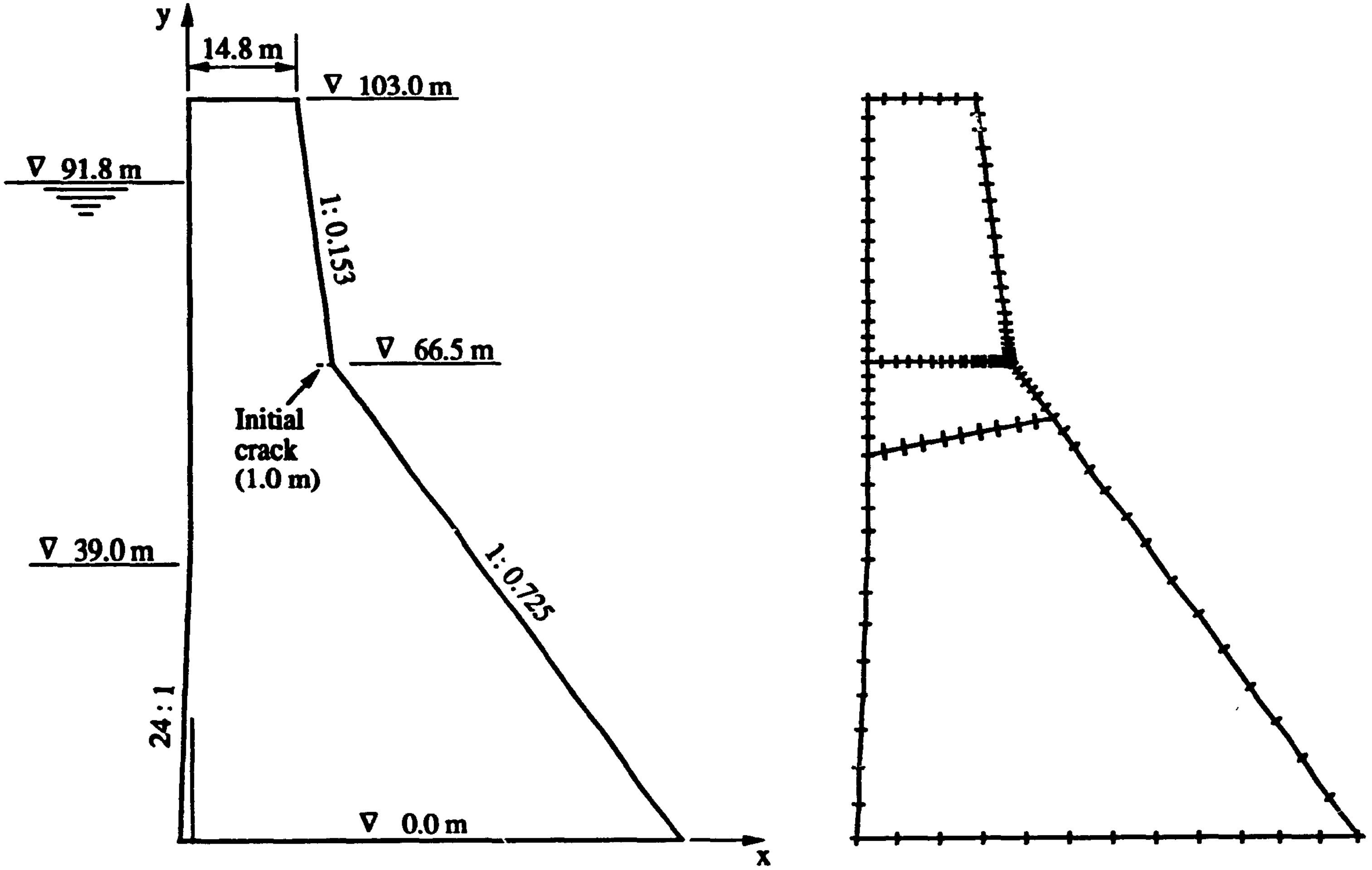

(a) Cross-section

(b) BE discretization

Figure 4.2 Koyna prototype dam

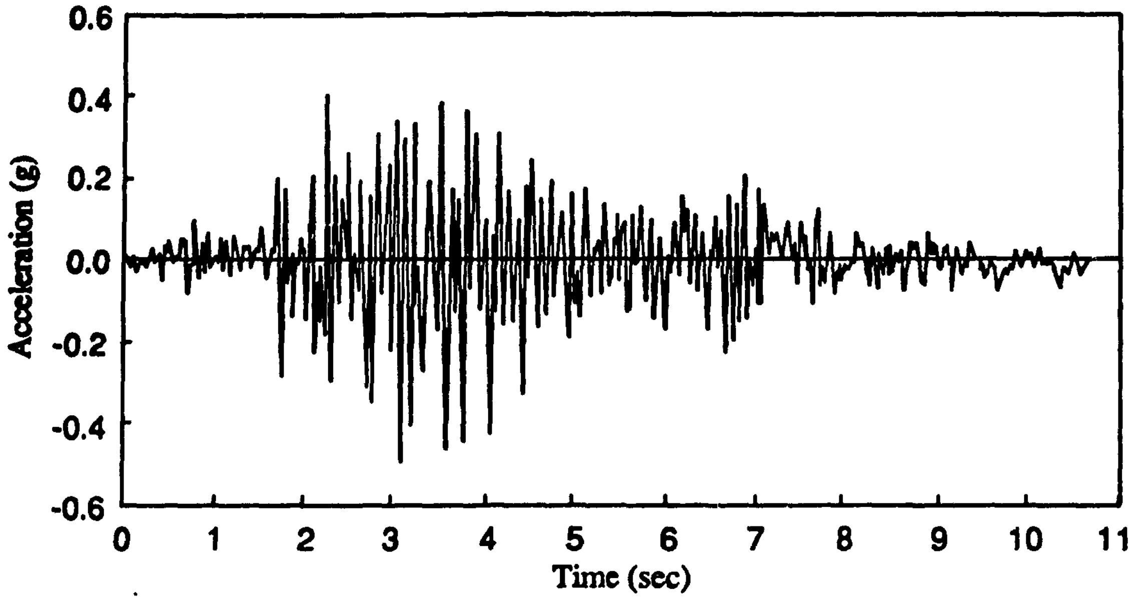

(a) Stream direction component

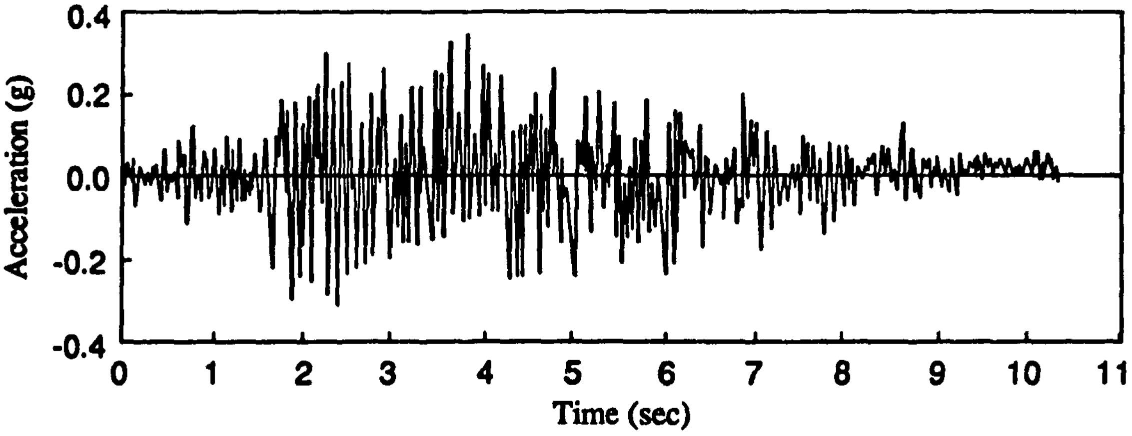

(b) Vertical component

Figure 4.3 Ground acceleration of Koyna earthquake, December 11, 1967

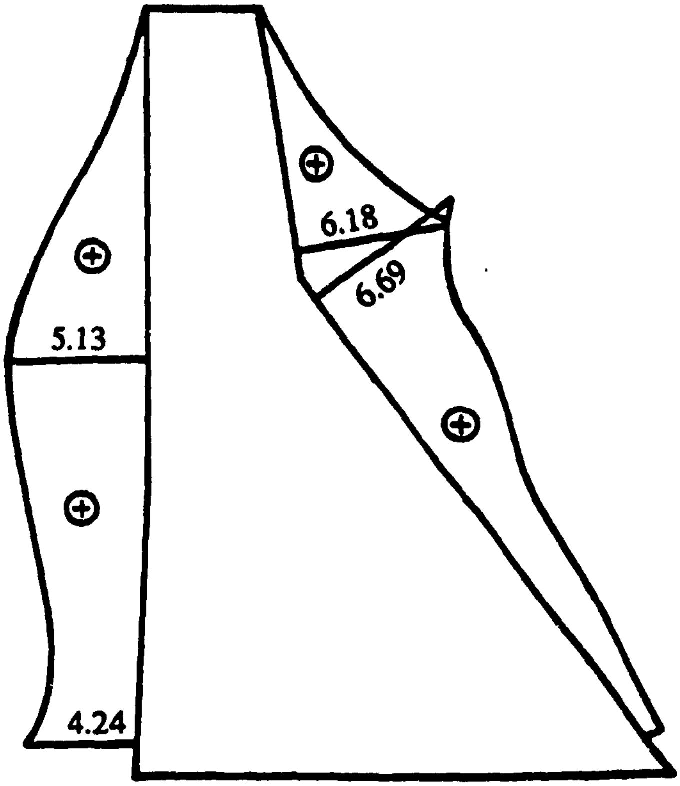

Figure 4.4 Maximum tensile stresses (MPa) in Koyna dam

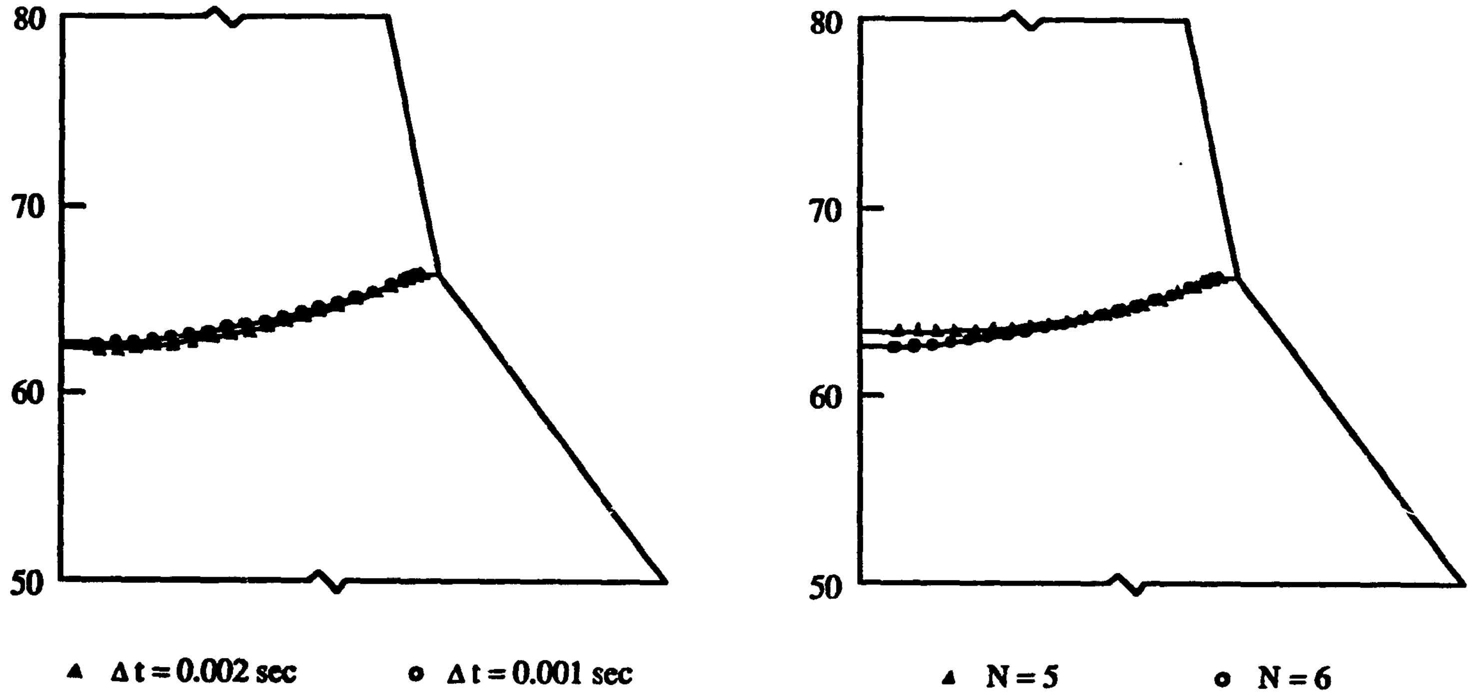

(a) Convergent test for time step Δ t

(b) Convergent test for number of modes N

Figure 4.5 Convergence of computed crack profile for Koyna dam under seismic loading only

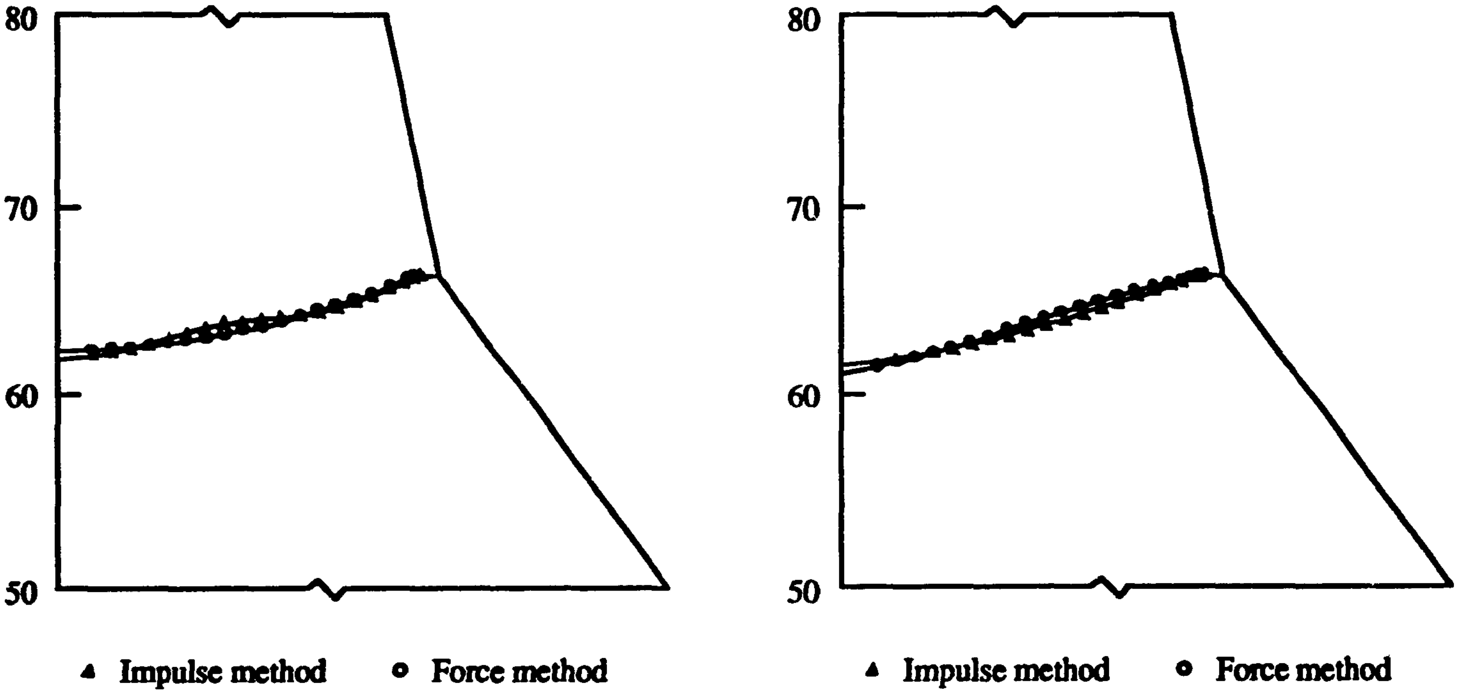

(a) Seismic loading only

(b) Static and dynamic loading

Figure 4.6 Comparison of crack profile for Koyna dam under different loading conditions and crack closure modelling

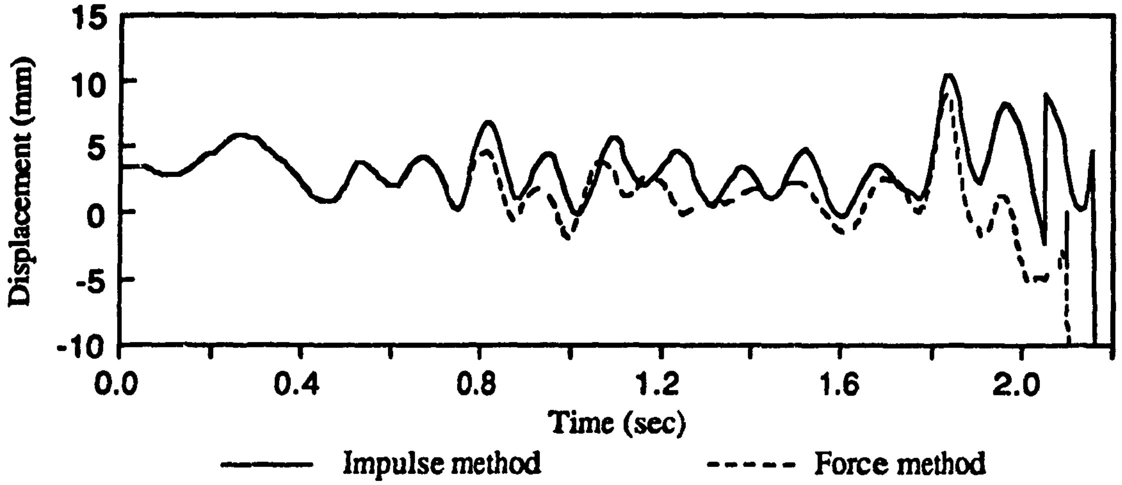

Figure 4.7 Comparison of time history of crest displacement for Koyna dam under different crack closure modelling

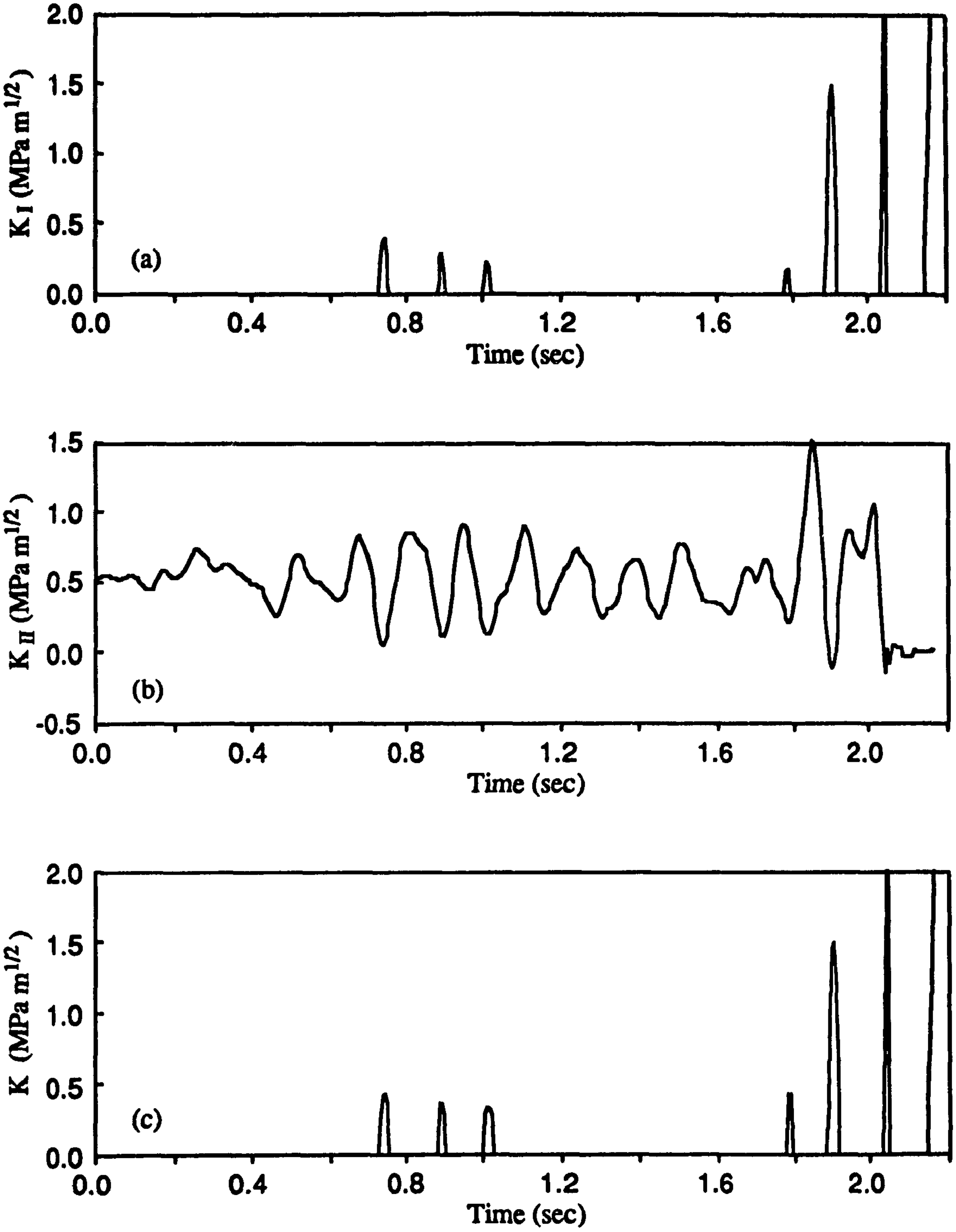

Figure 4.8 Time histories of stress intensity factors for Koyna dam computed by impusle method for crack closure

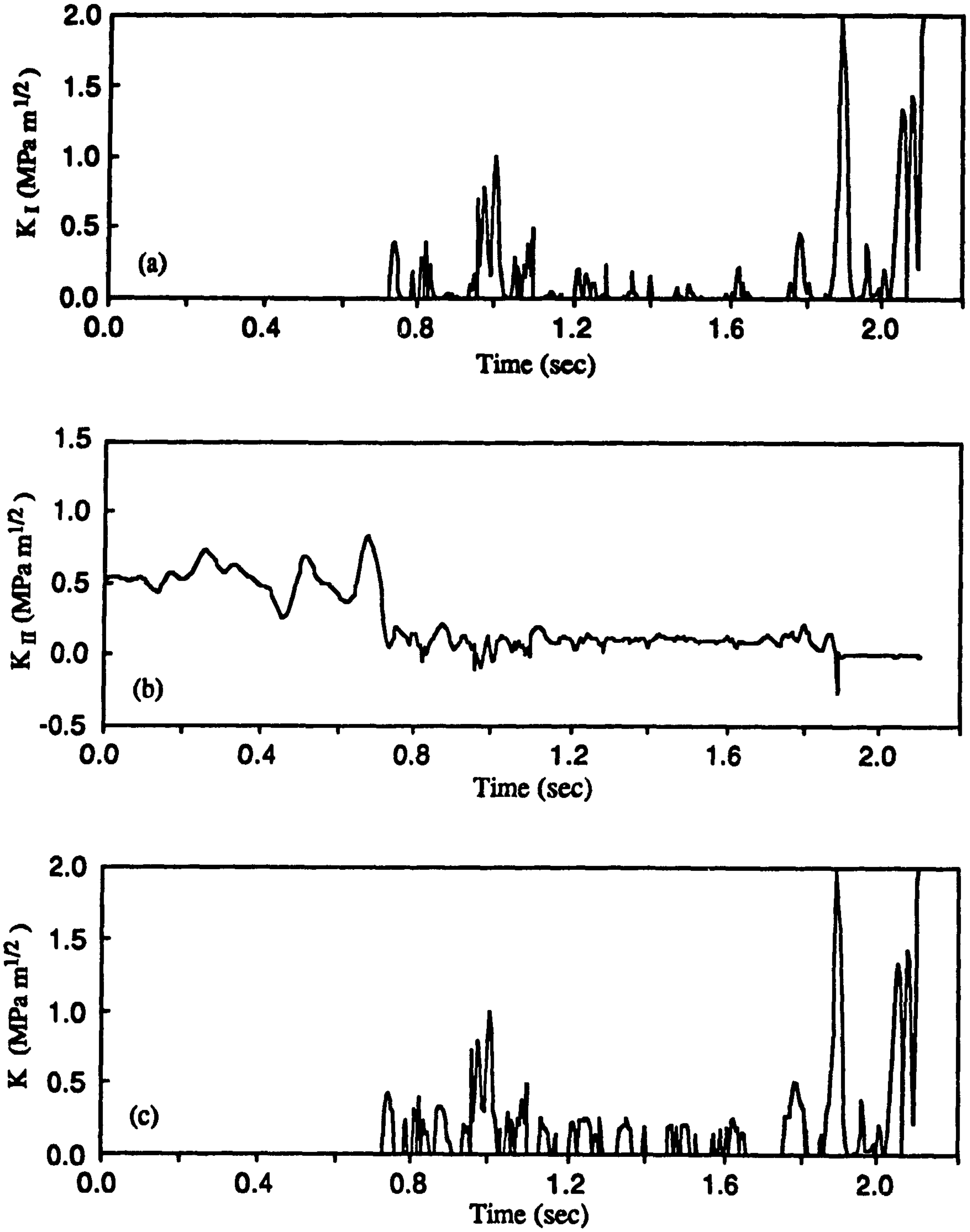

Figure 4.9 Time histories of stress intensity factors for Koyna dam computed by force method for crack closure

CHAPTER 5

3-D STATIC CRACKING ANALYSIS OF ARCH DAMS

With the objective of demonstrating the current BE based fracture mechanics formulation for the 3-D cracking problem posed by arch dams, this Chapter presents a simplified numerical procedure for these complex structures under static loading. The BE formulation for three-dimensional elastostatic fracture is derived with special crack front elements to improve the precision in computing 3-D stress intensity factors (SIFs). In order to evaluate accurately the singular integral corresponding to the special crack front element by standard Gaussian quadrature formulae, appropriate coordinate transformation is performed. The accuracy of the procedure in computing the 3-D stress intensity factors is verified by two examples. Finally, a simplified model for crack extension is proposed and its applicability to arch dams is discussed.

5.1 BOUNDARY ELEMENT FORMULATION OF 3-D ELASTOSTATICS

The 2-D static formulation presented in Chapter 2 is repeated in the following for the 3-D case since the fundamental solution and the meaning of subscripts are different.

Employing the residual approximation and using the 3-D Kelvin fundamental solution as the weighting function, the governing static equilibrium equation for a homogeneous isotropic elastic body Ω can be transformed to the following boundary integral equation[30]

$$c_{ij}(P)u_j(P)+\int_S T_{ij}(P,Q)u_j(Q)dS=\int_S U_{ij}(P,Q)t_j(Q)dS$$

$$+\int_\Omega U_{ij}(P,Q)b_j(Q)d\Omega \qquad (5.1)$$

where u_j (j=1, 2, 3) are the displacements, t_j the tractions at the surface S of the body Ω, b_j the body forces; P is the source point, Q the integration point, both on the boundary surface

$$c_{ij} = \lim_{\varepsilon \to 0} \int_{S_\varepsilon} T_{ij} dS_\varepsilon$$

in which S_ε is the spherical surface enclosed in the domain with radius ε and centre P; U_{ij} (P, Q) and T_{ij} (P, Q) are the 3-D Kelvin fundamental solution given by[30]

$$U_{ij}(P,Q) = \frac{(1+\nu)}{8\pi E(1-\nu)R}[(3-4\nu)\delta_{ij} + \frac{\partial R}{\partial x_i}\frac{\partial R}{\partial x_j}]$$

$$T_{ij}(P,Q) = -\frac{1}{8\pi(1-\nu)R^2}\{\frac{\partial R}{\partial n}[(1-2\nu)\delta_{ij} + 3\frac{\partial R}{\partial x_i}\frac{\partial R}{\partial x_j}] + (1-2\nu)(\frac{\partial R}{\partial x_j}n_i - \frac{\partial R}{\partial x_i}n_j)\} \tag{5.2}$$

where R is the distance from P to Q, δ_{ij} the Kronecker delta, n_i the unit outward normal at Q, E the elastic modulus, ν the Poisson's ratio, and x_i is the Cartesian coordinate.

If the surface S is discretized into m elements with r nodes each and if the displacements and tractions are represented in terms of nodal values through the r interpolation functions $\phi_{dr}(\xi)$ and $\phi_{tr}(\xi)$, respectively, equation (5.1) becomes

$$c_{ij}(p)u_j(p) + \sum_{l=1}^{m}\sum_{s=1}^{r} H_{ij}^{pls}u_j^{ls} = \sum_{l=1}^{m}\sum_{s=1}^{r} G_{ij}^{pls}t_j^{ls} \tag{5.3}$$

where body forces are disregarded and the source point P has been taken to coincide with the discretization node p. The coefficients H_{ij}^{pls} and G_{ij}^{pls} are given by

$$H_{ij}^{pls} = \int_{S_\xi} T_{ij}(P, Q^l(\xi))\phi_{ds}(\xi)J^l(\xi)d\xi \tag{5.4}$$

$$G_{ij}^{pls} = \int_{S_\xi} U_{ij}(P, Q^l(\xi))\phi_{ts}(\xi)J^l(\xi)d\xi \tag{5.5}$$

where $J(\xi) = dS/d\xi$ is the Jacobian of transformation ξ to x.

If we apply equation (5.3) to nodal point p and add the terms relating to the same node q, we have

$$\sum_{q=1}^{n} H*_{ij}^{pq} u_j^q = \sum_{q=1}^{n} G_{ij}^{pq} t_j^q \tag{5.6}$$

where n is the total number of nodes in the discretization.

After we apply equation (5.3) to all the n nodes, prescribe properly the boundary conditions and reorder the terms, equation (5.6) leads to a non-symmetric fully-populated system of 3n equations with 3n unknowns. When the body is divided into subdomains, from the conditions of compatibility and equilibrium on the interface between the subdomains α and β, we obtain

$$u_i^{(\alpha)} = u_i^{(\beta)} \quad , \quad t_i^{(\alpha)} = -t_i^{(\beta)}$$

When the node s of the element l coincides with point p, to avoid calculating directly c_{ij} and the strongly singular integral in equation (5.4), the coefficients $H*_{ij}^{pp}$ can be evaluated by applying the rigid body motion condition to equation (5.6):

$$H*_{ij}^{pp} = -\sum_{q=1}^{n} H*_{ij}^{pq} \quad (q \neq p)$$

All the other integrals in equations (5.4) and (5.5) are numerically calculated by Gaussian quadrature formula. In order to achieve a roughly uniform precision of integration, the order of the Gaussian formula is determined according to the rapidity of variation of the integrand within the element. When node p belongs to element l, the element is split into 2 or 3 triangles with a common vertex at p (see Figure 5.1). Each triangle is then transformed into a square in space ξ' so that the singularity 1/R in the kernel-interpolation function product is eliminated by the Jacobian of the transformation ξ' to ξ which is proportional to $(1+\xi'_2)$[55].

Body forces

For the self-weight and steady-state thermal loadings encountered in arch dams, the domain integral of the body force term in equation (5.1) can be suitably transformed into a surface integral, thus avoiding the need for the domain of the problem to be divided into internal cells for integration[56]. The body force term of equation (5.1) is represented as

$$B_i = \int_\Omega U_{ij}(P,Q)\, b_j(Q)\, d\Omega \tag{5.7}$$

(1) For the constant self-weight b_i, we have

$$B_i = \int_S W_i(P,Q)\, dS \tag{5.8}$$

where

$$W_i(P,Q) = \frac{1+\nu}{4\pi E}\left[b_i n_j \frac{\partial R}{\partial x_j} - \frac{1}{2(1-\nu)} b_j \frac{\partial R}{\partial x_j} n_i \right] \tag{5.9}$$

(2) For the steady-state temperature load, it can be shown that

$$B_i = \int_S \left[D_i(P,Q)\, T(Q) - F_i(P,Q) \frac{\partial T(Q)}{\partial x_j} n_j \right] dS \tag{5.10}$$

where

$$D_i(P,Q)=\frac{(1+\nu)\alpha}{8\pi(1-\nu)R}(n_i-\frac{\partial R}{\partial x_i}\frac{\partial R}{\partial x_j}n_j)$$

$$F_i(P,Q)=\frac{(1+\nu)\alpha}{8\pi(1-\nu)}\frac{\partial R}{\partial x_i} \tag{5.11}$$

in which α is the coefficient of thermal expansion and T represents the change in temperature from the time when the construction joints are grouted.

5.2 COMPUTATION OF STRESS INTENSITY FACTORS FOR 3-D CRACKS

A great deal of work has dealt with the computation of SIFs for 3-D crack problems. In early days, FEM was employed for this purpose. Raju and Newman[57] used thousands of degrees of freedom (up to 6900 DOF) to calculate the SIF of a wide range of semi-elliptical surface cracks in finite-thickness plates and obtained satisfactory results. However, for 3-D crack problems, FEM has been found to be very costly because the refining of the mesh in the vicinity of the crack front requires extensive computing resources and data preparation effort.

The boundary element method is a successful alternative and has been found to be particularly suitable for 3-D crack problems[58]-[62] because it avoids the discretization of the interior region of the structure, thus leading to better accuracy and much less data preparation.

Several strategies have been used to improve the accuracy in computing SIFs by BEM. The quarter-point element, which is extensively employed in FEM and is the simplest one, can be directly applied in BEM. However, this method is less accurate since it only correctly models the displacement behaviour in the vicinity of the crack front. For elliptical cracks, Luo et al.[61] employed the parametric form of the equation for an ellipse to represent the contour of the crack exactly so that the error resulting from the quadratic interpolation function for an ellipse can be reduced. The most popular method is to employ special crack front elements to model the behaviour of both the displacement and stress fields around the crack front. Results obtained by Luchi et al.[58] and Tanaka et al.[59] show that this method improves accuracy significantly. Since the method of using special crack front elements yields better accuracy and is easy to be incorporated into BEM code, it is adopted herein.

Special crack front element

In the immediate vicinity of the crack front, by utilizing only the first term of the power series given by Irwin[63] and Williams[64], the displacements u_1, u_2 and u_3 in directions x_1, x_2 and x_3 (respectively parallel to the normal, binormal and tangent to the crack edge) can be expressed in polar co-ordinates as [see Figure 5.2(a) for $\phi=0$]:

$$u_1=\frac{1+\nu}{4E}\sqrt{\frac{2r}{\pi}}\,\{K_I[(5-8\nu)\cos\frac{\theta}{2}-\cos\frac{3\theta}{2}]+K_{II}[(9-8\nu)\sin\frac{\theta}{2}+\sin\frac{3\theta}{2}]\}$$

$$u_2=\frac{1+\nu}{4E}\sqrt{\frac{2r}{\pi}}\,\{K_I[(7-8\nu)\sin\frac{\theta}{2}-\sin\frac{3\theta}{2}]-K_{II}[(3-8\nu)\cos\frac{\theta}{2}+\cos\frac{3\theta}{2}]\} \quad (5.12)$$

$$u_3=\frac{2(1+\nu)}{E}\sqrt{\frac{2r}{\pi}}\,K_{III}\sin\frac{\theta}{2}$$

where K_I, K_{II}, K_{III} denote the stress intensity factors in the opening, sliding and tearing modes, respectively; and E, ν are the elastic modulus and Poisson's ratio, respectively. The stress components are given by

$$\sigma_{11}=\frac{1}{\sqrt{2\pi r}}[K_I\cos\frac{\theta}{2}(1-\sin\frac{\theta}{2}\sin\frac{3\theta}{2})-K_{II}\sin\frac{\theta}{2}(2+\cos\frac{\theta}{2}\cos\frac{3\theta}{2})]$$

$$\sigma_{22}=\frac{1}{\sqrt{2\pi r}}[K_I\cos\frac{\theta}{2}(1+\sin\frac{\theta}{2}\sin\frac{3\theta}{2})+K_{II}\sin\frac{\theta}{2}\cos\frac{\theta}{2}\cos\frac{3\theta}{2}]$$

$$\begin{aligned}
\sigma_{33} &= 2\nu(\sigma_{11}+\sigma_{22}) \\
\sigma_{12} &= \frac{1}{\sqrt{2\pi r}}\left[K_I \sin\frac{\theta}{2}\cos\frac{\theta}{2}\cos\frac{3\theta}{2} + K_{II}\cos\frac{\theta}{2}\left(1-\sin\frac{\theta}{2}\sin\frac{3\theta}{2}\right)\right] \\
\sigma_{23} &= \frac{1}{\sqrt{2\pi r}} K_{III}\cos\frac{\theta}{2} \\
\sigma_{31} &= -\frac{1}{\sqrt{2\pi r}} K_{III}\sin\frac{\theta}{2}
\end{aligned} \tag{5.13}$$

Based on both $r^{1/2}$ displacement variation and $r^{-1/2}$ traction variation around the crack front as shown in equations (5.12) and (5.13), two kinds of interpolation functions are compared.

Method 1

If the displacements near the crack front are expressed in the form of

$$u = a_1 + a_2 r^{1/2} + a_3 r \tag{5.14}$$

where a_i (i=1, 2, 3) are coefficients to be determined and r denotes the distance from the crack front, then we have the following interpolation functions for the displacements proposed by Luchi et al.[58] when letting nodes 1, 5 and 2 be on the crack front [$\xi_2 = -1$ in Figure 5.2(b)]:

$$\phi_{d1}(\xi) = \frac{1}{2}(1-\xi_1)\left[-\xi_1 - \left(1-\frac{\sqrt{2}}{2}\xi_1\right)\sqrt{1+\xi_2} + \frac{\sqrt{2}}{2}(1+\xi_2)\right]$$

$$\phi_{d2}(\xi) = \frac{1}{2}(1+\xi_1)\left[\xi_1 - \left(1+\frac{\sqrt{2}}{2}\xi_1\right)\sqrt{1+\xi_2} + \frac{\sqrt{2}}{2}(1+\xi_2)\right]$$

$$\phi_{d3}(\xi) = \frac{1}{4}(1+\xi_1)\left[\sqrt{2}\,(\xi_1 - 2 - \sqrt{2})\sqrt{1+\xi_2} + (2+\sqrt{2})(1+\xi_2)\right]$$

$$\begin{gathered}
\phi_{d4}(\xi)=\frac{1}{4}(1-\xi_1)[-\sqrt{2}(\xi_1+2+\sqrt{2})\sqrt{1+\xi_2}+(2+\sqrt{2})(1+\xi_2)] \\
\phi_{d5}(\xi)=(1-\xi_1^2)(1-\frac{\sqrt{2}}{2}\sqrt{1+\xi_2}) \\
\phi_{d6}(\xi)=\frac{1}{2}(1+\xi_1)[(2+\sqrt{2})\sqrt{1+\xi_2}-(1+\sqrt{2})(1+\xi_2)] \\
\phi_{d7}(\xi)=\frac{\sqrt{2}}{2}(1-\xi_1^2)\sqrt{1+\xi_2} \\
\phi_{d8}(\xi)=\frac{1}{2}(1-\xi_1)[(2+\sqrt{2})\sqrt{1+\xi_2}-(1+\sqrt{2})(1+\xi_2)]
\end{gathered} \tag{5.15}$$

The corresponding interpolation functions for tractions $\phi_{ti}(\xi)$ (i=1, 2, ..., 8) are obtained from $\phi_{di}(\xi)$ by dividing by $(1+\xi_2)^{1/2}$ and, additionally, multiplying ϕ_{d3}, ϕ_{d4} and ϕ_{d7} by $\sqrt{2}$.

Method 2

On the other hand, if the displacements near the crack front are expressed in the form of

$$u=a_1r^{1/2}+a_2r+a_3r^{3/2} \tag{5.16}$$

the following interpolation functions for the displacements suggested by Tanaka et al.[59] can be derived:

$$\phi_{d1}(\xi)=\frac{1}{4}(1-\xi_1)(\sqrt{1+\xi_2}-\sqrt{2})[\sqrt{2}\,\xi_1+\sqrt{2}(1+\xi_2)]$$

$$\phi_{d2}(\xi)=\frac{1}{4}(1+\xi_1)(\sqrt{1+\xi_2}-\sqrt{2})[-\sqrt{2}\,\xi_1+\sqrt{2}(1+\xi_2)]$$

$$\begin{aligned}
\phi_{d3}(\xi) &= \frac{1}{4}(1+\xi_1)\sqrt{1+\xi_2}\,[\sqrt{2}\,\xi_1 - 2(1+\sqrt{2})\sqrt{1+\xi_2} + (2+\sqrt{2})(1+\xi_2)] \\
\phi_{d4}(\xi) &= \frac{1}{4}(1-\xi_1)\sqrt{1+\xi_2}\,[-\sqrt{2}\,\xi_1 - 2(1+\sqrt{2})\sqrt{1+\xi_2} + (2+\sqrt{2})(1+\xi_2)] \\
\phi_{d5}(\xi) &= \frac{1}{2}(1-\xi_1^2)[2-\sqrt{2(1+\xi_2)}\,] \\
\phi_{d6}(\xi) &= \frac{1}{2}(1+\xi_1)\sqrt{1+\xi_2}\,[(2+\sqrt{2})\sqrt{1+\xi_2} - (1+\sqrt{2})(1+\xi_2)] \\
\phi_{d7}(\xi) &= \frac{\sqrt{2}}{2}(1-\xi_1^2)\sqrt{1+\xi_2} \\
\phi_{d8}(\xi) &= \frac{1}{2}(1-\xi_1)\sqrt{1+\xi_2}\,[(2+\sqrt{2})\sqrt{1+\xi_2} - (1+\sqrt{2})(1+\xi_2)]
\end{aligned} \tag{5.17}$$

The corresponding interpolation functions $\phi_{ti}(\xi)$ ($i=1, 2, \ldots, 8$) for tractions are derived from $\phi_{di}(\xi)$ by dividing by $(1+\xi_2)$ and, in addition, multiplying ϕ_{d3}, ϕ_{d4} and ϕ_{d7} by 2.

Integration procedures for special crack front element

Whenever an integration is performed over a special crack front element and the source point does not belong to the element, the singularity $(1+\xi_2)^{-1/2}$ in $\phi_t(\xi)$ leads to evaluating a singular integral. In order to accurately evaluate the integral by standard Gaussian quadrature formulae, the following transformation is employed:

$$\begin{cases} \xi_1 = \xi_1^* \\ (1+\xi_2) = \dfrac{1}{2}(1+\xi_2^*)^2 \end{cases} \quad \text{for} \quad \begin{cases} -1 \le \xi_1^* \le 1 \\ -1 \le \xi_2^* \le 1 \end{cases} \tag{5.18}$$

Thus, the Jacobian

$$\frac{d\xi_1 d\xi_2}{d\overset{*}{\xi}_1 d\overset{*}{\xi}_2}=(1+\overset{*}{\xi}_2)=\sqrt{2}\sqrt{1+\xi_2} \qquad (5.19)$$

removes the singularity $(1+\xi_2)^{-1/2}$ in $\phi_t(\xi)$.

When the source point belongs to the crack element, the integration over such an element can be accurately evaluated by a double mapping transformation. The details of the procedure are available in Reference [58] and not repeated here.

Stress intensity factors

Substituting $\theta=\pm\pi$ into equation (5.12) and employing the displacements on the crack surfaces near the crack front as shown in Figure 5.2(a), lead to the following expressions for the stress intensity factors (SIFs):

$$K_I=\frac{E}{4(1-\nu^2)}\sqrt{\frac{\pi}{2}}\frac{[2\sqrt{2}(u_2^B-u_2^{B'})-(u_2^A-u_2^{A'})]}{\sqrt{L}}$$

$$K_{II}=\frac{E}{4(1-\nu^2)}\sqrt{\frac{\pi}{2}}\frac{[2\sqrt{2}(u_1^B-u_1^{B'})-(u_1^A-u_1^{A'})]}{\sqrt{L}} \qquad (5.20)$$

$$K_{III}=\frac{E}{4(1+\nu)}\sqrt{\frac{\pi}{2}}\frac{[2\sqrt{2}(u_3^B-u_3^{B'})-(u_3^A-u_3^{A'})]}{\sqrt{L}}$$

where superscripts A, B, A', B' denote the node points of the crack-front elements and L represents the length of the element in the normal direction at point C [see Figure 5.2(a)].

5.3 CRITERION OF 3-D CRACK PROPAGATION

Fracture mechanics theory for 2-D problems is well established and has been verified by a number of experiments. However, due to the much greater complexity, the corresponding theory for 3-D problems is still in the developmental stage. Although the stress intensity factors for an arbitrary 3-D crack can now be determined by numerical methods, the available criteria to predict the orientation of the crack extension are, in practice, not applicable for arbitrary crack geometry. Two criteria, namely the maximum energy release rate theory and the strain energy density factor (S-theory hereafter), are valid for three-dimensional crack problems. The S-theory[65] is adopted herein. This theory assumes that the direction of crack propagation is toward the minimum region of strain energy density factor S and that the crack extends when S_{min} reaches the critical value S_{cr}, which is a material constant. The length r_0 of the crack extension is assumed to be proportional to S_{min}. The strain energy density factor itself is represented by the quadratic form

$$S = a_{11} K_I^2 + 2 a_{12} K_I K_{II} + a_{22} K_{II}^2 + a_{33} K_{III}^2 \tag{5.21}$$

where a_{11}, a_{12}, a_{22}, a_{33} are coefficients depending on the spherical angles θ and ϕ of Figure 5.2(a) as follows:

$$\begin{aligned}
a_{11} &= \frac{\kappa+1}{16\mu\lambda\kappa^2\cos\theta}\left[2(1-2\nu)+\frac{\kappa-1}{\kappa}\right] \\
a_{12} &= \frac{\sqrt{\kappa^2-1}}{8\mu\lambda\kappa^2\cos\theta}\left[\frac{1}{\kappa}-(1-2\nu)\right] \\
a_{22} &= \frac{1}{16\mu\lambda\kappa^2\cos\theta}\left[4(1-\nu)(\kappa-1)+\frac{1}{\kappa}(\kappa+1)(3-\kappa)\right]
\end{aligned} \tag{5.22}$$

$$a_{33} = \frac{1}{4\,\mu\,\lambda\,\kappa\cos\theta}$$

in which μ is the shear modulus. For an elliptical crack, with major and minor semi-axes a and b, respectively, and given by

$$\begin{aligned} x &= a\cos\beta \\ y &= b\sin\beta \end{aligned} \tag{5.23}$$

the parameters λ and κ in Equation (5.22) are defined by the following expressions in terms of spherical angles θ, ϕ, parametric angle β and the ratio b/a:

$$\begin{aligned} \lambda &= \cos\phi + \frac{b^2 - a^2}{a\,b}\sin\phi\sin\beta\cos\beta \\ \kappa &= \pm\sqrt{1 + (\tan\theta/\lambda)^2} \end{aligned} \tag{5.24}$$

The minimum of S is obtained by letting the derivatives of S with respect to θ and ϕ vanish, i.e.

$$\frac{\partial S}{\partial \theta} = 0 \quad , \quad \frac{\partial S}{\partial \phi} = 0 \tag{5.25}$$

The difficulty in dealing with a 3-D crack is the reason few, if any, experiments involving 3-D crack propagation have been conducted to verify the S-theory. Although this theory applies, in principle, to any 3-D crack, the displacement or stress fields near the front of an arbitrary crack geometry are too complicated to derive the minimum of S. Thus the S-theory can, in reality, only be applied to plane elliptical cracks, for which S_{min} is available at present. Sih[65] applied the theory to the propagation of a flat elliptical crack in an infinite medium under an inclined, remote uniform load as shown in Figure 5.3. However, it is found that after one step of extension the new crack surface becomes distorted and no longer elliptical, thus rendering it impossible to consider further propagation.

5.4 VERIFICATION OF ACCURACY IN COMPUTING 3-D SIFS

The foregoing crack-front element and the corresponding integration procedures are incorporated into the developed software FAPAD (Fracture Analysis Program for Arch Dams). To model the infinite region of the foundation of an arch dam efficiently, the infinite boundary element technique presented by Zhang et al.[66] is also coded into FAPAD. Two examples are studied to verify the accuracy of the proposed method in computing 3-D stress intensity factors. In the following computations, 4 to 8 node isoparametric quadrilateral elements are employed for all the boundary except the adjacent region connecting the crack front where the special crack front elements are adopted.

Example 1

The opening mode SIF for a solid cylinder with an embedded horizontal circular crack subjected to unit uniform axial tension at both ends is computed. Because of the symmetry, only one-eighth of the cylinder and its dimension are shown in Figure 5.4 and the BEM discretization is illustrated in Figure 5.5. The numerical results for K_I are compared with the analytical solution[67] for homogeneous extension of an infinite body with a disk-shape slit which is given by: $2\sigma(a/\pi)^{1/2}$, where σ is the uniform tensile stress applied at infinity and 'a' is the radius of the crack. Table 5.1 shows the percentage error of K_I by the two methods presented in Section 5.2 for different meshes and lengths of crack front element, where mesh 1 has 34 elements and mesh 2 is refined around the crack front with a total of 42 elements. It is seen from Table 5.1 that method 1 has better accuracy than method 2 and, with $L/a = 0.1\sim0.2$ and appropriate mesh (i.e. $L/a = 0.1$ by mesh 2 and $L/a = 0.2$ by meshes 1 and 2), good accuracy (within 3% error) is achieved for method 1.

Example 2

The second example is also a solid cylinder subjected to unit uniform axial tension at both ends, but with an inclined embedded circular crack as shown in Figure 5.6. Figure 5.7 shows the BE discretization of the problem. The length/radius ratio $L/a = 0.2$ is adopted and a total of 244 elements are employed for this test example. Since method 1 has better accuracy than method 2, hereafter all numerical analyses are performed by method 1. The numerical results in terms of the three stress intensity factors K_I, K_{II} and K_{III} along the crack front are shown in Figure 5.8 and compared with the following analytical solution for an embedded circular crack in an infinite medium derived from Reference [68]:

$$K_I = 2\cos^2\left(\frac{\pi}{6}\right)\sqrt{\frac{a}{\pi}}$$

$$K_{II} = \frac{4\sin\left(\frac{\pi}{6}\right)\cos\left(\frac{\pi}{6}\right)}{(2-\nu)}\sqrt{\frac{a}{\pi}}\cos\beta \tag{5.26}$$

$$K_{III} = \frac{4(1-\nu)\sin\left(\frac{\pi}{6}\right)\cos\left(\frac{\pi}{6}\right)}{(2-\nu)}\sqrt{\frac{a}{\pi}}\sin\beta$$

where ν denotes Poisson's ratio; 'a' represents the radius of the crack, and β is the angle shown in Figure 5.6. It is seen from Figure 5.8 that the BEM results are in excellent agreement with the analytical solutions, thus confirming the high accuracy of the present method in computing 3-D stress intensity factors.

5.5 SIMPLIFIED MODEL OF CRACK EXTENSION FOR ARCH DAMS

Since the S-theory can only be applied to plane elliptical cracks, even in the simple case of an infinite medium and uniform loading, only a single step of crack extension is possible, as noted in Section 5.3. Obviously this rules out rigorous application of this theory to arch dams for simulation of multi-step crack propagation at the present time. The following two hypotheses are therefore made, in order to obtain a simplified model of the 3-D crack propagation criterion for arch dams:

(i) Instead of an elliptical crack geometry, a through-crack is assumed in the dam, i.e. the crack front is a straight line, equivalent to the extreme case of the a/b ratio approaching infinity for an elliptical curve.

(ii) The direction of crack extension at all points along the crack front is the one determined at the center point of the front, implying that the entire crack front will extend in the direction determined by S-theory at the center point, and with the same predetermined length. Thus, the new crack front remains straight.

The above two assumptions are elaborated in Figure 5.9. An initial through-crack is assumed on upstream face near the foundation of an arch dam at location "1" and the SIFs are calculated by 3-D BEM under the relevant loading conditions. After the direction of crack propagation at the center point of the crack front is determined by the S theory, the whole crack front extends along this direction to the location "2" with the new crack front retaining straight line. Repeating the above step by step procedure until the extension of the crack stops. In this way, the trajectories of the crack propagation in arch dams can be traced by multi-step crack extensions.

Although the foregoing assumptions reduce the criterion for crack propagation to that of 2-D computed at the centre point, this simplified 3-D model represents important improvements over a pure 2-D procedure for arch dams with regard to the following aspects: (i) Taking the geometrical conditions of the dam and foundation into account, the redistribution of the stress fields associated with arch and cantilever actions can be simulated accurately during the entire crack extension process; and (ii) The lateral extension of the through-crack can be prescribed according to either the topography of the dam-foundation interface if the crack is located near the foundation, or to the geometry of the dam surface when it occurs across the upstream or downstream faces. It should be noted that these advantages over a 2-D model have significant effects on crack development in arch dams, especially when the cracking extends from the upstream face into the dam body which leads to a significant increase in arch action.

To examine the validity of assuming a constant direction along the crack front for crack growth, a horizontal through-crack 2.0 m in depth is assumed on the upstream face near the foundation of the 102 m high three-centered Jinshui Tan arch dam[7], as shown in Figure 5.10. The material properties of the dam and its foundation are listed in Table 5.2. The loadings include the self-weight of the dam and the hydrostatic pressure of the reservoir, with full water head on the crack surfaces. The BE discretization of the cracked dam and the foundation is shown in Figure 5.11, where infinite boundary elements are employed to model the remote regions of the foundation. The variation of propagation direction θ along the crack front according to the S-theory is presented in Figure 5.12 for the first two steps of crack propagation. Due to the symmetry of the dam, only the results for half of the crack are shown. It is seen that θ is nearly constant over more than half of the central portion of the crack front, indicating use of θ determined at only the center point produces sufficient accuracy for more than half the crack front. Beyond this region, boundary restraint is seen to affect direction θ rather strongly.

Concerning the straight-line assumption for the crack geometry, the following observations should be noted. All the horizontal surface cracks which occurred on the Dragan arch dam[2] during the construction stage spread over the whole widths of the blocks, with depth ranging from 0.2 to 1.2 m. This suggests that the small initial surface cracks resemble a through-type crack. The lateral extent of the trace of the crack on the upstream face of the Kolnbrein arch dam covers a central span of 100 m[22], implying also that the cracking in this dam extends approximately in the fashion of a through-crack. These observations thus provide justification for the hypothesis of a through-crack as introduced in the present simplified model for crack propagation in arch dams.

5.6 CONCLUDING REMARKS

A simplified model for 3-D crack extension in arch dams under static loading has been presented. The validity of the assumptions introduced in this model was examined by using an example arch dam. The good accuracy of the BE procedure in computing 3-D SIFs was verified by two examples of cylinders with embedded cracks.

The above 3-D static BE procedure is applied, in the following Chapter, to a detailed study of the cracking of the Kolnbrein arch dam.

Table 5.1 Percentage error of K_I for example 1

Method	L/a	Mesh	Error (%)
1	0.1	1	8.2
		2	1.0
	0.2	1	1.2
		2	2.6
2	0.1	1	8.2
		2	1.7
	0.2	1	2.8
		2	7.1

Table 5.2 Material properties of Jinshui Tan arch dam

Property Material	Elastic modulus (MPa)	Poisson ratio	Specific weight (kN/m^3)
Dam concrete	21, 600	0.2	23.5
Foundation rock	16, 000	0.2	25.0

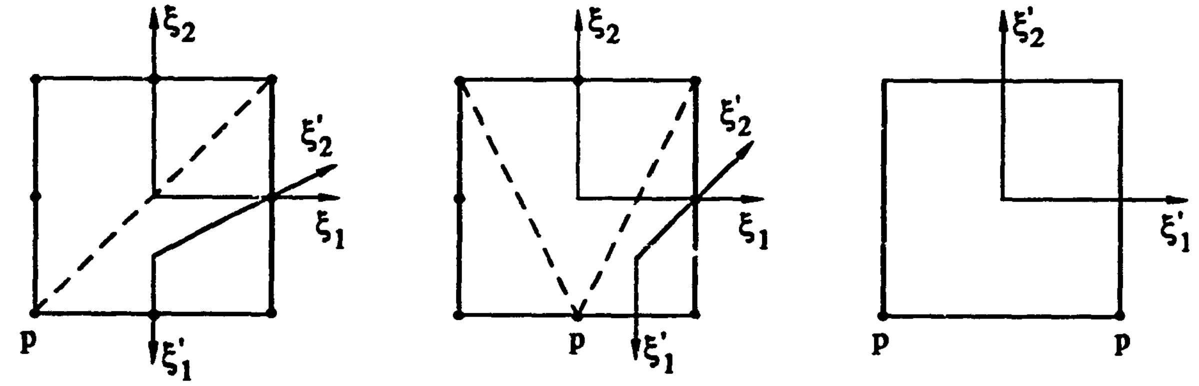

(a) Split into 2 triangles (b) Split into 3 triangles (c) ξ' coordinate system

Figure 5.1 Integration schemes for an element

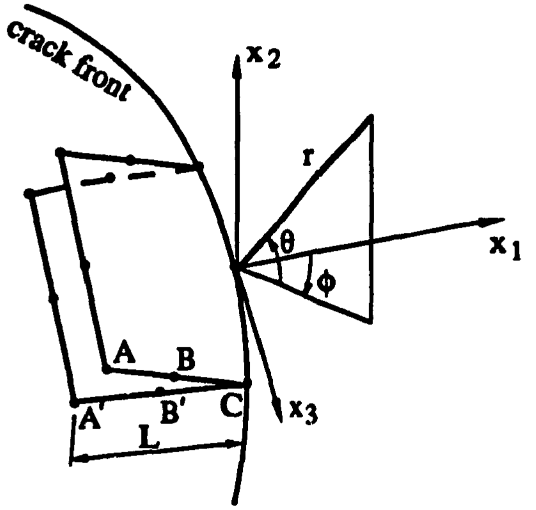

(a) Coordinate system for crack front

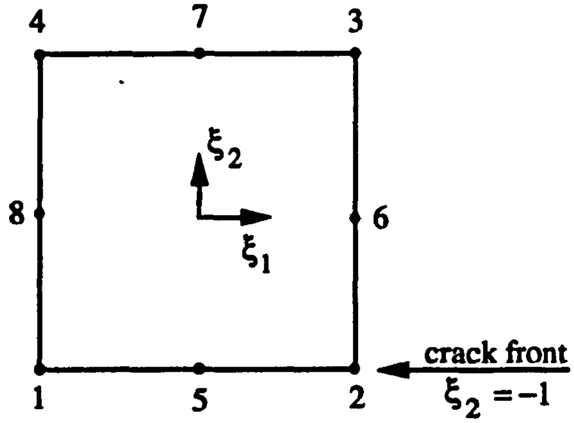

(b) Special crack front element

Figure 5.2 Coordinate system and special crack element

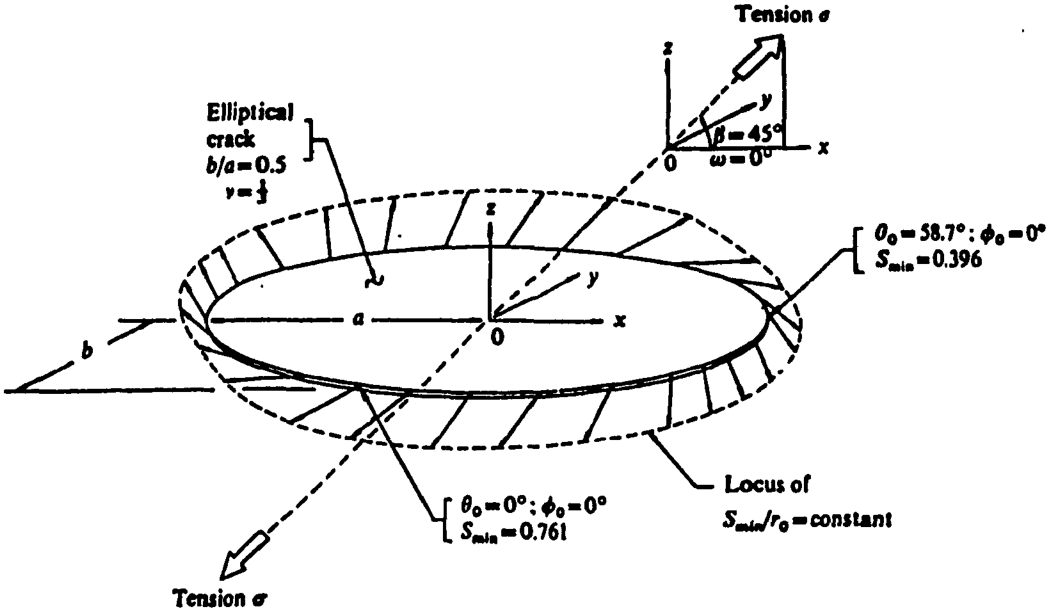

Figure 5.3 Initial fracture surface of an elliptical crack under tension, after Sih

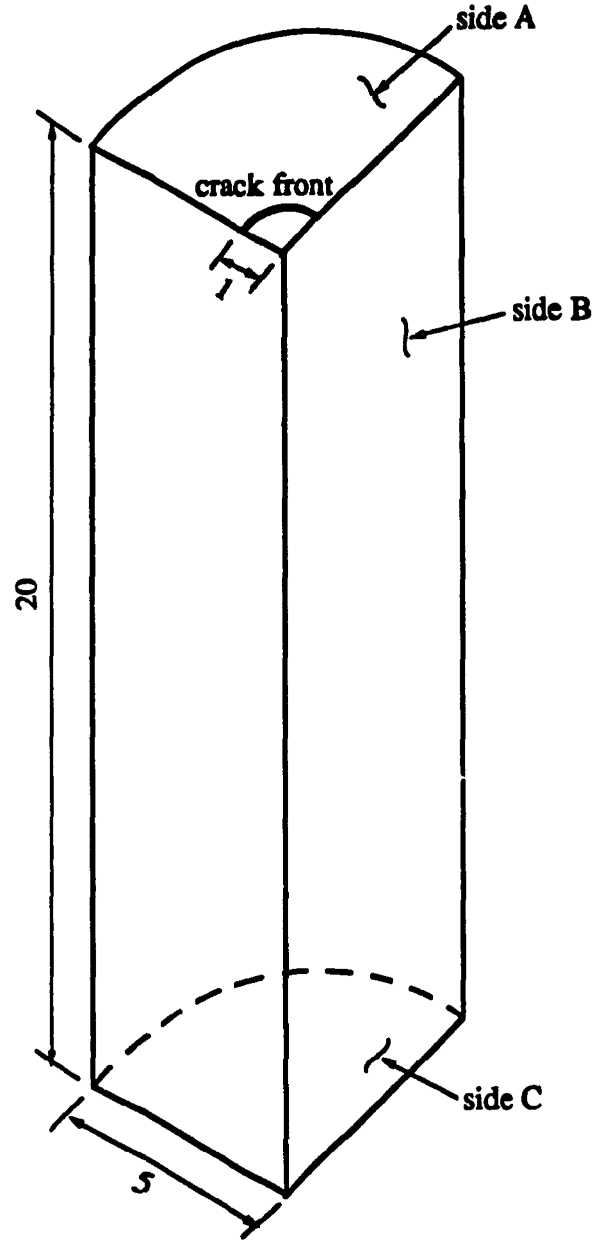

Figure 5.4 Cylinder for example 1

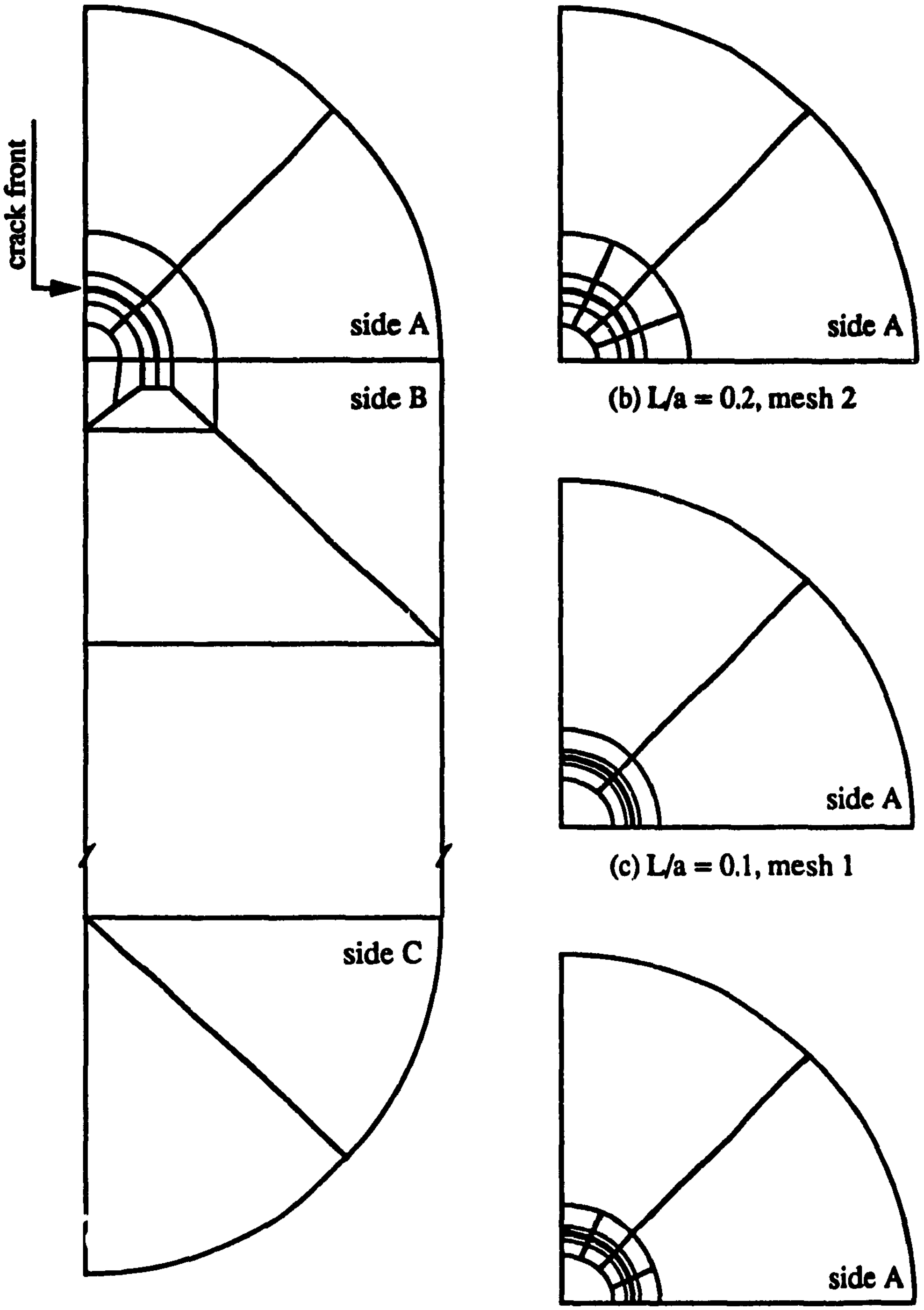

(a) L/a = 0.2, mesh 1

(b) L/a = 0.2, mesh 2

(c) L/a = 0.1, mesh 1

(d) L/a = 0.1, mesh 2

Figure 5.5 BE discretization for example 1

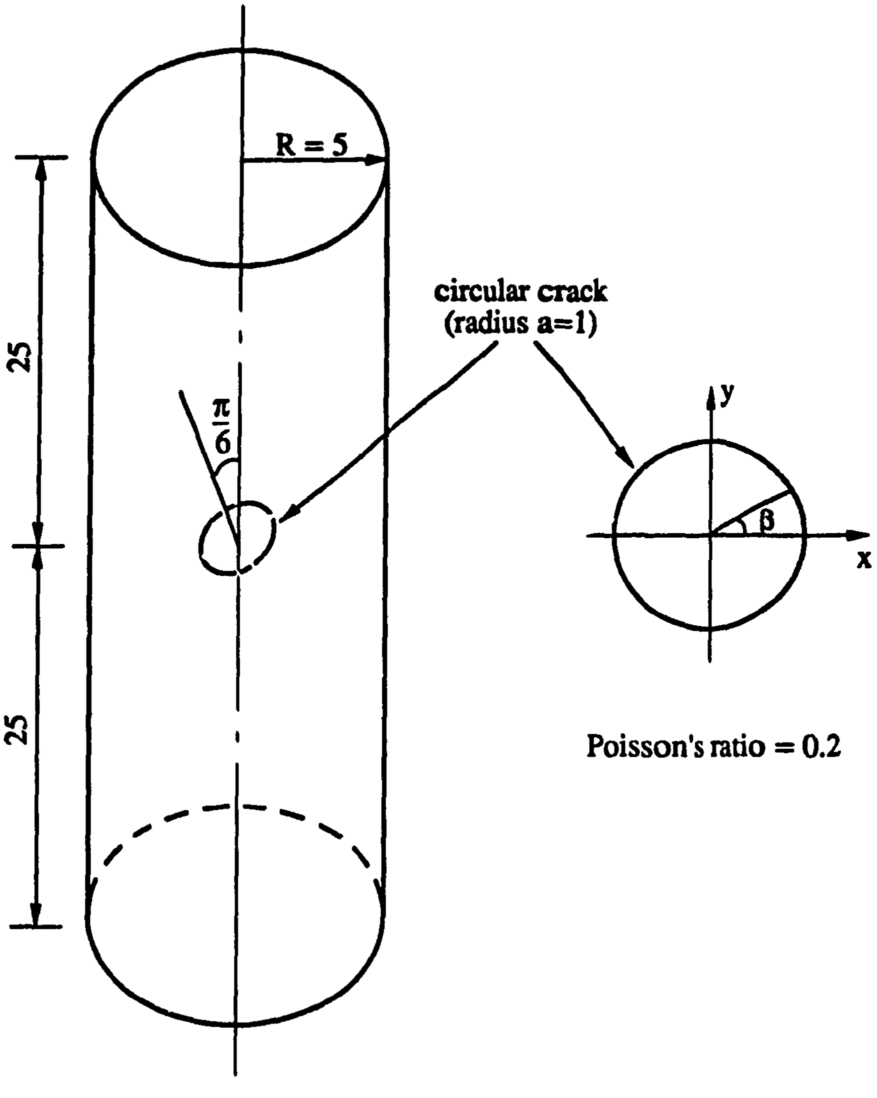

Figure 5.6 Cylinder with inclined circular crack

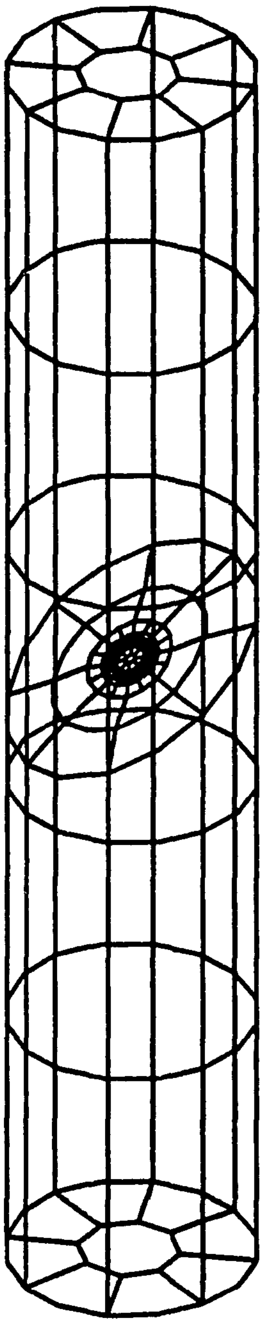

Figure 5.7 BE discretization of the cylinder with inclined circular crack

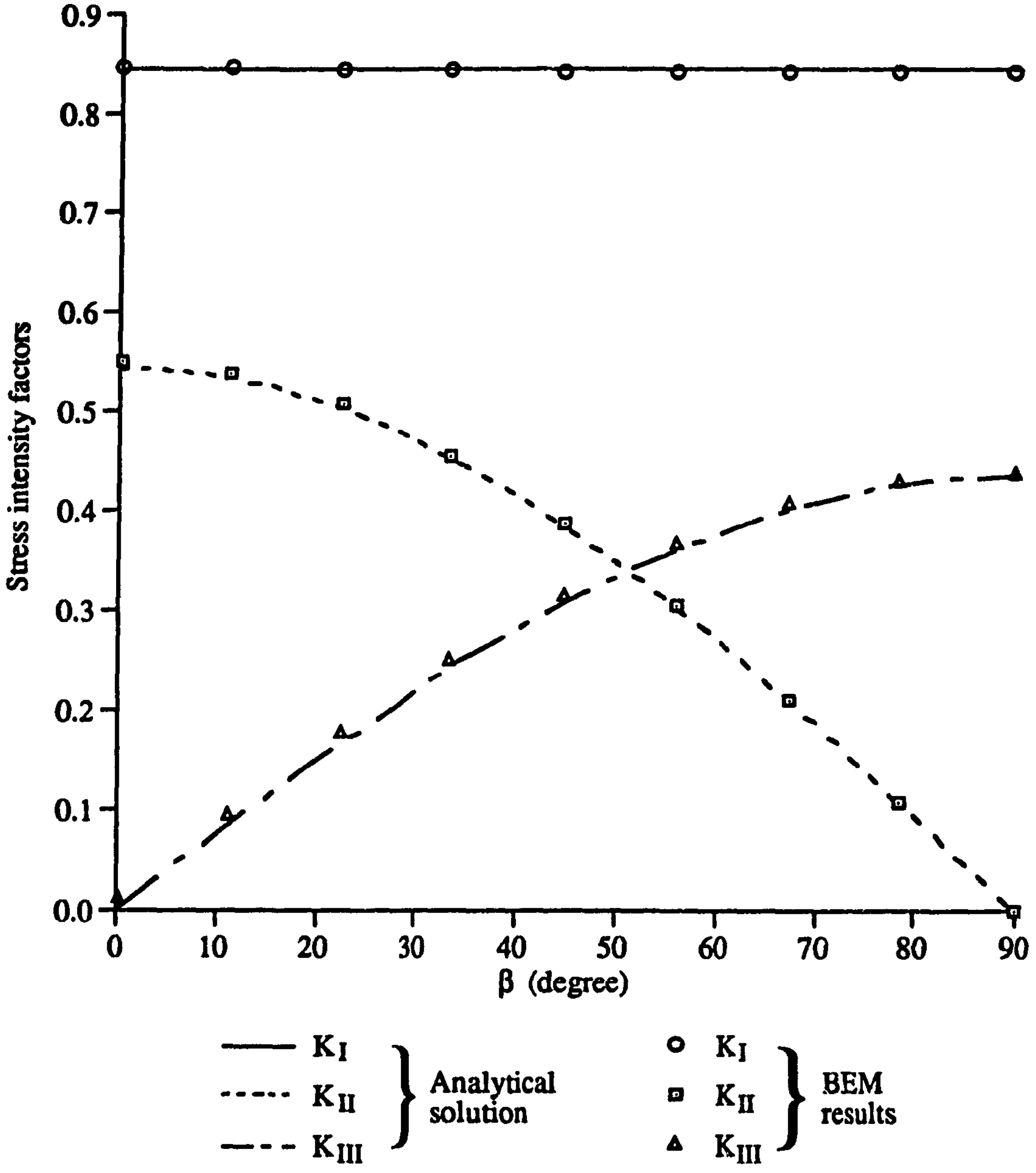

Figure 5.8 Stress intensity factors for inclined circular crack under unit uniform tension at far ends

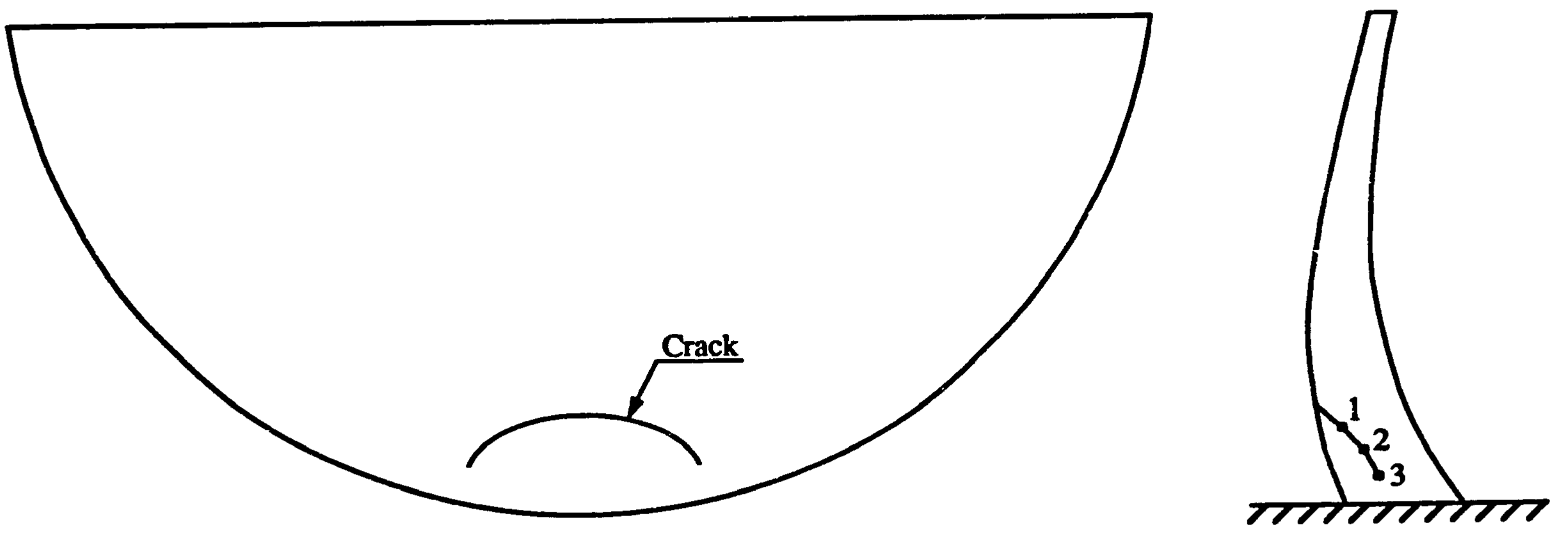

(a) Upstream view

(b) Crown cantilever

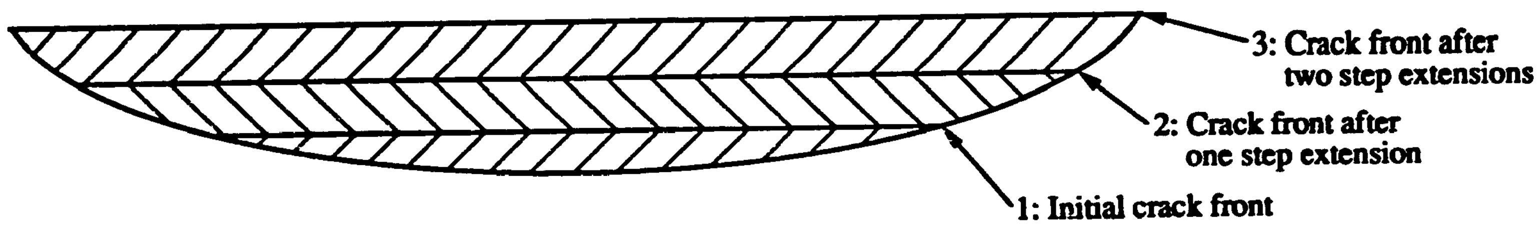

(c) Enlarged crack surface

Figure 5.9 Modelling crack propagation

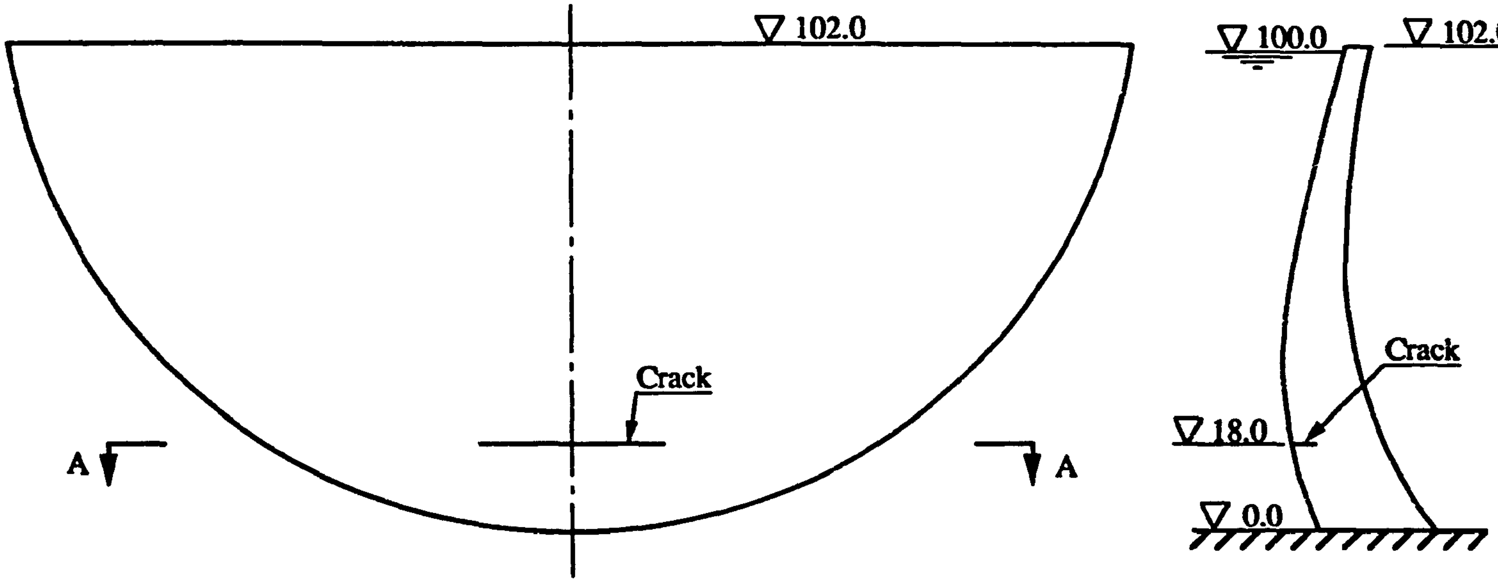

(a) Upstream view

(b) Crown cantilever

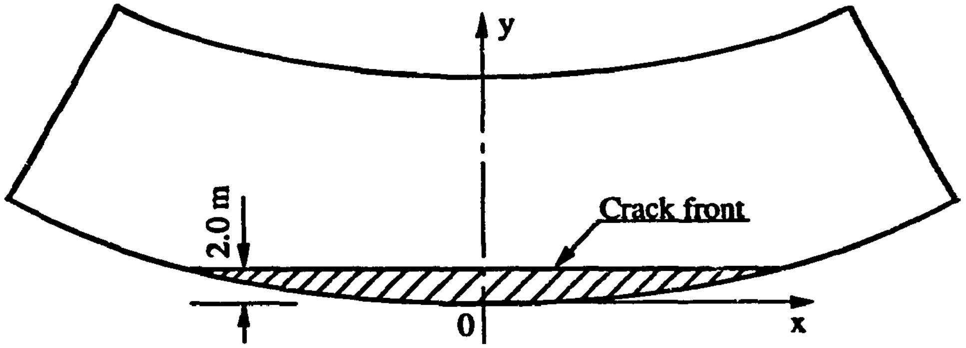

(c) Enlarged A-A section

Figure 5.10 Jinshui Tan arch dam

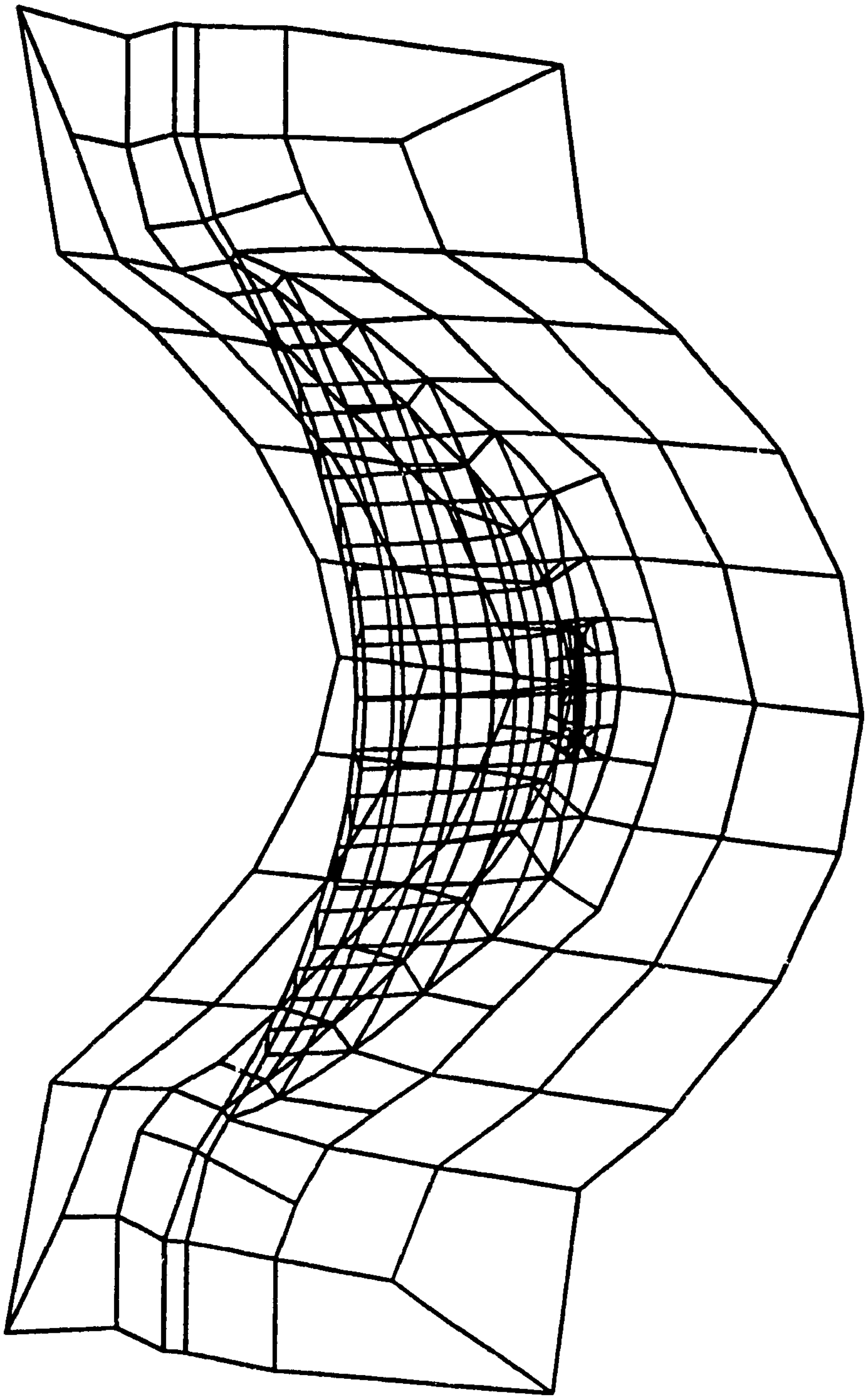

Figure 5.11 BE discretization of Jinshui Tan arch dam with a through crack near the dam base

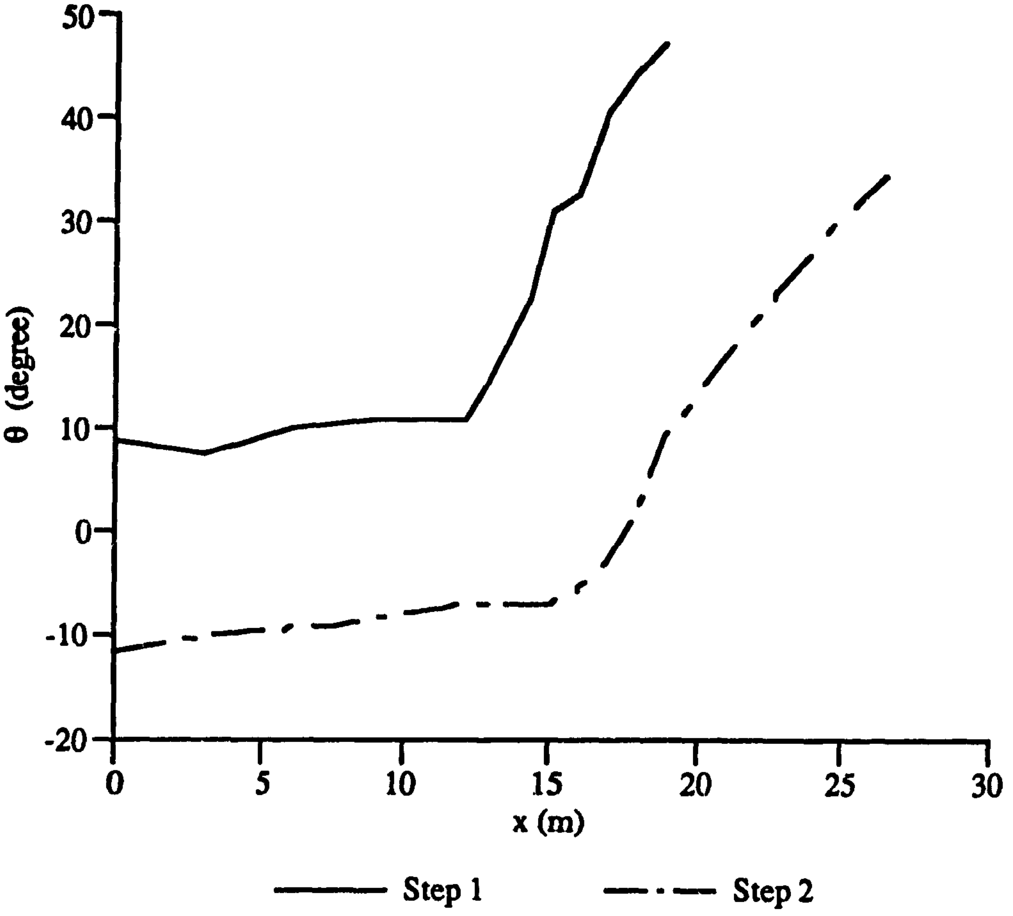

Figure 5.12 Variation of crack propagation angle θ along through-crack front

CHAPTER 6

CASE STUDY - CRACKING OF KOLNBREIN ARCH DAM

The general procedure for cracking analysis in arch dams proposed in Chapter 5 is now applied to the case study of the Kolnbrein arch dam in Austria. A detailed study of the first upstream cracking in this dam during the reservoir impounding stage is presented, based on three models for the possible causes of the observed damage.

6.1 PROTOTYPE BEHAVIOUR AND NUMERICAL SIMULATION

Observed cracking

The Kolnbrein dam in Austria is a 200 m high, double curvature arch structure situated in the Tauern Mountain range[21]. As shown in Figure 6.1, the dam is situated in a U-shaped valley with a canyon width/height ratio of 3.1 and bottom thickness/height ratio of 0.18. The right bank consists of massive gneisses and the left abutment of bedded gneisses with some intercalations of schistose gneisses. The construction of the dam was completed in 1977 and water began to be impounded in 1976.

During the first two partial fillings, beginning in 1976 and reaching a level of 1852 m in 1977 while construction was still under way, the dam and its foundation behaved in an expected manner, with nothing unusual about deformation of the dam, uplift at the base or drainage flow. However, during the reservoir filling in the autumn of 1978 when the water level exceeded 1860 m, the water leakage from drainage holes increased suddenly, surging to 200 l/s when reservoir elevation reached 1890 m. The uplift and joint water pressure at the dam base of the highest blocks soared to 100 % of the reservoir head at this time. After emptying and extensive exploration by core drilling, a steeply inclined cracking system was discovered, daylighting on the upstream face. This cracking system also penetrated the dam foundation, breaking the grout curtain as seen in Figure 6.1(b). Two horizontal downstream cracks near the dam base were also detected. These are believed to have been created at the end of the construction stage, due to vertical tensile stresses produced by self-weight of the dam and the grouting pressure in the construction joints, but which closed during the subsequent reservoir filling. Following two years during which various remedial work was undertaken, extremely large water leakage (more than 400 l/s in 1982 when reservoir level reached 1890 m) indicated the formation of the second upstream cracking shown in Figure 6.1(C). For more details concerning the behaviour of the Kolnbrein dam, readers may refer to the References [21], [69]-[73].

The unique pattern of the first upstream crack daylighting at an acute angle on the upstream face has previously been investigated in a 2-D finite element analysis by Linsbauer et al.[23], who employed four models to predict the initiation and trajectories of this crack. Due to the complexities of the problem, definitive conclusions were not reached. Thus, the simplified 3-D fracture model proposed herein is also applied to this crack as a case study.

Loadings

The three basic loads, namely hydrostatic, temperature and self-weight, are considered in the present analysis. The most important is the upstream hydrostatic pressure and the associated uplift acting on the crack surfaces. Since the increased leakage was first discovered in the autumn of 1978 when the reservoir elevation exceeded 1860 m, the upstream water level is assumed to be in the range 1850–1860 m. Temperature loading is based on the following considerations: (i) Water temperature variation along the upstream face; (ii) Air temperature change on the downstream side based on the local dam site record shown in Figure 6.2(b); and (iii) The thickness of the cross sections at different elevations. A refined procedure[74] taking these factors into account is employed to obtain the induced thermal stresses (see Appendix II for details). Rigorously, the stresses caused by the self-weight of the dam are related to construction procedure and the grouting process of the contraction joints. Herein, a global self-weight stress field is adopted for simplicity, i.e. the self-weight loading is resisted by arch and cantilever actions of the dam in the same manner as is the hydrostatic load.

Assumed crack models

Considering the possible locations of crack initiation and the question of bonding between the dam and the elevated foundation on the upstream side, the three crack models shown in Figure 6.3 are studied. The first two are based on cracks initiating at, and propagating upward from, the interior point of the detected damage, namely point C on the dam base. In the third model, the crack is assumed to propagate downward from corner point A, where stress concentration may have been the cause of crack initiation. Perfect bond condition between the dam and foundation interface AB is assumed in crack models 1 and 3, while the model 2 is bond-free. The crack initiating on the dam base of models 1 and 2 could have resulted from the high concrete temperature of 29°C reached during construction[21], compared to the stable concrete temperature of approximately 5°C. This 24°C difference, together with the restraint provided by the foundation rock, may have produced tensile stresses in the concrete above the foundation sufficient to create minor cracks at the dam base. Secondly, nonuniform foundation deformation caused by difference in geological conditions of the rock could also have resulted in small cracks in the concrete at the base. Alternate explanations for possible causes of a crack propagating upward from the base have been presented by Linsbauer et al.[23].

Analysis of crack extension

The crack trajectories are computed by the aforementioned program FAPAD for the three crack models under appropriate range of the reservoir water level (WL). The BE discretization of the dam and foundation rock for crack model 1 is shown in Figure 6.4. The mesh around the initial crack at the dam base is refined and infinite boundary elements are employed to model the remote regions of the foundation. The cracking region of the dam and base needs to be remeshed to accommodate the new crack front after each step of crack extension. The CPU time for each step of crack extension requires approximately 7 hours on a IBM PC 486/50 computer.

The properties of the concrete and rock material adopted in this study are listed in Table 6.1 and cited from Linsbauer et al.[22]. As noted in Reference [22], fracture toughness K_{IC} is difficult to determine and the typical value 2.0 MPa·m$^{1/2}$ is assumed for the Kolnbrein concrete. The corresponding critical strain energy density factor S_{cr} is given by: $S_{cr} = K_{IC}^2 (1+v)(1-2v)/(2E) = 0.08$ kN/m.

6.2 RESULTS FOR FIRST UPSTREAM CRACKING

Crack model 1

Since the first upstream cracking was not detected until the water level reached 1860 m, WL=1850, 1855, 1860 m is employed as a parameter. During the reservoir filling in 1978, an upstream tension zone (Figure 6.5) may have developed in the foundation rock at the heel of the dam[71], causing opening of rock joints in this area which allowed the water in the reservoir to permeate to the grout curtain and build up the full water pressure. Since the observed crack is located near the region of the grout curtain, it is assumed that this pressure acts also on the crack surfaces of this model. Since Figure 6.2(b) shows that WL=1850-1860 m is accompanied by close to peak temperature, loading corresponding to this temperature is also imposed on the dam. A small initial crack inclined at 45 degrees is assumed at the base.

The trajectories in the highest cantilever section obtained by numerical analysis for crack model 1 are compared in Figure 6.6 with the observed cracking of the dam. This comparison of the crack profiles leads to the following conclusions: (i) The computed crack profile is sensitive to the reservoir water level; it is seen that a 10 m difference in WL results in an 8 m difference in elevation where the crack penetrates the upstream surface; the higher the water level, the lower the point where the crack reaches the upstream surface; and (ii) When the water level is somewhere between 1850-1855 m, the computed crack trajectory is predicted to daylight at the corner point elevation of 1720 m, which is close to the actual location of the crack mouth.

The three-dimensional crack surface for the case of Figure 6.6(a) is shown in Figure 6.7(b) and its corresponding trace on the upstream face of the dam is compared with the observed pattern of cracking in Figure 6.7(a). Good agreement of the lateral extent of the crack trace on the upstream face is evident in Figure 6.7(a), further confirming the adequacy of the through-crack assumption in modelling 3-D crack extension in arch dams.

To evaluate post-cracking safety, the stress redistribution in the dam following crack propagation was also studied. The stress distributions along the crown cantilever, top and elevation 1750 m arch sections corresponding to Figure 6.6(a) were compared at the first and final steps of crack propagation in Figure 6.8. As expected, tension stress in and around the upstream cracked region of the dam is released once the crack has approached the upstream face. Since the redistribution becomes negligible above elevation 1750 m, the effect on the entire structure of such relatively shallow cracking (approximately one-quarter the dam width at the base) is limited and overall safety of the dam is not impaired.

To examine the proportion contributed to the stress intensity factors by each of the load components, K_I and K_{II} computed separately for each component are plotted in Figure 6.9 for the case of Figure 6.6(a) (K_{III} is not reported since it is very small and has no influence on crack propagation angle θ for a through-crack). The data indicate that: (i) The reservoir water plays the most important role with the temperature load the least; and (ii) The contributions to K_{II} made by water pressure and self-weight predominate but nearly offset each other, resulting in K_{II} caused by temperature to be close to that of the total loading. Since the magnitude of the resultant K_{II} remains small regardless of the crack length, the direction of the crack extensions changes very little during the propagation process.

Although the temperature load apparently plays only a minor role, it nevertheless does influence the crack profile developed. The results of crack propagation analysis excluding the temperature load, performed for WL=1860, 1865 and 1870 m as shown in Figure 6.10, indicate that temperature affects the propagation direction of the crack initiated on the dam base in such a way that the crack reaches the upstream face at a lowered elevation. Comparison of the crack profiles in Figure 6.10 with those of Figure 6.6 leads to the conclusion that including temperature is equivalent to the effect of an upward shift by 10 m in the reservoir water level. For example, without temperature load the computed crack path will daylight near the corner point when the reservoir elevation is close to 1865 m, with a corresponding crack profile [Figure 6.10(b)] very similar to that of Figure 6.6(b) for WL=1855 m.

The minimum strain energy density factors S_{min} for each step of crack extension corresponding to Figures 6.6 and 6.10 are plotted in Figure 6.11 from which it is seen that the general trend of S_{min} becomes larger as the crack propagates forward, and the higher of the reservoir level, the larger of the S_{min}.

In order to study the effect of uplift pressure on the stability of the assumed initial crack, analysis was performed for the initial crack without uplift pressure on the crack surfaces. Under WL=1860 m and with temperature load included: $K_I = 0.16$ MPa·m$^{1/2}$; $K_{II} = 0.064$ MPa·m$^{1/2}$; and $S_{min} = 0.011$ kN/m. Since S_{min} is much smaller than S_{cr}, without uplift on its surfaces the initial crack is stable and therefore will not propagate. Thus, uplift pressure in the crack plays a key role in affecting the stability of a crack propagating from the dam base.

Crack model 2

As noted earlier, unlike model 1 this model assumes no bond along the interface between the dam and the foundation on the upstream face from A to B [Figure 6.3(b)]. The crack profiles under the loads of reservoir water, self-weight and temperature variation for WL=1850 and 1860 m, with and without uplift pressure in the crack, are shown in Figure 6.12 and the corresponding S_{min} in Figure 6.13. It is seen that: (i) The orientation of the crack changes sharply toward horizontal daylighting on the upstream face at a much lower elevation (approximately 1709 m) than obtained previously for crack model 1. Such a nearly horizontal trajectory is a common pattern in concrete dams generally, but is inconsistent with the steeply inclined one observed in the Kolnbrein dam; (ii) The uplift pressure in the crack has little effect on the shape of the crack profile although it does increase the values of S_{min} substantially as evident in Figure 6.13. The explanation for such trajectories daylighting horizontally at the upstream face is that the direction of the tensile principal stress is almost vertical near the upstream face. Since this pattern of cracking is obviously not similar to the observed one, crack model 2 can safely be discarded as applicable to the first upstream cracking in the Kolnbrein dam.

Crack model 3

As is the case in model 1, this model is also based on assuming a small initial crack, steeply inclined as the observed one but now originating at the upstream corner point A as previously discussed and shown in Figure 6.3(c). Full water pressure acts on the crack surfaces, because the crack is connected directly to the reservoir. Interface AB is assumed to possess perfect bond. The computed crack profiles are shown in Figure 6.14 for WL=1850 and 1860 m, with and without temperature load. The corresponding values of S_{min} are illustrated in Figure 6.15. Raising of the reservoir level by 10 m and including temperature are seen to cause the crack trajectory to propagate downward less steeply in this crack model.

Although the computed crack profile in Figure 6.14 for WL=1850 m is quite close to the observed one, the magnitude of S_{min} corresponding to the initial crack is very much greater than material property S_{cr} (Figure 6.15) of the concrete. This implies that the crack in this model would have propagated at a much lower water level than 1850 m, which is contradicted by the field experience wherein, during the second filling of the reservoir in 1977, the highest water level reached 1852 m [Figure 6.2(a)] evidently without cracking. On the other hand, this model would be the applicable one if the tensile stress at the upstream corner point was smaller than the tensile strength of the concrete itself, thus precluding the existence of an initial crack before the reservoir water reached 1850 m. It is also interesting to note from Figure 6.15 that S_{min} decreases as the crack extends downward, which differs from the 2-D finite element results of Linsbauer et al.[23], who obtained a monotonic increase of K_I as the crack develops downward. This difference is attributable to the lateral restraint provided by canyon to the dam, which becomes larger as the crack approaches the base of the dam and which is included in the present 3-D analysis, while a 2-D model cannot consider this effect.

6.3 ASSESSMENT OF PERFORMANCE OF CRACK MODELS

Comparing the predicted crack trajectories with the observed one, the most probable model for the actual cracking of the Kolnbrein dam is represented by the model 1, i.e. the crack initiated on the dam base and propagated steeply upward, daylighting on the upstream face under reservoir elevation 1850-1855 m (with temperature load) or 1860-1865 m (without temperature load). In this modelling of the prototype damage, small cracks existed inside the concrete at the dam base, and a tensional region developed in the heel region and opened the joints of the rock in this region, causing full uplift pressure to act on the crack surfaces. The upstream interface between the dam and elevated foundation is needed to be well bonded. Under these conditions, the distinctive pattern of the first upstream crack which occurred in the Kolnbrein arch dam is predicted quite accurately. It is found that the daylighting elevation of this crack is rather sensitive to the reservoir water level. It is also worth noting that the existence of the uplift pressure along the crack surfaces plays a key role in causing the pre-existing crack to propagate, especially in the early stage of crack development. The well-bonded condition assumed for the upstream interface between the dam and the elevated foundation is necessary to explain the acute angle of crack profile. Otherwise, the crack would have followed a much flatter trajectory and daylighted at considerably lower elevation on the upstream face, as associated with model 2.

The plots of S_{min} versus crack growth, shown in Figures 11, 13 and 15 for crack model 1, 2 and 3, respectively, confirm that the initial crack of model 1 becomes unstable at water level consistent with the prototype behaviour. Crack model 2, already inconsistent in terms of the crack trajectory, is also seen to require a much lower reservoir level than the field experience in order to induce initial crack instability; this bond-free model has therefore been precluded.

Model 3, wherein the crack may have initiated at the upstream face at, or near, the corner of the dam-elevated foundation interface due to stress concentration, also predicts steeply inclined and downward propagation of the initial crack of this model. The well-bonded condition on the upstream interface needs to be assumed. Under these conditions, a crack profile similar to that of model 1 and in similar accordance with the prototype observation is obtained. Compared to the model 1, however, the major difference is that strain energy density factor S_{min} obtained with this model (Figure 6.15) is much greater than the magnitude of S_{cr} of the concrete, especially at the early stage of crack development. This means that no initial crack existed until the reservoir impounding reached elevation around 1850 m, otherwise the crack would have propagated much earlier than it really happened. Also, the upstream interface should be well-bonded, otherwise it is almost impossible to develop such an acute angle of crack profile.

Comment on the second upstream crack

The analysis of the second upstream cracking needs more information such as boundary and geometrical conditions of the first cracking, especially its lateral extension and the effectiveness of the various remedial treatments between 1979 and 1983. All these conditions have effects on the development of the second cracking. Since this information is not available at present, it requires further investigation in the future.

6.4 CONCLUDING REMARKS

Applying the simplified BE procedure for 3-D static crack propagation in arch dams proposed in Chapter 5, the first upstream cracking occurred in the Kolnbrein arch dam has been analyzed in detail under various conditions concerning the foundation interface, location of crack initiation, reservoir water elevation and load combinations. The good agreement between the computed results and the field observations in the aspects of crack trajectory and crack trace on the upstream face confirms the applicability of the present procedure in predicting 3-D crack propagation in arch dams under static loading.

The advantages of the 3-D procedure proposed here, as well as of the one based on different assumptions proposed previously by Martha et al.[24], over the 2-D method employed by Linsbauer et al.[22], [23] include the capability of considering the redistribution of the external loads between the horizontal arch and vertical cantilever actions of arch dams, resulting in more accurate stress fields during the crack propagation process. In addition, the lateral extent of the cracking can be prescribed according to the geometrical shape of the 3-D structure or to the topography of the structure-foundation interface, while in a 2-D model an infinite extent in the lateral direction must be assumed, which normally would overestimate the cracking in 3-D structures.

Table 6.1 Material properties of Kolnbrein arch dam

Property / Material	Elastic modulus (MPa)	Poisson ratio	Specific weight (kN/m^3)	Thermal expansion coefficient (1/°C)
Dam concrete	18, 000	0.2	23.5	0.00001
Foundation rock	23, 000	0.2	—	0.00001

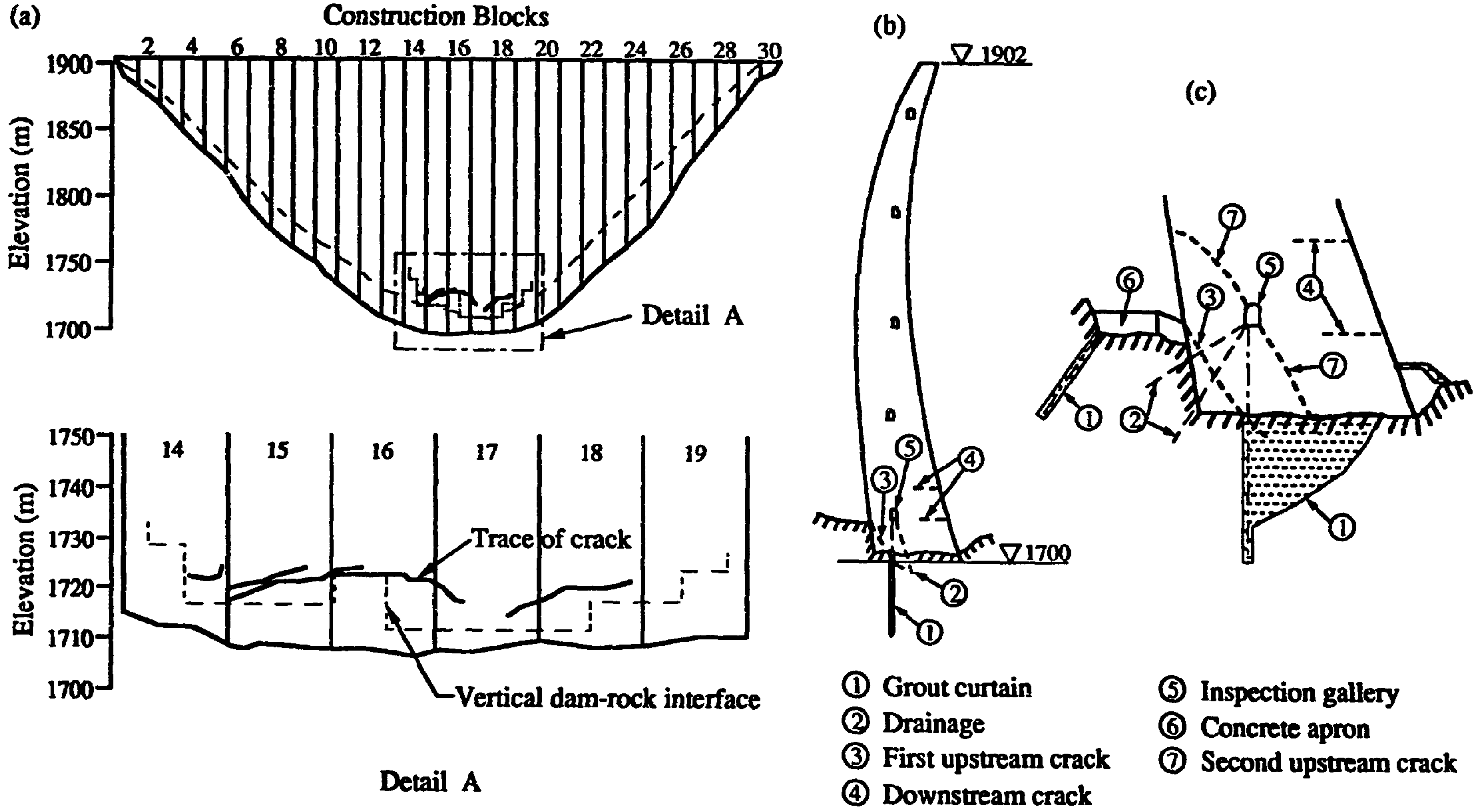

Figure 6.1 Cracking systems in Kolnbrein dam: (a) Upstream view, after Ref. 10; (b) Cross section and cracking situation in 1978; (c) Cross section near foundation and cracking situation in 1983, after Ref.20

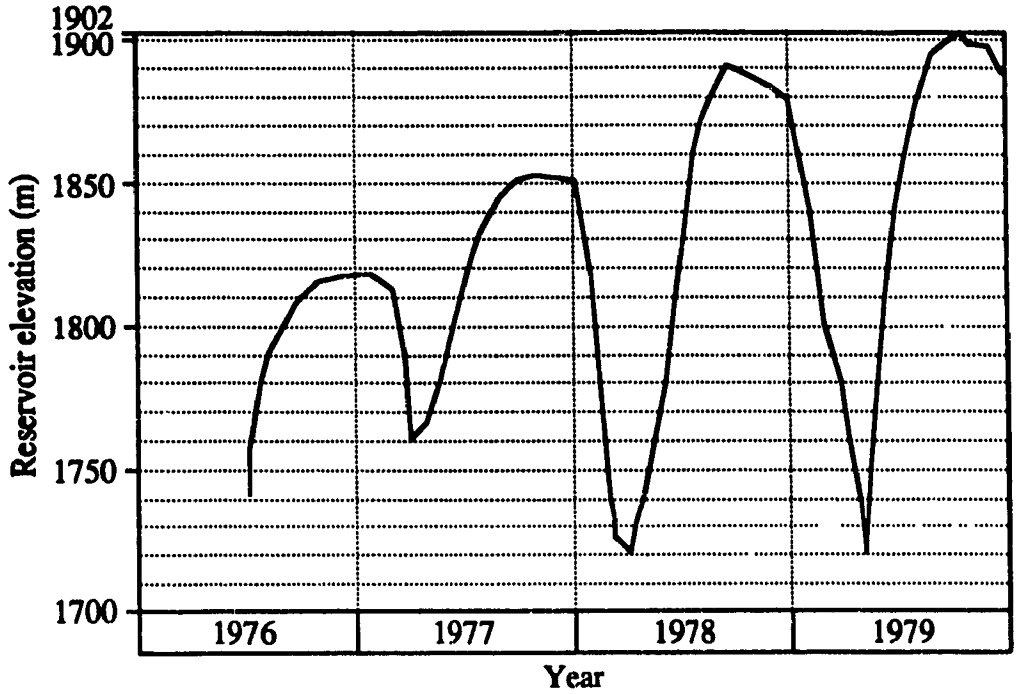

(a) Time history of reservoir elevation from 1976 to 1979, after Ref. 73

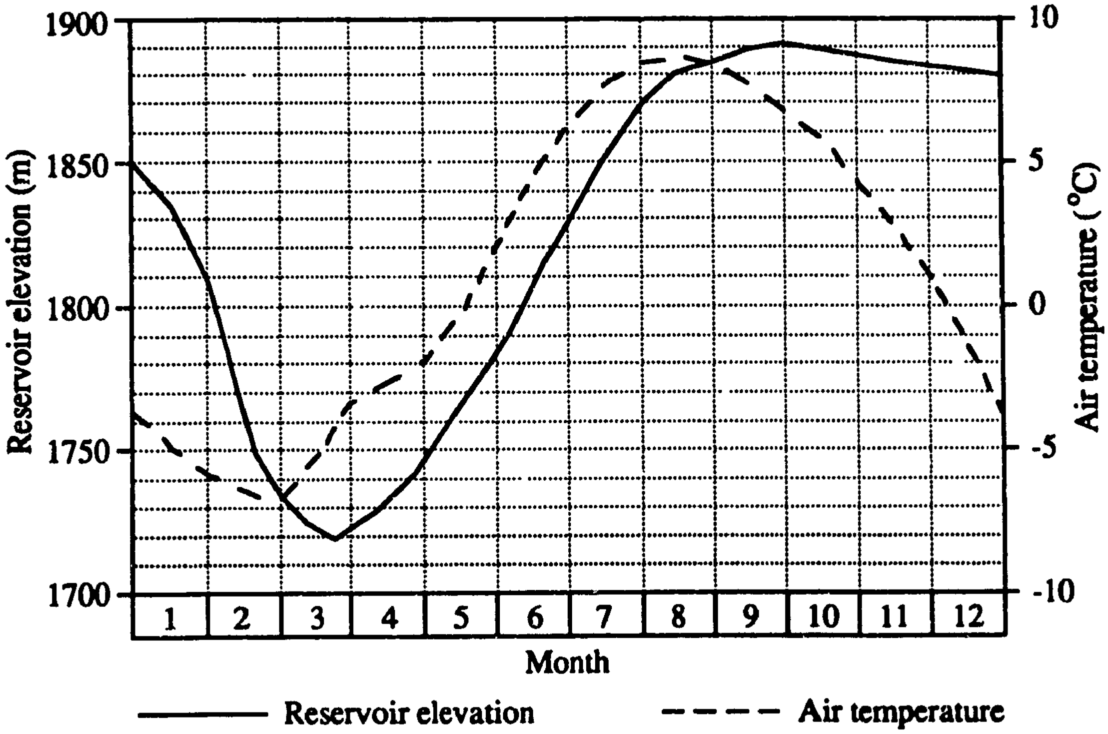

(b) Time history of reservoir elevation and air temperature in 1978

Figure 6.2 Time histories of reservoir elevation and air temperature at Kolnbrein dam

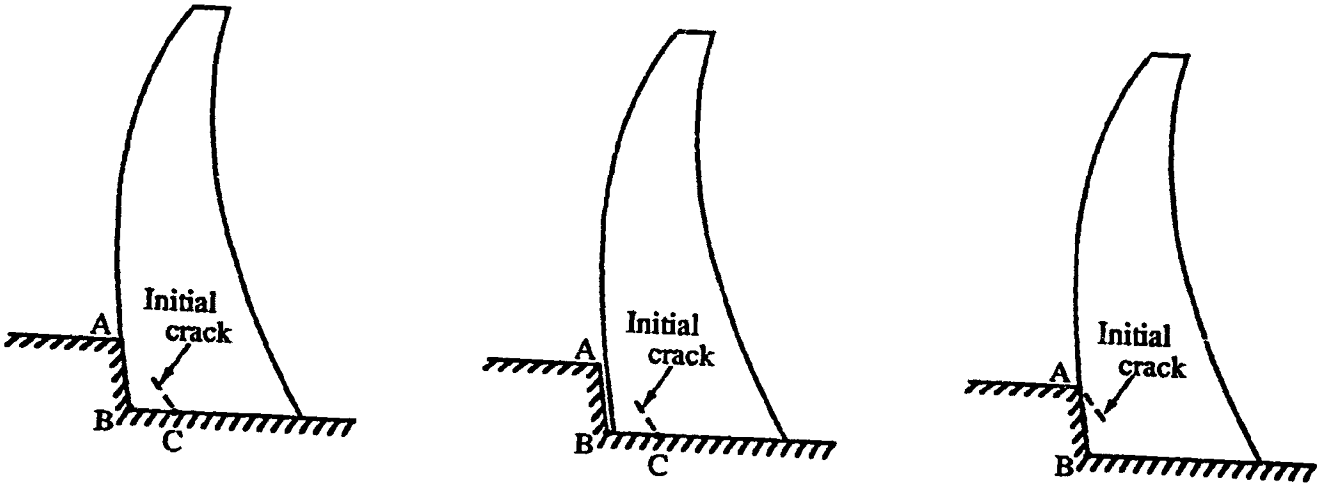

(a) Crack model 1

(b) Crack model 2

(c) Crack model 3

Figure 6.3 Crack models assumed in the analysis

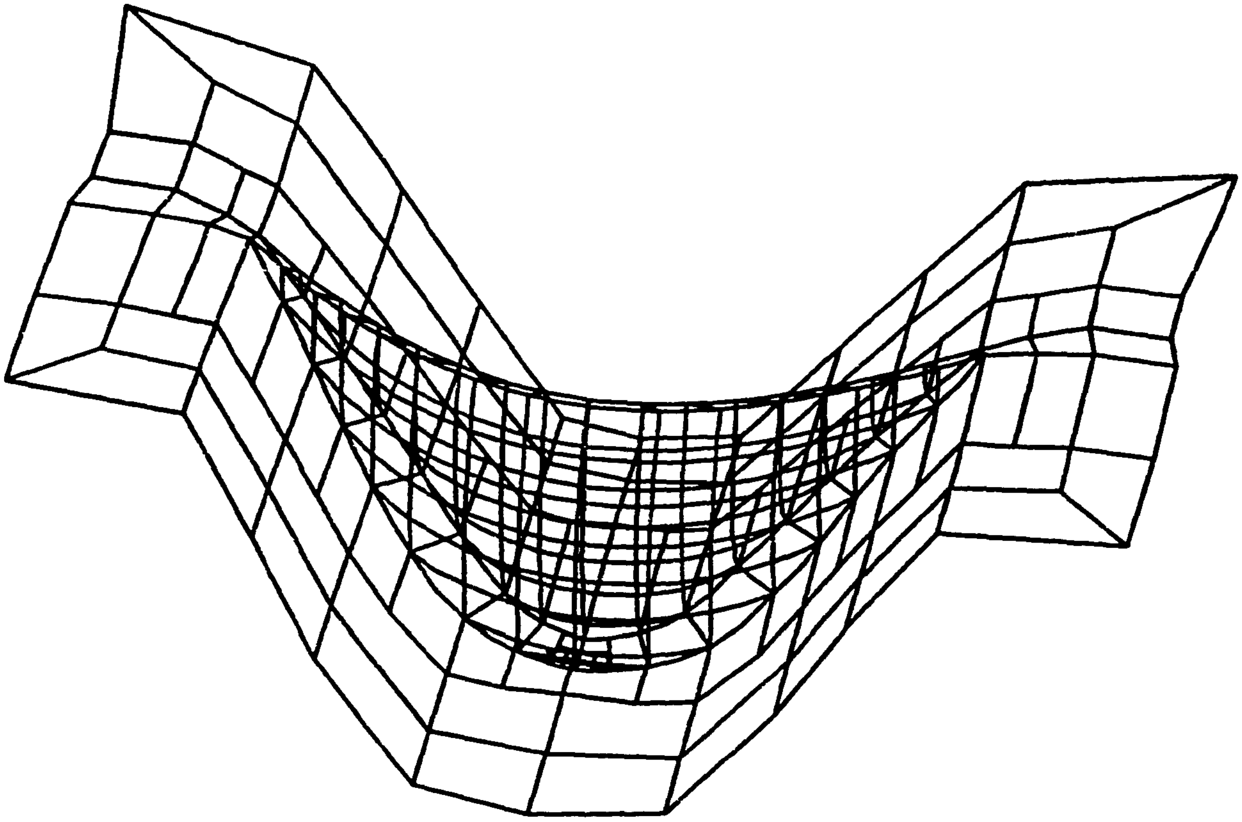

Figure 6.4 BE discretization of Kolnbrein arch dam for first upstream cracking

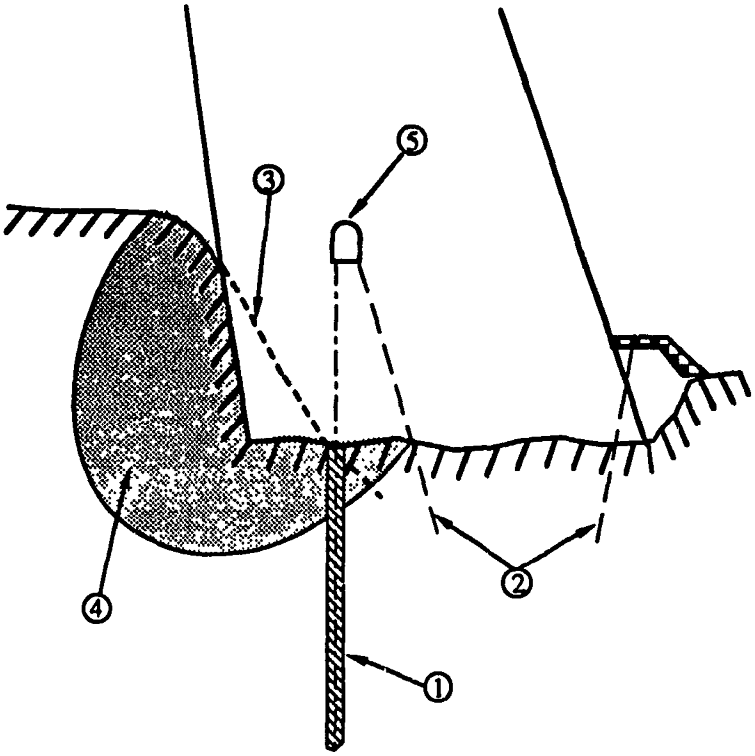

① Grout curtain
② Drainage
③ First upstream crack
④ Tension zone
⑤ Inspection gallery

Figure 6.5 Details near the base of Kolnbrein dam in 1978

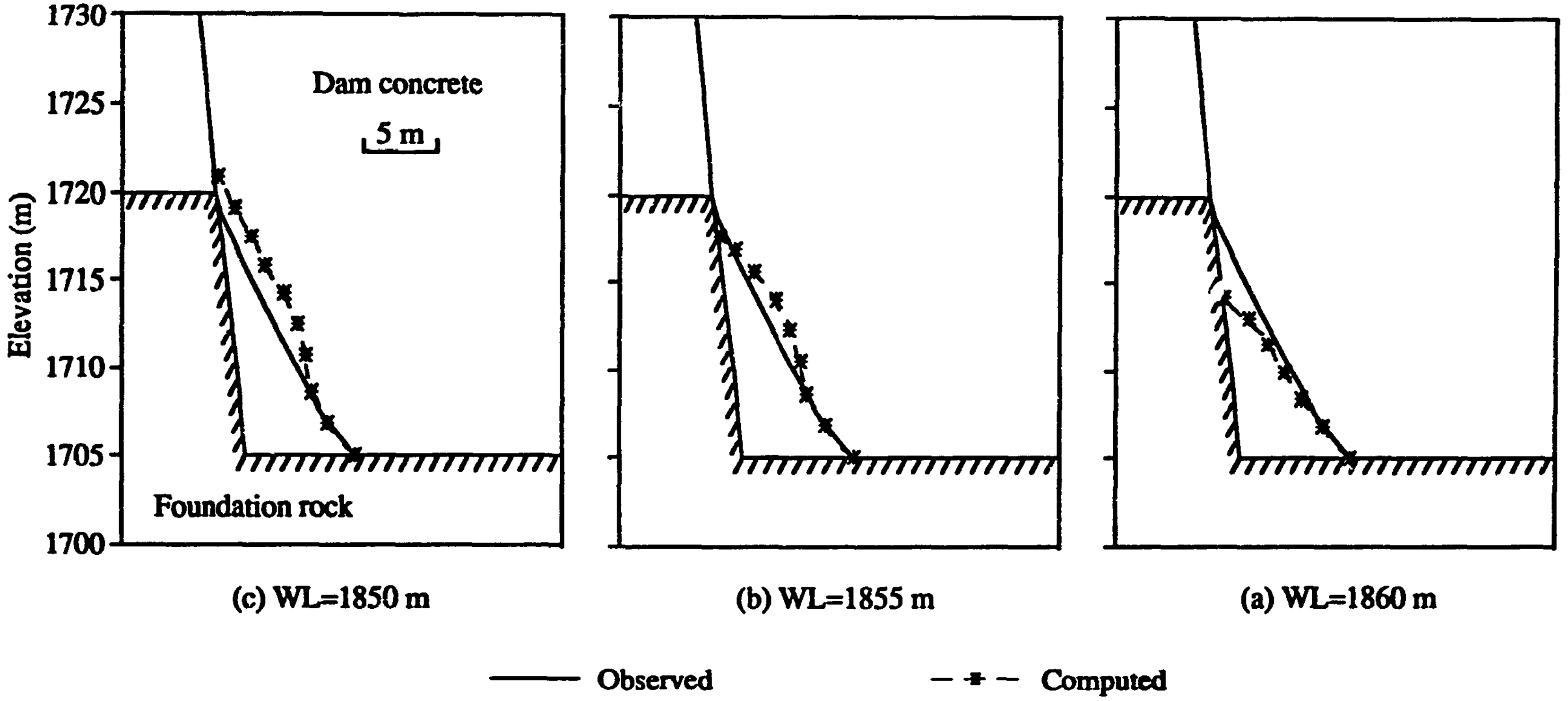

Figure 6.6 Crack profiles of model 1 under the loadings of reservoir water, self-weight and temperature for different water levels

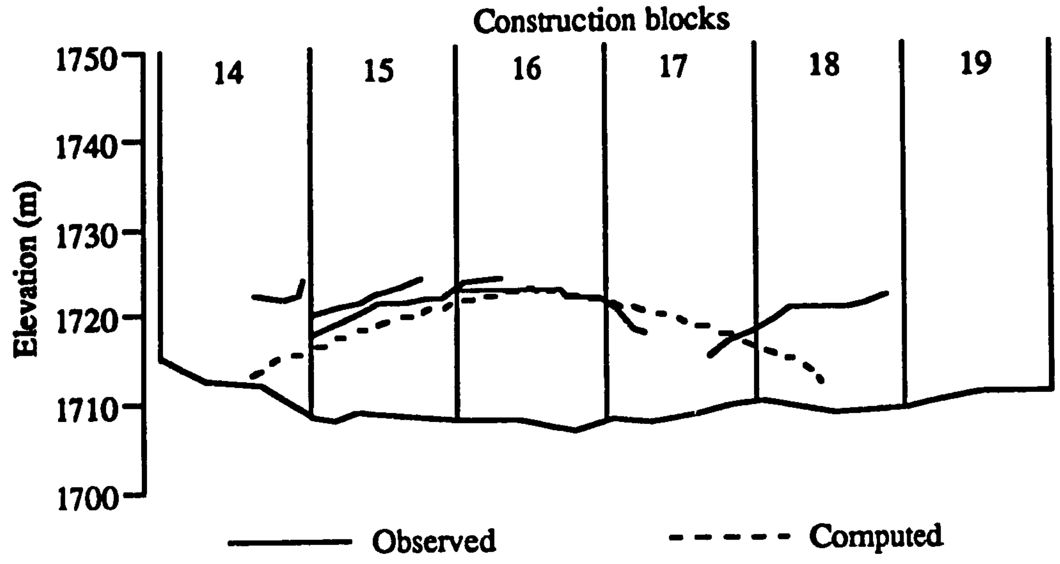

(a) Comparison of crack traces on upstream face

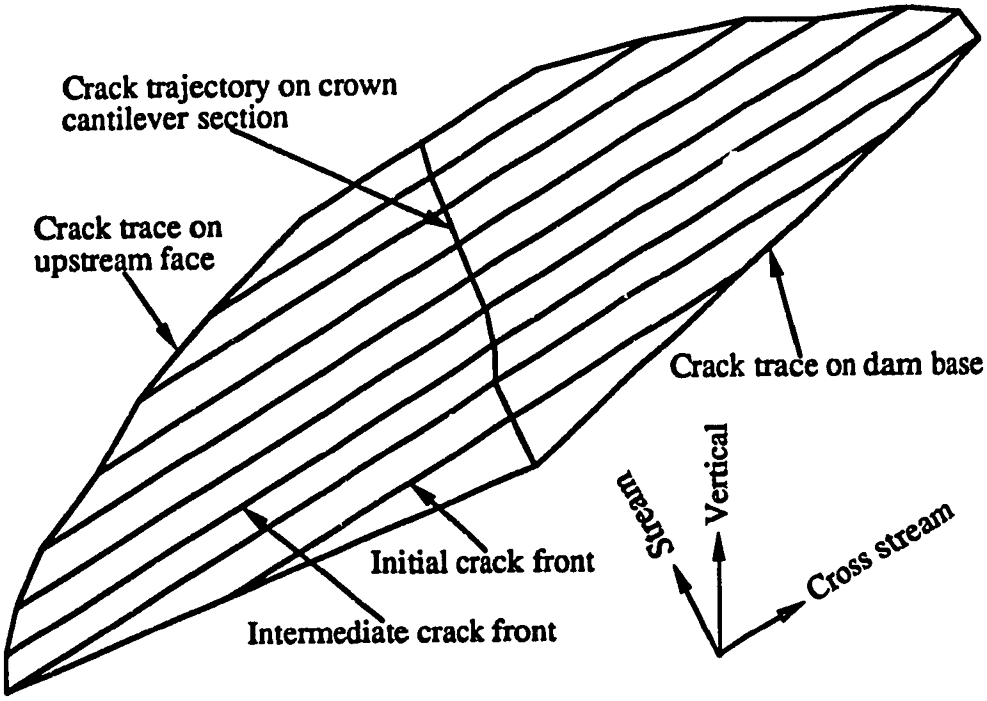

(b) Three-dimensional crack surface

Figure 6.7 Crack trace and surface for crack model 1 and WL=1850 m

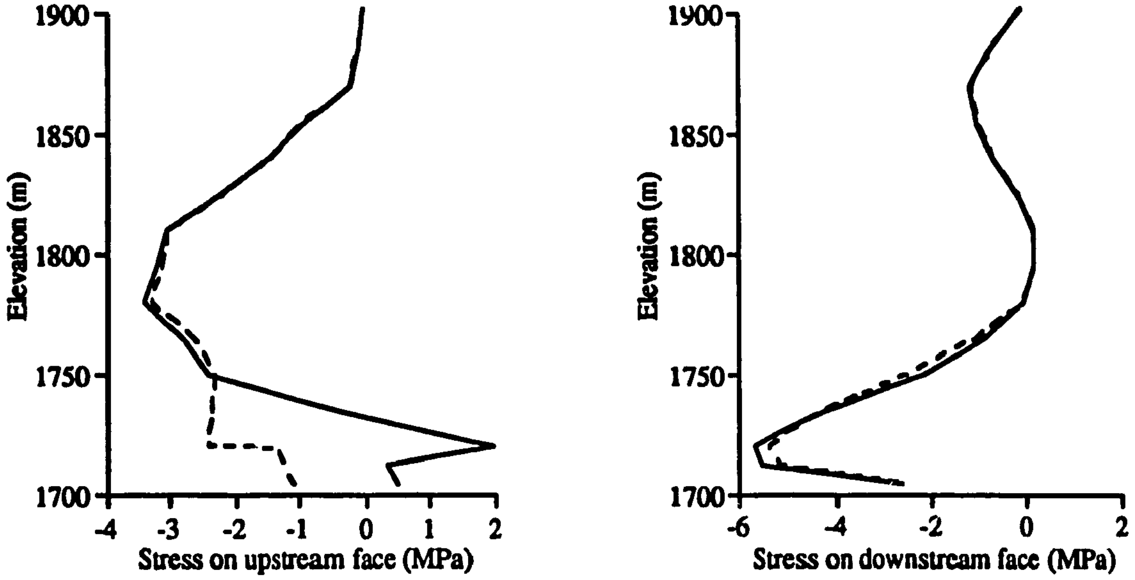

(a) Stress distribution in vertical direction of crown cantilever

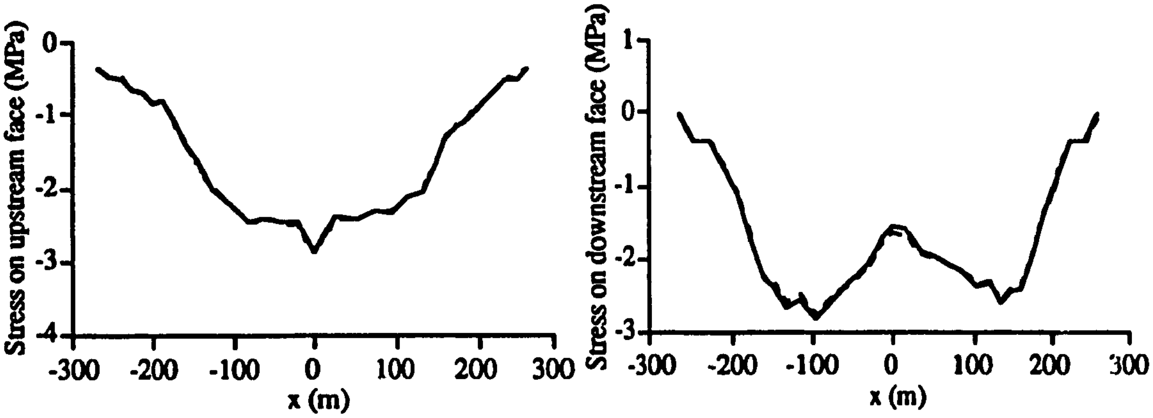

(b) Stress distribution in cross stream direction of top arch 1902 m

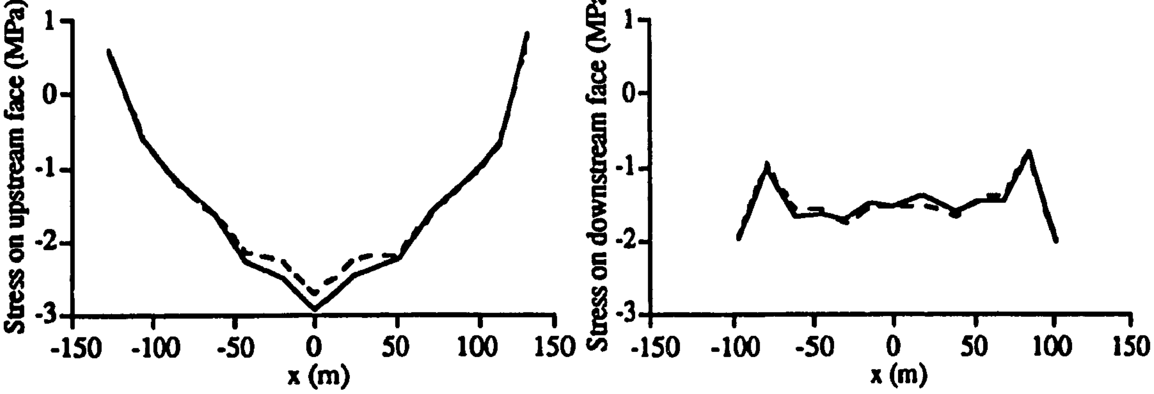

(c) Stress distribution in cross stream direction of arch section 1750 m

——— Initial crack ---- Final step of crack extension

Figure 6.8 Comparison of stress distributions

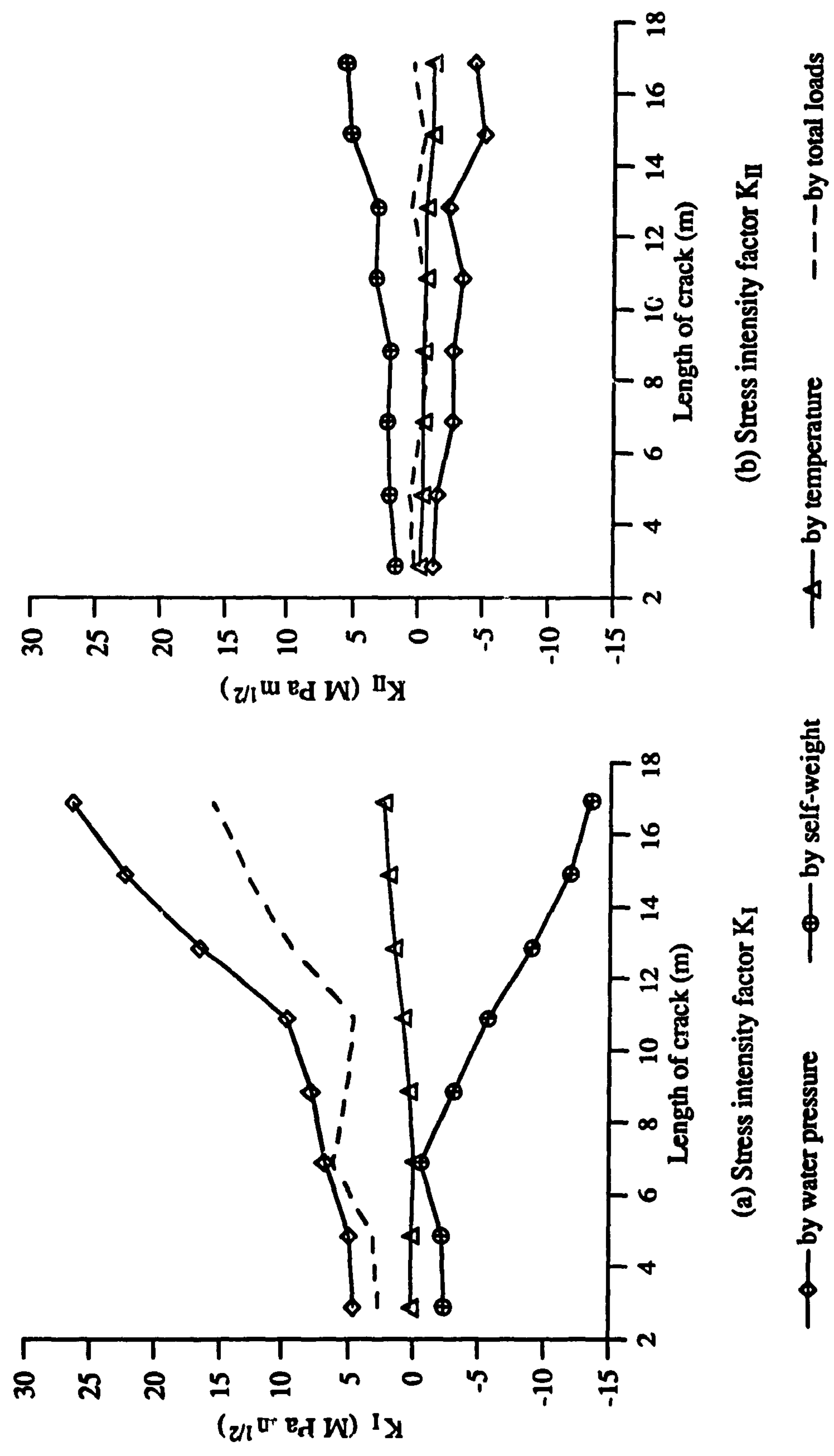

(a) Stress intensity factor K_I

(b) Stress intensity factor K_{II}

Figure 6.9 Comparison of crack model 1 stress intensity factors for different load components

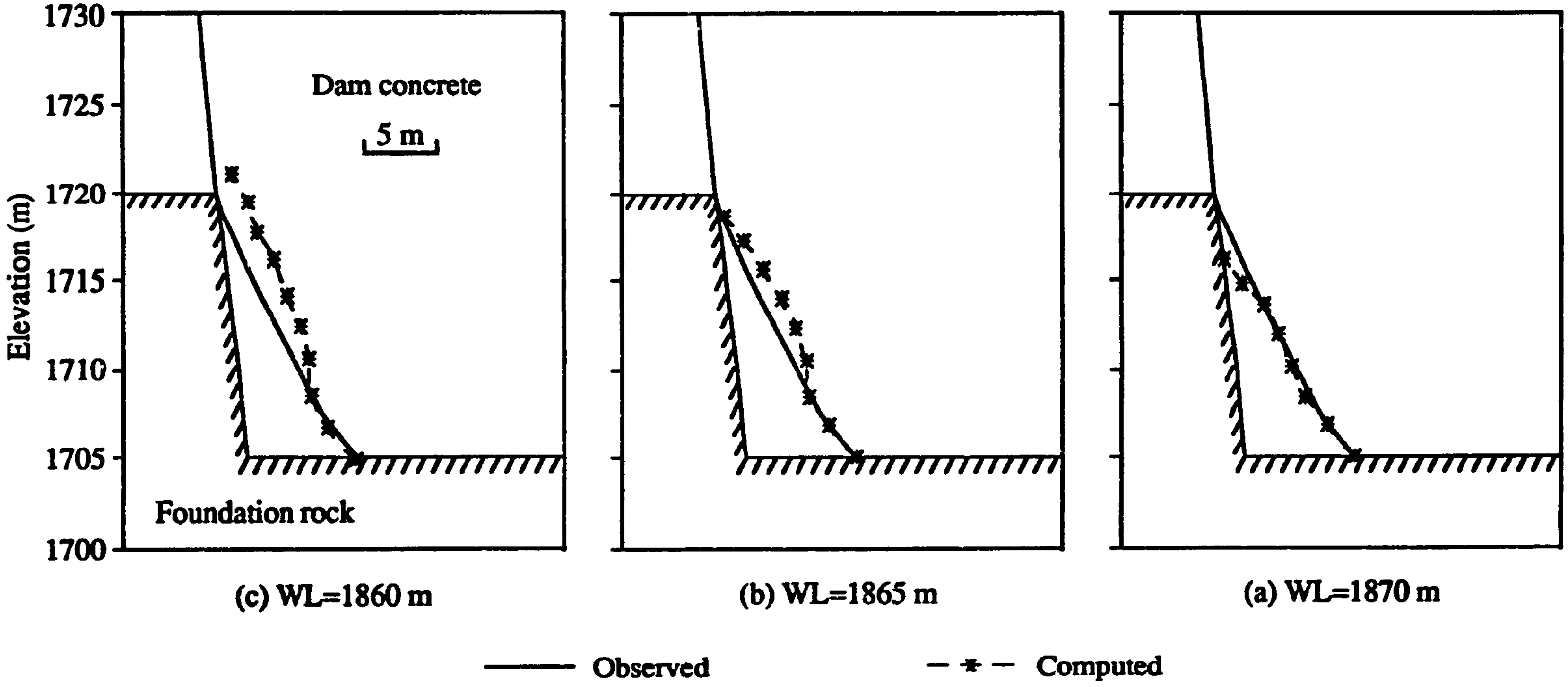

(c) WL=1860 m

(b) WL=1865 m

(a) WL=1870 m

Figure 6.10 Crack profiles of model 1 under the loadings of reservoir water and self-weight for different water levels

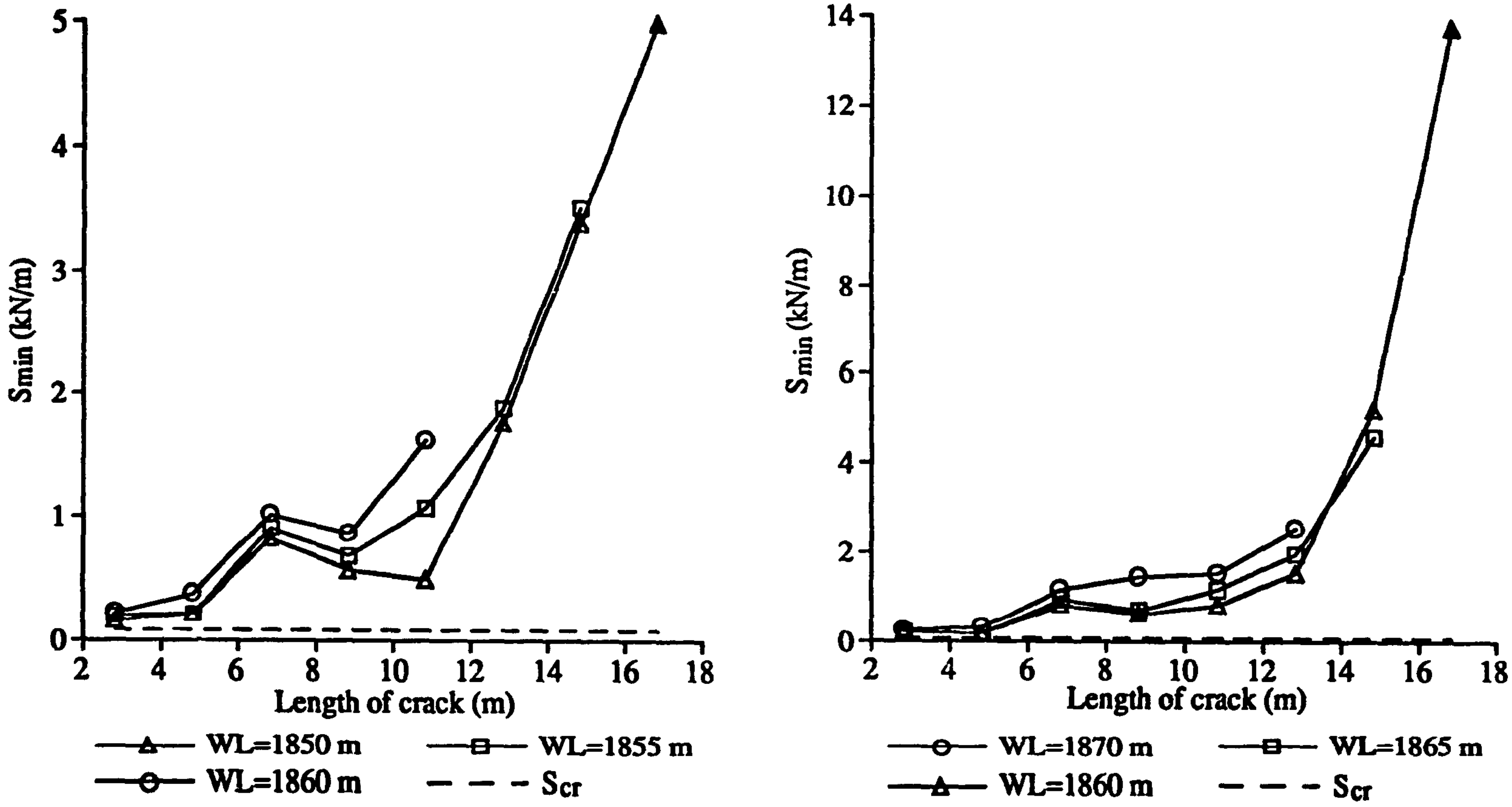

(a) Under the loadings of reservoir water, self-weight and temperature

(b) Under the loadings of reservoir water and self-weight

Figure 6.11 Minimum strain energy density factors of crack model 1 for different water levels

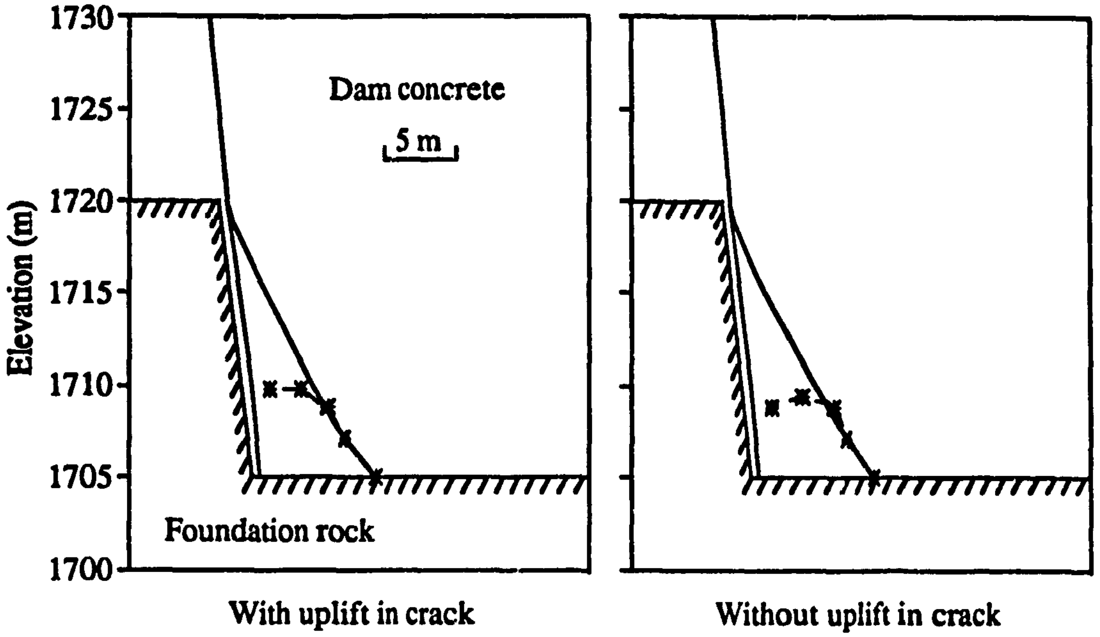

(a) WL=1850 m

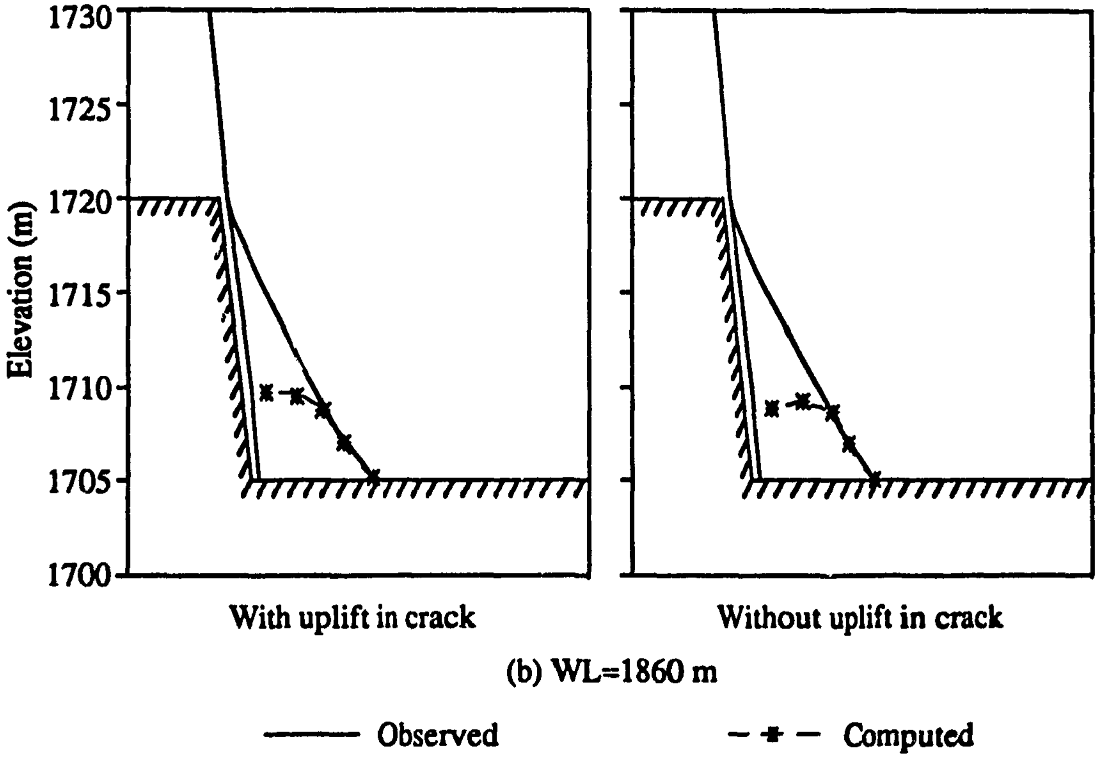

(b) WL=1860 m

Figure 6.12 Crack profiles of model 2 under the loadings of reservoir water, self-weight and temperature

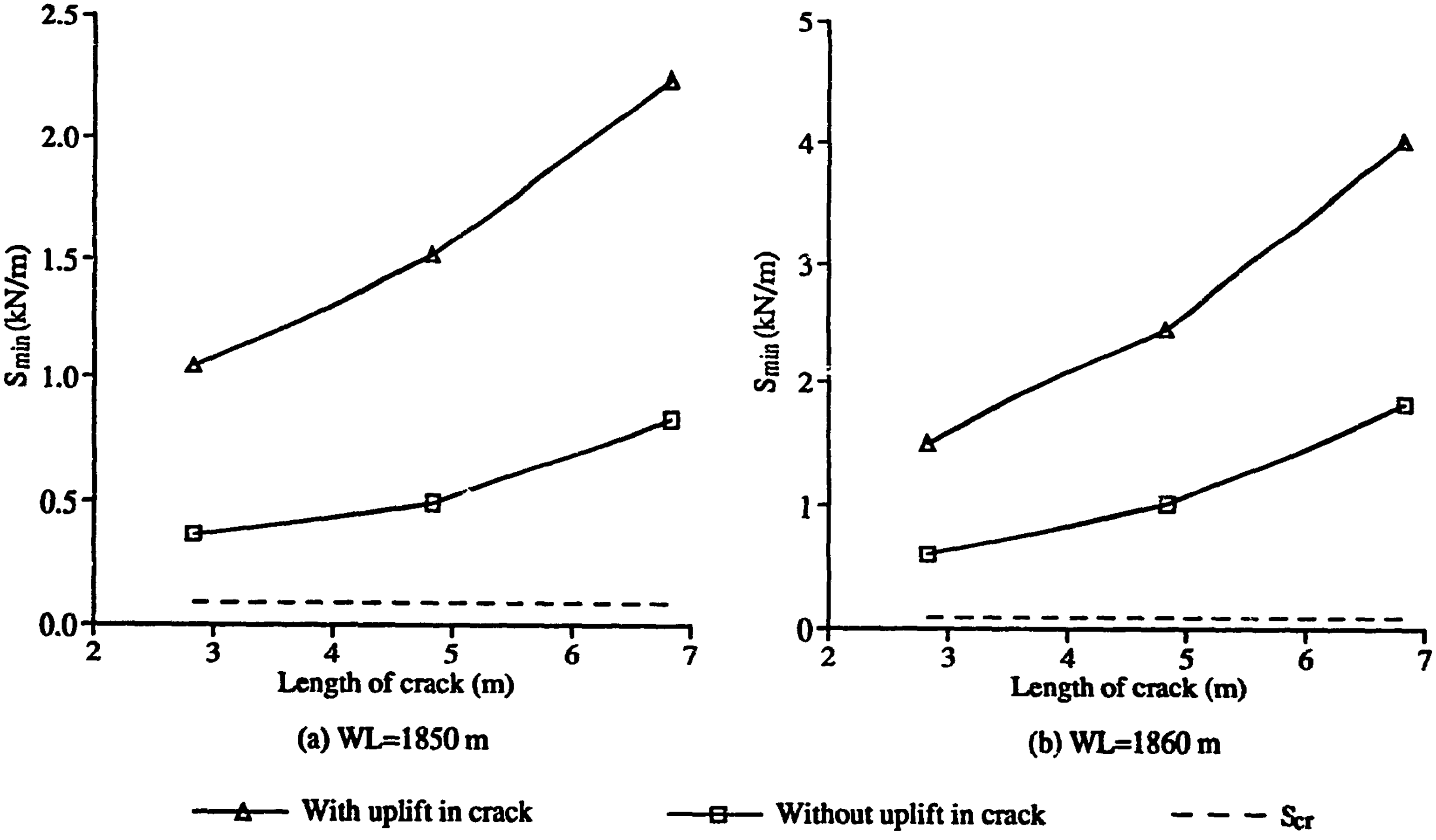

(a) WL=1850 m

(b) WL=1860 m

Figure 6.13 Minimum strain energy density factors of crack model 2 under the loadings of reservoir water, self-weight and temperature

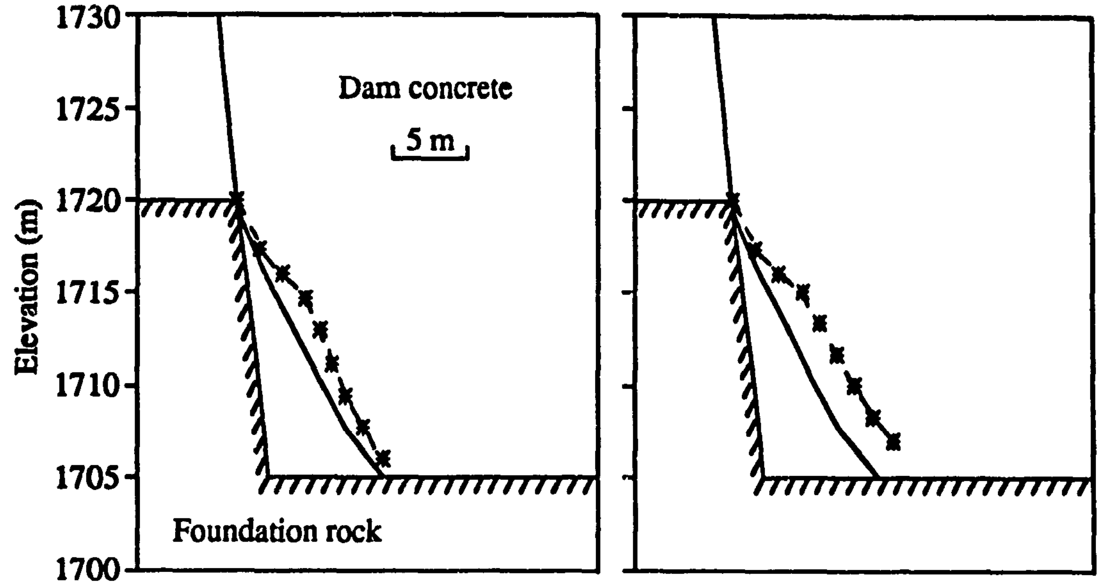

WL=1850 m WL=1860 m

(a) Under the loadings of reservoir water, self-weight and temperature

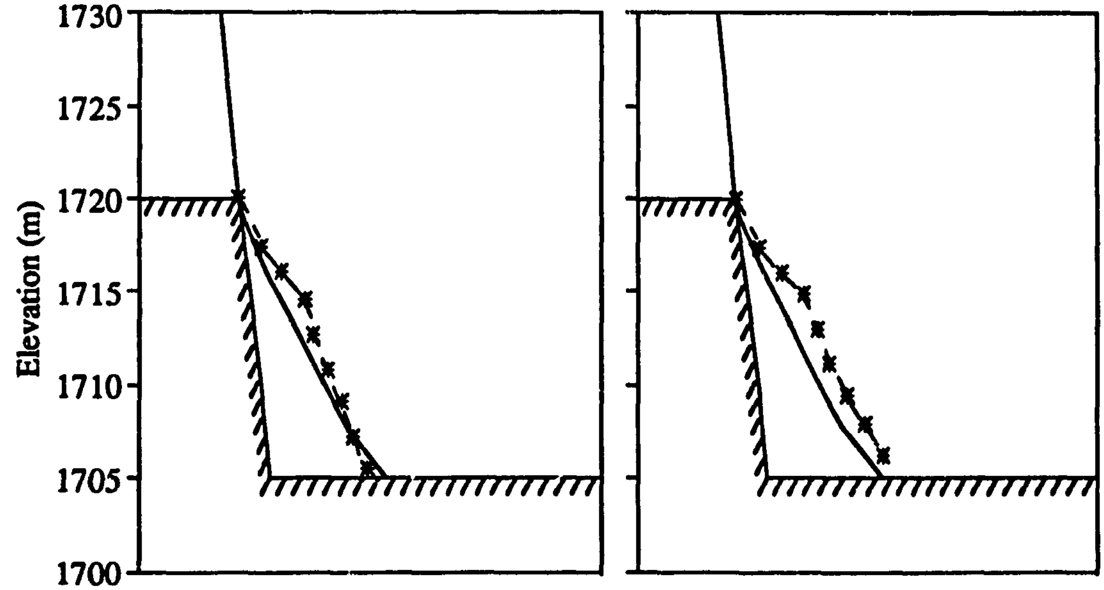

WL=1850 m WL=1860 m

(b) Under the loadings of reservoir water and self-weight

——— Observed — * — Computed

Figure 6.14 Crack profiles of model 3 for different water levels

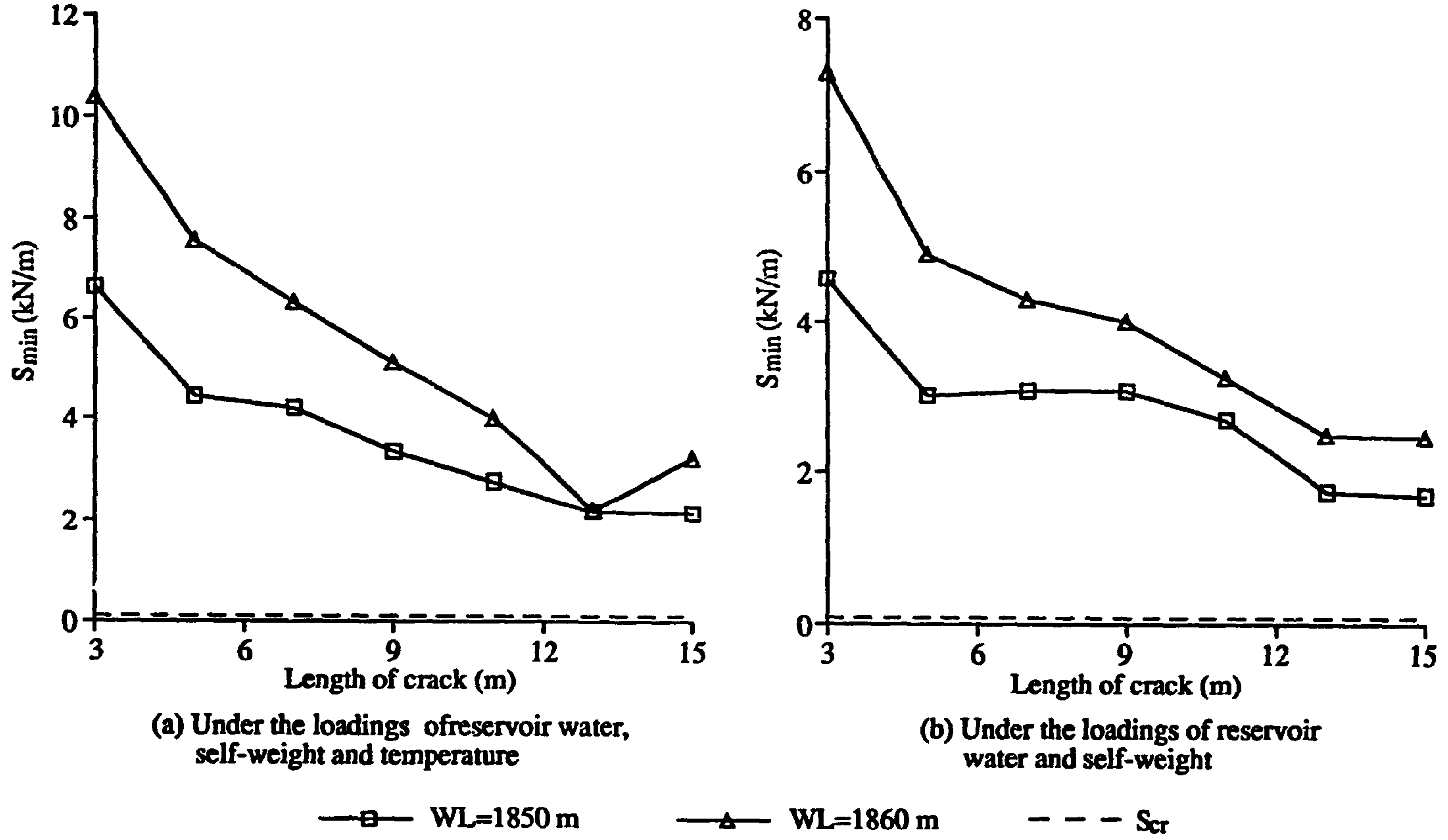

(a) Under the loadings ofreservoir water, self-weight and temperature

(b) Under the loadings of reservoir water and self-weight

Figure 6.15 Minimum strain energy density factors of crack model 3 for different water levels

CHAPTER 7

CONCLUSIONS AND FUTURE STUDY

7.1 CONCLUSIONS

A new procedure for analysis of static and dynamic cracking problems in concrete dams has been presented in this thesis. The LEFM theory, the discrete crack modelling and the BEM are combined in this procedure. Comprehensive analyses including 2-D static and dynamic and 3-D static problems have been conducted using the proposed approach. The innovative points of the approach and the corresponding findings from the analysis are summarized as follows:

1. In a parametric study in computing the 2-D SIFs by BEM, it was found that the best accuracy can be achieved by choosing the length of the crack tip element to be about 10% of the crack length. Comparing BEM and FEM in evaluating stress intensity factors, it was shown that BEM is an efficient method with better accuracy, less computer time and data preparation. As an application example, the stability and propagation process of the cracks around the heel of a typical gravity dam were analyzed. It was found that the horizontal cracks near the heel of the dam will propagate rapidly downwards to the interface between the dam and the foundation once they become unstable. The distribution pattern of uplift pressure on the crack surfaces has a significant effect on the stability of the cracks.

2. A detailed formulation of the 2-D approach for fracture analysis of gravity dams under earthquake loading was presented. Two methods, namely the impact and the force methods, were proposed to simulate the impact process of crack closing during earthquakes. Crack trajectories are obtained by multi-step crack extensions and the BE mode superposition technique is employed in each step of constant crack length. Thus, the

complicated nonlinear problem of crack propagation under dynamic loading is solved by a stepwise linear approach. The accuracy of the procedure was verified by comparison of the computed results with the data of rupture experiments of a cantilever beam and a model of Koyna dam tested on a shaking table, thus confirming the suitability of the 2-D procedure in cracking analysis of concrete gravity dams under dynamic loading.

3. Applying the 2-D dynamic fracture procedure to the case study of the Koyna prototype dam, the behaviour of this dam under the 1967 earthquake was analyzed by both impulse and force methods for simulation of the crack closure mechanism. The comparison between the two models for this mechanism shows expected discrepancies in the time histories of crest displacements and stress intensity factors, but only a slight difference in the instant in time at which rupture is predicted. Furthermore, since crack propagation occurs only during the crack opening phase, the results show that the final rupture profiles obtained from the two methods are in excellent agreement for both the model and prototype dams, thus indicating that the crack closure mechanism has no significant effect on the crack propagation trajectories. The numerical predictions concerning the penetration of the initial crack on the downstream face of Koyna dam through to the upstream face and the elevation at which the crack reaches the upstream surface are consistent with the field measurements after the 1967 earthquake.

4. Extending the 2-D procedure to solving 3-D static cracking problems, a simplified model for crack propagation in arch dams is proposed. The strain energy density factor theory, or so-called S-theory, has been employed to study the crack growth pattern inside the dam body. A through-crack, characterized by a straight line as the crack front, is assumed and the failure orientation at the center point of the front is taken as the common direction of propagation. Numerical examinations have been performed to verify the accuracy of the procedure and its adequacy for arch dams.

5. Employing the 3-D static fracture procedure, propagation of the first upstream cracking incurred in the Kolnbrein arch dam has been analyzed in detail based on three

crack models and different load combinations. The results show that both crack models 1 and 3 predict the observed first upstream cracking, fitting the field data with regard to the relevant reservoir level, temperature and pattern of cracking. Whether small initial cracks were due to stress concentration at the corner point of the dam - foundation interface as in model 3, or due to other factors having caused them to occur on the dam base as in model 1, is not known at present because of the limited information on field measurements. Thus the upward or downward propagation of this otherwise nearly identical cracking pattern is beyond the scope of the present study.

From the above results, it is concluded that the proposed BE procedure based on LEFM can be employed to predict the crack extensions in gravity dams under static and earthquake loadings, and in arch dams under static loading.

7.2 RECOMMENDATIONS FOR FUTURE STUDY

Since fracture in concrete dams is a relatively new field of research, a great deal of study needs to be conducted before the fracture mechanics theory can be applied to the practical design of new concrete dams and the safety evaluation of existing dams.

First, comparison study between the LEFM approach and the NLFM approach is necessary to clarify which theory is more relevant for predicting the cracking behaviour in concrete dams. To achieve this, more experiments on the concrete fracture mechanism and field measurements on existing concrete dams are needed to verify the analytical predictions. Concerning the material parameters such as fracture toughness of mass concrete especially under dynamic loading, little work is available on this topic. More experiments relating to different loading rates are necessary.

Secondly, the post-cracking behaviour of gravity dams after break-through of the crack needs to be studied in order to examine the safety of the dams. In the post-cracking analysis, the frictional forces on the crack surfaces must be incorporated into the present 2-D seismic procedure to provide the critical sliding resistance after the crack penetrates through the dam.

Thirdly, the fracture mechanics theory is not well established for 3-D cracking problems. The most serious limitation of the simplified procedure presented in Chapter 5 is the simulation of 3-D crack propagation by a piece-wise plane through-crack. Investigations by experiments are needed to determine the geometrical shapes of cracks inside 3-D structures and to verify the orientation of crack extension as predicted by theory. In particular, for the S-theory employed here, the algorithm to obtain S_{min} for an arbitrary crack geometry needs to be studied, since it is only available for plane elliptical cracks at present.

Finally, to the author's knowledge, few, if any, fracture analyses of arch dams under seismic loading have appeared in the literature. Experiments on fracture toughness of concrete under multi-axial stresses for both static and dynamic conditions have to be performed in order to obtain more realistic values of the material properties governing fracture of the dam concrete. In addition, the analytical challenge posed by 3-D arch dams under dynamic loading will be much greater than the 2-D case of gravity dams. Thus, there is a great deal of future work to be done concerning 3-D dynamic fracture related to arch dams.

REFERENCES

[1] W. J. Brunner and K. H. Wu, 'Cracking of the Revelstoke concrete gravity dam mass concrete', *15th ICOLD* **2**, Q.57, R.1, Lausanne, Switzerland, 1-21 (1985)

[2] S. Ionescu et al, 'Concrete cracking during Dragan arch dam construction', *15th ICOLD* **2**, Q.57, R.14, Lausanne, Switzerland, 249-261 (1985)

[3] H. L. Boggs, 'Cracking in concrete dams USBR case histories', *15th ICOLD* **2**, Q.57, R.10, Lausanne, Switzerland, 173-190 (1985)

[4] R. Del Hoyo and M. Guerreiro, 'Concrete cracking in two dams', *15th ICOLD* **2**, Q.57, R.18, Lausanne, Switzerland, 319-335 (1985)

[5] C. Tu, 'A study of the cracking of Zhaxi diamond head buttress dam and its strengthening measures', *15th ICOLD* **2**, Q.57, R.38, Lausanne, Switzerland, 653-670 (1985)

[6] C. Tu et al, 'Study of cracking problem in concrete blocks of Dong Jiang arch dam', *J. res. prac. hyd. eng.* (in Chinese), No.1, 1-8 (1991)

[7] Y. Chen and S. Jin, 'Comprehensive analysis of dynamic experiments for Jinshui Tan arch dam in cases of with and without cracks in the dam', *Report of East Design Institute of China for Water Resources and Hydropower Station* (in Chinese), March, 1989

[8] J. A. Veltrop, C. H. Yeh and W. J. Paul, 'Evaluation of cracks in a multiple arch dam', *Dam eng.* **1**, No.1, 5-13 (1990)

[9] R. Dunger, 'Analysis of plastic deformations leading to cracking of grouted contraction joints in Zervreila arch dam', *15th ICOLD* **2**, Q.57, R.20, Lausanne, Switzerland, 343-363 (1985)

[10] A. R. Berchten, 'Repair of the Zeuzier arch dam in Switzerland', *15th ICOLD* **2**, Q.57, R.40, Lausanne, Switzerland, 693-711 (1985)

[11] C. K. Shen, H. C. Chen, C. H. Zhang, et al. 'Earthquakes induced by reservoir

impounding and their effect on Hsingfengkiang dam', *Scientia Sinica* **17**, No.2, (1974)

[12] A. K. Chopra and P. Chakrabarti, 'The Koyna earthquake and the damage to Koyna dam', *Bull. seism. soc. Am.* **63**, 381-397 (1973)

[13] N. Pal, 'Seismic cracking of concrete gravity dams', *J. struct. div. ASCE* **102**, 1827-1844 (1976)

[14] M. L. Ayari and V. E. Saouma, 'A fracture mechanics based seismic analysis of concrete gravity dams using discrete cracks', *Eng. fract. mech.* **35**, No.1/2/3, 587-598 (1990)

[15] S. S. Bhattacharjee and P. Leger, 'Seismic cracking and energy dissipation in concrete gravity dams', *Earthquake eng. struct. dyn.* **22**, 991-1007 (1993)

[16] P. E. Skrikerud and H. Bachmann, 'Discrete crack modelling for dynamically loaded, unreinforced concrete structures', *Earthquake eng. struct. dyn.* **14**, 297-315 (1986)

[17] Research Group of Earthquake Resistance of the Buttress Dam, Dept. of Hydraulic Engineering, Tsinghua University, 'Test studies of earthquake resistance of the massive-head buttress dam', *J. natural science univ., div. civil hyd. eng.* **2**, No.2, 142-160 (1966)

[18] A. Niwa and R. W. Clough, 'Shaking table research on concrete dam models', *Report No. EERC 80-05*, Earthquake Engineering Research Center Report, University of California, Berkeley, CA, 1980

[19] W. P. Donlon and J. F. Hall, 'Shaking table study of concrete gravity dam monoliths', *Earthquake eng. struct. dyn.* **20**, 769-786 (1991)

[20] J. F. Hall, 'The dynamic and earthquake behaviour of concrete dams: review of experimental behaviour and observational evidence', *Soil dyn. earthquake eng.* **7**, No.2, 58-121 (1988)

[21] K. Baustadter and R. Widmann, 'The behaviour of the Kolnbrein arch dam', *15th*

ICOLD 2, Q.57, R.37, Lausanne, Switzerland, 633-651 (1985)

[22] H. N. Linsbauer, A. R. Ingraffea, H. P. Rossmanith and P. A. Wawrzynek, 'Simulation of cracking in large arch dam: Part I', *J. struct. div. ASCE* **115**, No.7, 599-1615 (1989)

[23] H. N. Linsbauer et al, 'Simulation of cracking in large arch dam: Part II', *J. struct. div., ASCE* **115**, No. 7, 1616-1629 (1989)

[24] L. F. Martha, J. LLorca, A. R. Ingraffea and M. Elices, 'Numerical simulation of crack initiation and propagation in an arch dam', *Dam Engrg.* **2**, No. 3, 193-213 (1991)

[25] A. Hillerborg, M. Modeer & P. E. Peterson, 'Analysis of crack formation and crack growth in concrete by means of fracture mechanics and finite element', *Cement concrete res.* **6**, No.6, 773-782 (1976)

[26] Z. P. Bazant & B. H. Oh, 'Crack band theory for fracture of concrete', *Mat. const.* **16**, No.93, 155-177 (1983)

[27] V. E. Saouma, E. Bruhwiler and H. L. Boggs, 'A review of fracture mechanics applied to concrete dams', *Dam eng.* **1**, No.1, 41-57 (1990)

[28] M. Cervera, J. Oliver, E. Herrero and E. Onate, 'A computational model for progressive cracking in large dams due to the swelling of concrete', *Eng. fract. mech.* **35**, No.1/2/3, 573-585 (1990)

[29] B. Fauchet, O. Coussy, A. Carrere and B. Tardieu, 'Poroplastic analysis of concrete dams and their foundations', *Dam eng.* **2**, No.3, 165-192 (1991)

[30] C. A. Brebbia, J. C. F. Tells and L. C. Wrobel, Boundary Element Techniques: Theory and Applications in Engineering, Springer-Verlag, Berlin, Heidelberg, 1984

[31] O. A. Pekau, Zhang Chuhan and Feng Lingmin, 'Seismic fracture analysis of concrete gravity dams', *Earthquake eng. struct. dyn.* **20**, 335-354 (1991)

[32] O. A. Pekau, Feng Lingmin and Zhang Chuhan, 'Seismic fracture of Koyna dam:

case study', *Earthquake eng. struct. dyn.* (accepted in March 1994)

[33] L. M. Feng, O. A. Pekau and C. H. Zhang, 'Cracking Analysis of Arch Dams by 3-D Boundary Element Method', *Journal of Structural Engineering, ASCE* (submitted in June, 1994)

[34] T. A. Cruise, 'Numerical evaluation of elastic stress intensity factors by the boundary integral equation method', in the Surface Crack: Physical Problems and Computation Solutions, ASME, New York,1972

[35] T. A. Cruise, 'Applications of the boundary integral equation method to three dimensional stress analysis', *Computers struct.* **3**, 509-527 (1973)

[36] G. E. Blandford, A. R. Ingraffea and J. A. Liggett, 'Two-dimensional stress intensity factor computations using the boundary element method', *Int. j. numer. methods eng.* **17**, 387-404 (1981)

[37] Melvin F. Kanninen and Carl H. Popelar, Advanced Fracture Mechanics, Oxford University Press, New York, 1985

[38] R. N. L. Smith and J. C. Mason, 'A boundary element method for curved crack problems in two dimensions', *Boundary Element Method in Engineering, 4th International Conference on Boundary Element Methods*, Springer-Verlag, Berlin, 472-484 (1982)

[39] R. E. Smelser, 'Evaluation of stress intensity factors for bimaterial bodies using numerical crack flank displacement data', *Int. j. fract.* **15**, No.2 (1979)

[40] D. Y. Xu *et al.*, 'Experimental studies of fracture criteria for combined crack mechanism of concrete using four point shear samples', *J. hyd. eng.* (Beijing), No. 9, 63-69 (1984)

[41] W. X. Fan, 'Circumferential strain factor criterion for complex brittle fracture', *Appl. math. mech.* (Beijing) **3** , No. 2, 211-224 (1983)

[42] M. Stern, E. Becker, R. Dunham, 'Contour integral computation of mixed-mode stress intensity factors', *Int. j. fract.* **12**, 359-368 (1976)

[43] Y. Y. Cai et al., 'Application of isoparametric element in determination of stress intensity factors', *J. hyd. eng.* (Beijing), No.1 (1981)

[44] M. L. Tian et al., 'Toughness of concrete', *J. hyd. eng.* (Beijing), No.6, 38-46 (1982)

[45] C. H. Zhang and C. M. Song, 'Boundary element technique in infinite and semi-infinite plane domain', *Boundary Elements, Proceedings of International Conference*, Beijing, China, 551-558 (1986)

[46] D. Nardini and C. A. Brebbia, 'A new approach to free vibration analysis using boundary elements', *Boundary Element Method in Engineering, 4th International Conference on Boundary Element Methods*, Springer-Verlag, Berlin, 312-326 (1982)

[47] D. Nardini and C. A. Brebbia, 'Transient boundary element elastodynamics using the dual reciprocity method and modal superposition', *Proc. 8th int. conf. BEM*, Tokyo **1**, 435-443 (1986)

[48] Y. G. Hanna and J. L. Humar, 'Boundary element analysis of fluid domain', *J. eng. mech. div. ASCE* **108**, 436-451 (1982)

[49] C. M. Song and C. H. Zhang,'Dynamic boundary element method for seismic analysis of concrete dams,' *Earthquake eng. eng. vib.* (Beijing) **8**, No.4 (1988)

[50] R. E. Taylor, 'Analysis of hydrodynamic loads by boundary elements', *In: Developments in Boundary Element Method - 2*, P.K. Banerjee and R.P. Show (Eds.), Applied Science Publishers, London, 211-244 (1982)

[51] J. Zhou and H. G. Ni, 'Response of cracked structures during earthquakes', *Earthquake eng. eng. vib.* (Beijing) **6**, No.2, 52-58 (1986)

[52] R. Z. Zhou and G. T. Liu, 'The estimation of accuracy of Williams premier expansion as compared with exact solutions', *J. Fuzhou univ.*, No.2, 89-100 (1986)

[53] Koyna Earthquake of December 11, 1967, *Report of the UNESCO Committee of*

Experts, New Delhi, 1968

[54] S. Mindess, 'Fracture toughness testing of cement and concrete', *in Fracture Mechanics of Concrete: Material Characterization and Testing*, A. Carpinteri and A.R. Ingraffea (Eds.), Martinus Nijhoff Publishers, The Hague, 67-110 (1984)

[55] J. C. Lachat and J. O. Watson, 'Effective numerical treatment of boundary integral equations: a formulation for three-dimensional elastostatics', *Int. j. numer. methods eng.* **10**, 991-1005 (1976)

[56] D. J. Danson, 'A boundary element formulation of problems in linear isotropic elasticity with body forces', in *Boundary Element Methods*, C.A. Brebbia (Ed.), Springer-Verlag, Berlin, 105-122 (1981)

[57] I. S. Raju and J. C. Newman, Jr, 'Stress intensity factors for a wide range of semi-elliptical surface cracks in finite-thickness plates', *Eng. fract. mech.* **11**, 817-829 (1979)

[58] M. L. Luchi and A. Poggialini, 'Computation of 3-dimensional stress intensity factors using special boundary elements', *Boundary Elements, Proceedings of the 5th International Conference*, 461-470 (1983)

[59] M. Tanaka and H. Itoh, 'Boundary element modelling of crack singularities in 3-D elastostatics', *Boundary Elements, Proceedings of International Conference*, Beijing, 275-285 (1986)

[60] Y. Zhang and W. Feng, 'Investigation in weighted function and optimization of isoparametric singular boundary elements' size in 3-D crack problem', *Eng. fract. mech.* **26**, No.4, 611-617 (1987)

[61] G. Luo and Y. Zhang, 'Application of boundary element method with singular and isoparametric elements in three dimensional crack problems', *Eng. fract. mech.* **29**, No.1, 97-106 (1988)

[62] G. Luo and Y. Zhang, 'Improvement of stress singular element for crack problems in three dimensional boundary element method', *Eng. fract. mech.* **31**, No.6, 993-

999 (1988)

[63] G. R. Irwin, 'Fracture', *Handbook der Physik* 79, Springer-Verlag, Berlin, 551-590 (1958)

[64] M. L. Williams, 'On the stress distribution at the base of a stationary crack', *J. appl. mech.* 24, 109-114 (1957)

[65] G. C. Sih, 'Introduction Chapter: A three-dimensional strain energy density factor theory of crack propagation', Mechanics of Fracture, Vol. 2: Three-dimensional Crack Problems, G.C. Sih (Ed.), 1974

[66] Zhang Chuhan, Song Chongmin, Wang Gwanglun and Jin Feng, '3-D infinite boundary elements and simulation of monolithic dam foundations', *Commun. appl. numer. methods* 5, No.6, 389-400 (1989)

[67] G. P. Cherepanov, Mechanics of Brittle Fracture, McGraw-Hill International Book Company, 1979

[68] M. K. Kassir and G. C. Sih,'Three-dimensional stress distribution around an elliptical crack under arbitrary loadings', *J. appl. mech. ASME ser.E* 33, No.3, 601-611 (1966)

[69] H. Ludescher, 'A modern instrumentation for the surveillance of the stability of the Kolnbrein dam', *15th ICOLD* 1, Q.56, R.42, Lausanne, Switzerland, 797-811 (1985)

[70] K. Kovari, 'Detection and monitoring of structural deficiencies in the rock foundations of large dams', *15th ICOLD* 1, Q.56, R.36, Lausanne, Switzerland, 695-719 (1985)

[71] W. Demmer and H. Ludescher, 'Measures taken to reduce uplift and seepage at Kolnbrein dam', *15th ICOLD* 3, Q.58, R.81, Lausanne, Switzerland, 1373-1393 (1985)

[72] P. Obernhuber, 'Remedial works for the Kolnbrein dam: design and analysis', *17th ICOLD* 4, C.7, Vienna, Austria, 697-714 (1991)

[73] 'Remedial projects for Kolnbrein arch dam design and construction', *Reports of Oslerreichische Draukraftwerke AG. Carinthia*, Austria, June 1991

[74] B. Zhu, 'On temperature load of arch dams', *J. hydropower* (Beijing), No. 2, 23-29 (1984)

APPENDIX I

GEOMETRY OF KOLNBREIN ARCH DAM

The Tauernplan Consulting GMBH in Austria is gratefully acknowledged for providing the following geometry data of the Kolnbrein arch dam.

NOTATION FOR THE GEOMETRY OF THE DAM

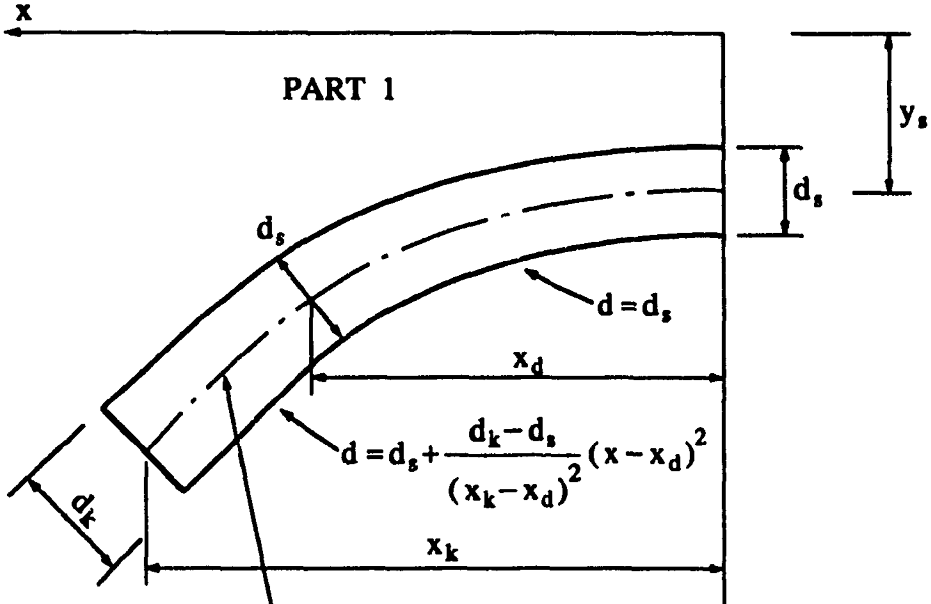

Equation of the axis:

$$x^2+(1-\varepsilon^2)(y-y_s)^2-2\rho_s(y-y_s)=0$$

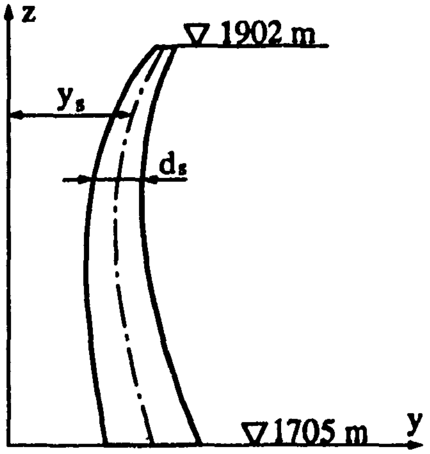

GEOMETRY DATA OF PART 1 (WEST) OF KOLNBREIN DAM

z (m)	y_s (m)	ρ_s (m)	ε^2	x_d (m)	x_k (m)	d_s (m)	d_k (m)
197.0	30.976	250.944	1.74635	260.80	260.80	7.600	7.600
195.0	30.000	250.000	1.69975	257.94	258.95	7.999	8.061
190.0	27.713	247.617	1.58365	250.80	254.30	8.993	9.210
185.0	25.633	245.200	1.46888	243.66	249.58	9.976	10.348
180.0	23.745	242.749	1.35637	236.51	244.73	10.940	11.468
175.0	22.036	240.262	1.24708	229.35	239.70	11.878	12.563
170.0	20.496	237.738	1.14180	222.19	234.48	12.782	13.629
165.0	19.115	235.175	1.04105	215.02	229.16	13.655	14.674
160.0	17.883	232.572	0.94529	207.85	223.83	14.498	15.710
155.0	16.791	229.927	0.85497	200.69	218.60	15.310	16.744
150.0	15.832	227.239	0.77042	193.54	213.54	16.094	17.786
145.0	14.999	224.506	0.69134	186.40	208.64	16.850	18.838
140.0	14.286	221.727	0.61730	179.27	203.87	17.579	19.903
135.0	13.685	218.901	0.54787	172.13	199.21	18.282	20.984
130.0	13.192	216.025	0.48260	164.99	194.63	18.960	22.081
125.0	12.802	213.098	0.42108	157.84	190.10	19.613	23.197
120.0	12.509	210.118	0.36291	150.68	185.62	20.243	24.322
115.0	12.309	207.085	0.30769	143.50	181.19	20.853	25.448
110.0	12.199	203.997	0.25506	136.31	176.81	21.446	26.565
105.0	12.173	200.851	0.20461	129.09	172.47	22.023	27.665
100.0	12.229	197.648	0.15610	121.85	168.17	22.587	28.741
95.0	12.363	194.385	0.10977	114.60	163.91	23.142	29.803
90.0	12.572	191.061	0.06600	107.36	159.70	23.689	30.866
85.0	12.853	187.675	0.02517	100.14	155.54	24.233	31.942
80.0	13.203	184.225	-0.01233	92.95	151.43	24.776	33.046
75.0	13.619	180.712	-0.04599	85.81	147.34	25.322	34.180
70.0	14.099	177.133	-0.07477	78.75	143.18	25.873	35.308
65.0	14.641	173.489	-0.09748	71.79	138.82	26.435	36.384
60.0	15.242	169.778	-0.11295	64.97	134.13	27.009	37.360
55.0	15.900	166.000	-0.12000	58.30	129.00	27.600	38.190
50.0	16.613	162.155	-0.11762	51.82	123.38	28.211	38.849
45.0	17.380	158.241	-0.10553	45.59	117.58	28.845	39.402
40.0	18.197	154.260	-0.08363	39.65	111.98	29.505	39.932
35.0	19.065	150.211	-0.05182	34.07	106.98	30.194	40.525
30.0	19.980	146.095	-0.00960	28.87	102.66	30.915	41.202
25.0	20.942	141.911	0.04507	24.04	97.87	31.671	41.714
20.0	21.949	137.660	0.11464	19.53	91.13	32.465	41.751
15.0	23.000	133.342	0.20154	15.31	81.00	33.300	41.000
10.0	24.093	128.959	0.30722	11.31	66.73	34.176	39.545
5.0	25.227	124.512	0.42905	7.47	45.00	35.081	38.000
0.0	26.400	120.000	0.56176	3.70	0.00	36.000	36.000

GEOMETRY DATA OF PART 2 (EAST) OF KOLNBREIN DAM

z (m)	y_s (m)	ρ_s (m)	ε^2	x_d (m)	x_k (m)	d_s (m)	d_k (m)
197.0	30.976	250.944	1.08300	253.22	266.40	7.600	7.600
195.0	30.000	250.000	1.05119	250.01	264.48	7.999	8.161
190.0	27.713	247.617	0.97214	241.98	259.65	8.993	9.558
185.0	25.633	245.200	0.89474	233.95	254.75	9.976	10.938
180.0	23.745	242.749	0.82016	225.92	249.73	10.940	12.288
175.0	22.036	240.262	0.74958	217.90	244.55	11.878	13.596
170.0	20.496	237.738	0.68373	209.89	239.19	12.782	14.859
165.0	19.115	235.175	0.62244	201.89	233.73	13.655	16.093
160.0	17.883	232.572	0.56539	193.92	228.26	14.498	17.317
155.0	16.791	229.927	0.51225	185.97	222.87	15.310	18.551
150.0	15.832	227.239	0.46270	178.06	217.63	16.094	19.809
145.0	14.999	224.506	0.41635	170.19	212.53	16.850	21.094
140.0	14.286	221.727	0.37281	162.34	207.55	17.579	22.402
135.0	13.685	218.901	0.33167	154.51	202.66	18.282	23.733
130.0	13.192	216.025	0.29254	146.70	197.82	18.960	25.084
125.0	12.802	213.098	0.25510	138.90	193.02	19.613	26.449
120.0	12.509	210.118	0.21936	131.15	188.24	20.243	27.814
115.0	12.309	207.085	0.18540	123.47	183.47	20.853	29.159
110.0	12.199	203.997	0.15330	115.90	178.72	21.446	30.467
105.0	12.173	200.851	0.12314	108.48	173.96	22.023	31.717
100.0	12.229	197.648	0.09500	101.24	169.19	22.587	32.896
95.0	12.363	194.385	0.06879	94.22	164.40	23.142	34.005
90.0	12.572	191.061	0.04442	87.47	159.55	23.689	35.049
85.0	12.853	187.675	0.02180	81.02	154.64	24.233	36.033
80.0	13.203	184.225	0.00083	74.91	149.64	24.776	36.963
75.0	13.619	180.712	-0.01856	69.19	144.55	25.322	37.843
70.0	14.099	177.133	-0.03636	63.79	139.35	25.873	38.667
65.0	14.641	173.489	-0.05255	58.65	134.07	26.435	39.430
60.0	15.242	169.778	-0.06711	53.73	128.72	27.009	40.126
55.0	15.900	166.000	-0.08000	48.94	123.30	27.600	40.750
50.0	16.613	162.155	-0.09121	44.26	117.84	28.211	41.297
45.0	17.380	158.241	-0.10077	39.67	112.40	28.845	41.773
40.0	18.197	154.260	-0.10872	35.21	107.05	29.505	42.185
35.0	19.065	150.211	-0.11511	30.90	101.89	30.194	42.541
30.0	19.980	146.095	-0.11993	26.74	96.77	30.915	42.808
25.0	20.942	141.911	-0.12305	22.73	90.82	31.671	42.794
20.0	21.949	137.660	-0.12429	18.82	82.93	32.465	42.269
15.0	23.000	133.342	-0.12349	15.00	72.00	33.300	41.000
10.0	24.093	128.959	-0.12056	11.22	57.50	34.176	39.078
5.0	25.227	124.512	-0.11587	7.47	37.00	35.081	37.200
0.0	26.400	120.000	-0.11000	3.72	0.00	36.000	36.000

APPENDIX II

TEMPERATURE LOAD IN ARCH DAM

The procedure to compute the temperature load in arch dams during the operation stage proposed by Zhu[74] is briefly described below.

According to the assumption in mechanics of materials that the transverse sections of a beam remain plane after bending, the temperature distribution T(x) along the thickness direction x of an arch section at any time can be decomposed into three parts T_m, T_d and T_n as shown in Figure 1.

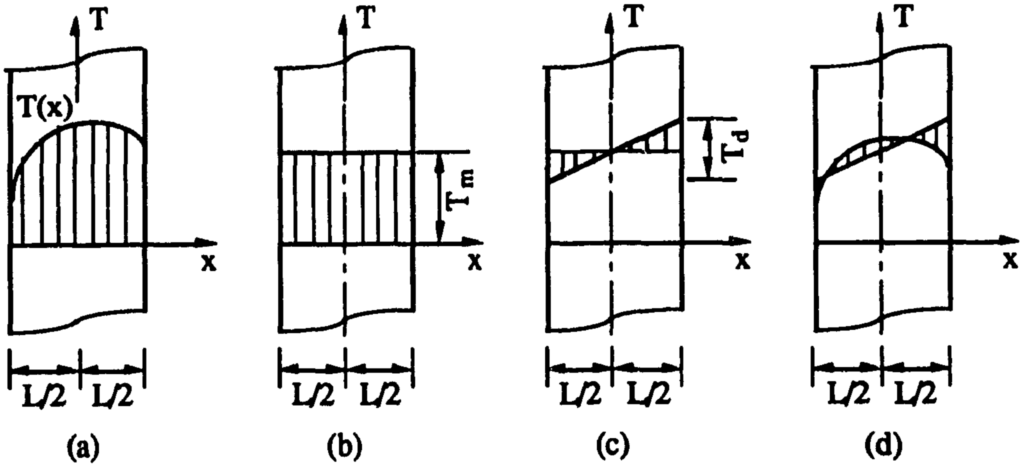

Figure 1 Decomposition of temperature distribution along thickness direction of an arch section: (a) Real temperature; (b) Mean temperature T_m; (c) Equivalent linear temperature difference T_d; (d) Nonlinear temperature difference T_n

The mean temperature along thickness T_m, the equivalent linear temperature difference between the downstream and upstream faces T_d and the nonlinear temperature difference T_n are defined by the following equations:

$$T_m = \frac{1}{L}\int_{-\frac{L}{2}}^{\frac{L}{2}} T(x)\,dx \qquad (1)$$

$$T_d = \frac{12}{L^2}\int_{-\frac{L}{2}}^{\frac{L}{2}} T(x)\,x\,dx \tag{2}$$

$$T_n = T(x) - T_d\, x/L \tag{3}$$

where L denotes the thickness of the arch section.

The nonlinear temperature difference T_n is usually neglected since it does not create axial force and bending moment in arch dam. Thus, only T_m and T_d need to be evaluated.

The temperature field in arch dams varies with time. The following three temperature fields are important in determining temperature load.

(i) Temperature field at the time when the construction joints are grouted $T_0(x)$ -- the corresponding mean temperature along the thickness and the equivalent linear temperature difference are denoted as T_{m0} and T_{d0}, respectively.

(ii) Yearly mean temperature field $T_1(x)$ in operation stage -- the corresponding mean temperature along the thickness and the equivalent linear temperature difference are represented by T_{m1} and T_{d1}, respectively.

(iii) Varying temperature field $T_2(x,t)$ at time t during operation stage -- the corresponding mean temperature along the thickness and the equivalent linear temperature difference are denoted as T_{m2} and T_{d2}, respectively.

Thus, the temperature change in an arch dam at any time with respect to the temperature when the construction joints are grouted are obtained by

$$\begin{aligned} \Delta T_m &= T_{m1} - T_{m0} + T_{m2} \\ \Delta T_d &= T_{d1} - T_{d0} \div T_{d2} \end{aligned} \tag{4}$$

where ΔT_m and ΔT_d denote the temperature changes of mean temperature along the thickness and the equivalent linear temperature difference, respectively.

Thus, the temperature load in an arch dam, i.e. the temperature change ΔT_U and ΔT_D

on the upstream and downstream faces, respectively, are obtained by

$$\Delta T_U = \Delta T_m - \frac{1}{2}\Delta T_d \qquad (5)$$
$$\Delta T_D = \Delta T_m + \frac{1}{2}\Delta T_d$$

Determination of T_{m0}, T_{d0}, T_{m1}, T_{d1}, T_{m2} and T_{d2}

(a) T_{m0} and T_{d0}

In practice, the construction joints are grouted at the yearly mean temperature before the filling of reservoir. Thus, we have

$$T_{m0} = T_{m1} \qquad (6)$$
$$T_{d0} = 0$$

(b) T_{m1} and T_{d1}

Since $T_1(x)$ is distributed linearly along the thickness direction, T_{m1} and T_{d1} are obtained by

$$T_{m1} = (T_{UM} + T_{DM})/2 \qquad (8)$$
$$T_{d1} = T_{DM} - T_{UM}$$

where T_{DM} denotes the yearly mean temperature on the downstream face of the dam, equaling the yearly mean air temperature plus the effect of sunlight radiation; T_{UM} represents the yearly mean temperature on the upstream face, i.e. the yearly mean water temperature in the reservoir which can be determined by the following empirical formulae:

$$T_{UM} = c + (T_s - c)e^{-0.04y} \qquad (9)$$

where

$$c = (T_b - T_s\, g)/(1-g)$$

$$g = e^{-0.04H}$$

H denotes the depth of the reservoir; T_s and T_b are the yearly mean water temperatures at the surface and the bottom of reservoir, respectively; y represents the water depth at the considered elevation.

(c) T_{m2} and T_{d2}

(i) Above water level

$$T_{m2} = \pm \rho_1 A_D \quad , \quad T_{d2} = 0 \tag{10}$$

(ii) Below water level

$$T_{m2} = \pm \frac{\rho_1}{2}\left(A_D + \frac{13.1\, A_{w0}}{14.5+y}\right) \tag{11}$$

$$T_{d2} = \pm \rho_3 \left[A_D - A_{w0}\left(\xi + \frac{13.1}{14.5+y}\right)\right] \tag{12}$$

where

A_D -- amplitude of temperature variation in a year on downstream face, equaling to the amplitude of air temperature variation in a year plus the effect of sunlight radiation.

A_{w0} -- amplitude of surface water temperature variation in a year. In tropical and temperate zones, $A_{w0} = (T_7 - T_1)/2$; In frigid zone, $A_{w0} = T_7/2 + 1.5$; in which T_1 and T_7 are monthly mean air temperature in January and July, respectively.

y -- depth of water at considered elevation.

The coefficients ρ_1, ρ_3 and ξ are determined by the following equations:

(i) When $L \geq 10$ m,

$$\rho_1 = 4.66/(L - 0.90)$$

$$\rho_3 = 18.76 / (L + 12.6) \qquad (13)$$

$$\xi = (3.80\, e^{-0.022\, y} - 2.38\, e^{-0.081\, y}) / (L - 4.50)$$

(ii) When $L \leq 10$ m,

$$\rho_1 = e^{-0.00067\, L^3}$$

$$\rho_3 = e^{-0.00186\, L^2} \qquad (14)$$

$$\xi = (0.069\, e^{-0.022\, y} - 0.0432\, e^{-0.081\, y})\, L$$

where L represents the dam thickness (m).